

REPORT DOCUMENTATION PAGE			Form Approved OMB NO. 0704-0188	
Public Reporting burden for this collection of information is estimated to average 1 hour per response, including the time for reviewing instructions, searching existing data sources, gathering and maintaining the data needed, and completing and reviewing the collection of information. Send comment regarding this burden estimates or any other aspect of this collection of information, including suggestions for reducing this burden, to Washington Headquarters Services, Directorate for information Operations and Reports, 1215 Jefferson Davis Highway, Suite 1204, Arlington, VA 22202-4302, and to the Office of Management and Budget, Paperwork Reduction Project (0704-0188,) Washington, DC 20503.				
1. AGENCY USE ONLY (Leave Blank)		2. REPORT DATE August 31, 2005		3. REPORT TYPE AND DATES COVERED Interim Progress Report, August 1, 2004 to July 31, 2005
4. TITLE AND SUBTITLE Fundamental Understanding of Propellant/Nozzle Interaction for Rocket Nozzle Erosion Minimization under very High Pressure Conditions.			5. FUNDING NUMBERS N00014-04-1-0683	
6. AUTHOR(S) Kenneth K. Kuo, Kenneth Brezinsky, Sathyanaraya Hanagud, Stephan Irle, Joseph H. Koo, M.C. Lin, Suresh Menon, John Morral, Jamal Musaev, Jerry Seitzman, Angus Wilkinson, Vigor Yang, and Richard A. Yetter				
7. PERFORMING ORGANIZATION NAME(S) AND ADDRESS(ES) The Pennsylvania State University, University Park, PA The University of Illinois, Chicago, Chicago, IL The Georgia Institute of Technology, Atlanta, GA The Ohio State University, Columbus, OH Emory University, Atlanta, GA The University of Texas, Austin, TX			8. PERFORMING ORGANIZATION REPORT NUMBER	
9. SPONSORING / MONITORING AGENCY NAME(S) AND ADDRESS(ES) U. S. Office of Naval Research Ballston Centre Tower One 800 North Quincy Street Arlington, VA 22217-5660			10. SPONSORING / MONITORING AGENCY REPORT NUMBER	
11. SUPPLEMENTARY NOTES The views, opinions and/or findings contained in this report are those of the author(s) and should not be construed as an official Department of the Army position, policy or decision, unless so designated by other documentation.				
12 a. DISTRIBUTION / AVAILABILITY STATEMENT  Approved for public release; distribution unlimited.			12 b. DISTRIBUTION CODE	
13. ABSTRACT (Maximum 200 words)  To substantially increase the operating pressures of future missiles, this MURI project addresses scientific understanding and methods for mitigation of rocket nozzle erosion by solid-propellant combustion products. Several processes can affect the nozzle erosion rate at high pressure and temperature conditions. Three approaches have been used to reduce the thermochemical/mechanical erosion rates of nozzle materials, including improving the thermochemical resistance of the nozzle materials, modifying the solid propellant formulation, and/or introducing boundary-layer control methods. The experimental efforts of the program are guided by state-of-the-art theoretical calculations. During the past year, great progress has been made on the development of both numerical codes and new experimental test facilities. Test rigs have been designed for simulating ultra high-pressure rocket nozzle conditions; with X-ray radiography for erosion rate measurements. A vortex combustor was also designed to simulate propellant product species and to evaluate their effects on nozzle erosion process. A nozzle erosion code has been updated to include comprehensive heterogeneous surface reaction mechanism at high-pressure conditions. The reaction kinetics of nozzle materials has been studied and calculations have been performed using quantum-mechanical and molecular dynamics models. A micro-scale dynamics sub-grid model has been adopted in a parallel LES code to determine the effect of surface shear forces on physical erosion of nozzle throat. Phase diagrams of the W-O-C-H-Cl systems have been obtained to acquire insight into tungsten reaction mechanisms with gaseous mixtures at high-pressure conditions. From equilibrium calculations, tungsten-based nozzles are suitable for aluminized propellants since tungsten oxide and tungsten oxychloride formation are significantly reduced due to the strong affinity of oxygen for aluminum.				
14. SUBJECT TERMS High-temperature nozzle materials, graphite, tungsten, rocket motor simulator, vortex combustor, X-ray radiography, mechanical erosion, heterogeneous reaction, reaction kinetics, phase diagram, LES, recession rate, ultra-high pressure, solid propellant rocket.			15. NUMBER OF PAGES 108	
			16. PRICE CODE	
17. SECURITY CLASSIFICATION OR REPORT UNCLASSIFIED	18. SECURITY CLASSIFICATION ON THIS PAGE UNCLASSIFIED	19. SECURITY CLASSIFICATION OF ABSTRACT UNCLASSIFIED	20. LIMITATION OF ABSTRACT  UL	

# REPORT DOCUMENTATION PAGE (SF298) (Continuation Sheet)

## Table of Contents

Introduction	4
Organization	5
Objectives and Approach	6
Scientific Progress and Accomplishments	8
1. Design of a Rocket Motor Simulator (Kuo Group at PSU)	8
1.1 Simulation of Propellant Product Species to Match Those of Propellant S	8
1.2 Justification for Removing Chlorine from the Rocket Motor Simulator	9
1.3 Simulation of Product Species of Propellant S in the Rocket Motor Simulator	10
1.4 RMS Design Description	11
1.5 Baseline X-ray Transparent Nozzle	16
1.6 Nozzle Assembly with Boundary-Layer Control Mechanism	17
1.7 Flow Field Calculations Using Fluent Code	18
2. Design of a High-Pressure Rocket Motor (Kuo Group at PSU)	18
2.1 Pressure Independence of Product Species	18
2.2 Rocket Motor Design Using Volume Filling Code	20
2.3 Propellant Grain Requirements: Penn State University	21
2.4 Test Site Design	21
3. Recent Progress in Theoretical Model and Numerical Code for Nozzle Erosion (Kuo Group at PSU)	22
3.1 Literature Review	22
3.2 GRC Code Modifications and Simulation	24
4. Heterogeneous Surface Oxidation, Carburization, and Nitration Studies of Bulk Tungsten, Rhenium, and Hafnium (Yetter Group at PSU)	26
5. Modeling and Simulation of Nozzle Material Erosion (Yang Group at PSU)	32
5.1 Heterogeneous chemical kinetics at the gas-solid interface	33
5.2 Chemical kinetics model for graphite oxidation	34
5.3 Chemical kinetics in the gas phase	35
5.4 Turbulence closure using LES (Large-eddy simulations)	36
5.5 Numerical treatment	37
6. Measurement of Gas-Phase and Heterogeneous Reaction Rates of Carbon and Tungsten Systems at High-Pressure and High-Temperature Conditions (Brezinsky Group at UIC)	37
6.1 Shock Tube	37
6.2 Particle Injector	37
6.3 Injector Problems	38
6.4 Shock Tube Heating	39
6.5 Kinetics Study	40
7. Computational Approach towards Prediction of Kinetic Rate Constants (Lin, Musaev, and Irle Group at Emory)	41

7.1 DFT, ONIOM, and DFTB-D Studies of Water Clusters on Graphite	42
7.2 Dissociative Adsorption of H <sub>2</sub> O on Graphite	44
7.3 Dissociative Adsorption of CO <sub>2</sub> on Graphite	47
7.4 Reactions of W/W <sup>+</sup> with H <sub>2</sub> O	49
7.5 Reactions of CO and OH with Pristine Graphite Surfaces	51
8. Literature Survey and Database Compilation on Nozzle Materials (Koo Group at UTA)	51
8.1 Literature Survey	51
8.2 Survey of rocket propulsion companies	52
8.3 Baseline nozzle material	52
9. Mechanisms of time dependent nozzle erosion processes (Hanagud, Wilkinson, and Seitzman Group at GaTech)	55
9.1 Erosion tests	55
9.2 Nozzle Fabrication	56
9.3 First principles studies of time dependant nozzle erosion	58
10. Simulation of Erosion in a Solid Rocket Nozzle (Menon Group at GaTech)	66
10.1 Method of Study	67
10.2 Modeling of Surface Kinetics	69
10.3 Micro Scale Dynamic (MSD) Model	69
10.4 Results and Discussion	72
11. Phase diagrams and diffusion mechanisms in consideration of the oxidation, carburization and nitration of bulk metals (Morral Group at OSU)	80
11.1 W-O-C-H Phase and Stability Diagrams	80
11.2 W-CL-H-O stability diagrams	82
11.3 Kinetic Database	85
Major Accomplishments and Findings	88
List of Papers Submitted or Published under ONR Sponsorship	92
Demographic Data	92
Acknowledgments	93
References	93
Appendices	102

## Introduction

To minimize the erosion rate of nozzle of solid propellant rockets, there are generally three different techniques: 1) to improve the thermochemical resistance of the nozzle materials, 2) to modify the solid propellant formulation, and 3) to introduce boundary-layer controlled methods. Any combination of the above techniques can also be applied. In view of the recent success in the development of high-pressure vessels, the performance of future solid rockets could be advanced if the operating pressure is increased from the conventional range. This is due to the fact that for a given missile volume, more propulsive energy can be gained from combustion systems with higher pressures. However, this advancement depends strongly upon the control of nozzle throat erosion rate. To facilitate the development of high-pressure rockets, it is vitally important to advance the fundamental understanding of the nozzle erosion processes and to develop useful scientific tools in this specific subject area.

During this reporting period, numerous exchanges of technical information were made between Dan Miller of NAWC-China Lake and our MURI team. These interactions have resulted in the determination of two baseline propellant formulations, which have the capability to burn at ultra high-pressure conditions. These propellants are called: Propellant S for non-metallized reduced smoke propellant and Propellant M for metallized propellant with significant amount of aluminum particle loading. More detailed discussions of these two propellants are provided in later sections. Our MURI team has also selected two baseline nozzle materials for in-depth research. Both of these nozzle materials can resist erosion under harsh flow environment. The high quality bulk graphite (such as G90) or carbon-carbon composite materials can resist erosion for both types of propellants and is therefore selected as one of the baseline nozzle material. The copper infiltrated tungsten can also resist erosion in solid rocket motor and scramjet propulsion conditions when metallized propellants are used. Therefore, it is selected as second baseline nozzle material.

The advantages and limitations of many of these potentially beneficial materials for zero-erosion performance in solid and airbreathing tactical missile nozzles have been discussed by Opeka.<sup>1-4</sup> Wolt and Webber<sup>5</sup> recently demonstrated a nozzle boundary-layer cooling system (NBLCS) as a means to mitigate nozzle throat erosion at conventional pressure levels for solid rockets. However, nozzle erosion data are scarce especially at high-pressure operating conditions. Theoretical and experimental understanding of the erosion rates of these selected materials in high-pressure rocket environments (for metallized and non-metallized propellants) are critical in order to design future rocket nozzles for advanced propulsion systems to operate with high propulsive performance at pressures on the order of 5,000 psi (35 MPa) or even 8,000 psi (55 MPa). However, the heat transfer rates to the nozzle throat increase strongly with chamber pressure. Therefore, the investigation of rocket nozzle erosion under ultrahigh-pressure conditions is urgently needed for future propulsion system development and for enhancing agility of missile systems.

In the consideration of minimizing rocket nozzle throat erosion, it is beneficial to consider many detailed processes listed below:

- Convective & radiative heating of nozzle surface in the vicinity of the throat and heating of nozzle material to elevated temperatures;
- Gas-phase reaction in the shear layer at the nozzle throat;
- Diffusion of gas-phase chemical species from core-flow region to the surface;
- Adsorption of chemical species and heterogeneous reaction at the nozzle surface;
- Formation of oxides, carbides, and nitrides near surface at the nozzle throat;
- Diffusion of chemical species in the matrix of nozzle material to form solid solution;
- Liquid particle impact and deposition on surface;
- Thermal/mechanical stresses induced microstructural damage (microcracks) in the matrix of nozzle material;
- Subsurface phase transformation, grain growth, coarsening, creep due to rapid heating;
- Formation of superficial scales;
- Removal of molten material by shear flow;
- Pyrolysis & evaporation of nozzle material; and,
- Spallation of damaged portion of the nozzle material.

To address these issues, which have very broad scope nature, the present **MURI** team with researchers of different disciplines from six universities, has been exploring different aspects of the **Rocket Nozzle Erosion Minimization (RNEM)** program. In particular, our team is exploring new technologies for characterization of the nozzle materials erosion rates and mechanisms at high-pressure and high-temperature conditions. Models for predicting erosion rates at these conditions are being developed with validation to be conducted by comparison with experimental data. Specific approaches adopted and accomplished made by different groups are discussed in the later sections.

### Organization

In order to achieve in-depth understanding of the complex physicochemical processes, this **MURI** program makes use of a combination of various skills mastered by different groups of researchers from the six universities: the Pennsylvania State University (**PSU**), the University of Illinois at Chicago (**UIC**), Emory University (**Emory**), University of Texas-Austin (**UTA**), Ohio State University (**OSU**), and the Georgia Institute of Technology (**GaTech**). The team consists of mechanical engineers and combustion scientists with expertise in high-pressure combustion, solid propellant rocket motor operations, and high-pressure/high-temperature chemical kinetics (**Kuo, Yetter**), chemists with expertise for heterogeneous and gas-phase reaction kinetics rate determination (**Lin, Musaev, Irle, Brezinsky, Wilkinson**), material scientists for rocket nozzles and high-temperature ablative compounds (**Koo, Morral**), theoreticians for simulation of nozzle erosion mechanism and rate prediction (**Yang, Menon, Kuo**), scientists for diagnostics of nozzle material phase transition and erosion phenomena (**Hangud, Seitzman, Wilkinson**), and specialist in structural mechanics of carbon-carbon composite material (**Costanzo**).

The kickoff meeting for the MURI program was held on August 27, 2004 at the Arlington, VA. A summary of the meeting can be found at the MURI website (<http://www.mne.psu.edu/muri-rnem/index1.htm>). The present report provides a brief description of scientific progress and accomplishments over the last year. In addition, interactions and technology transfer among the team members and with DoD scientists are described. Finally, publications, presentations, and demographics of the program are reported.

### Objectives and Approach

The main objective of this **MURI-RNEM** project is to achieve in-depth understanding of the thermochemical and mechanical erosion processes of nozzle materials for facilitating future development of advanced solid rocket motors for high-pressure applications, while developing the required chemical kinetic mechanisms and obtaining transport data for model solution; as well as to select solid propellant formulations for minimizing erosion rates. The overall method of approach for rocket nozzle erosion minimization (RNEM) study is illustrated in **Fig. 1**.

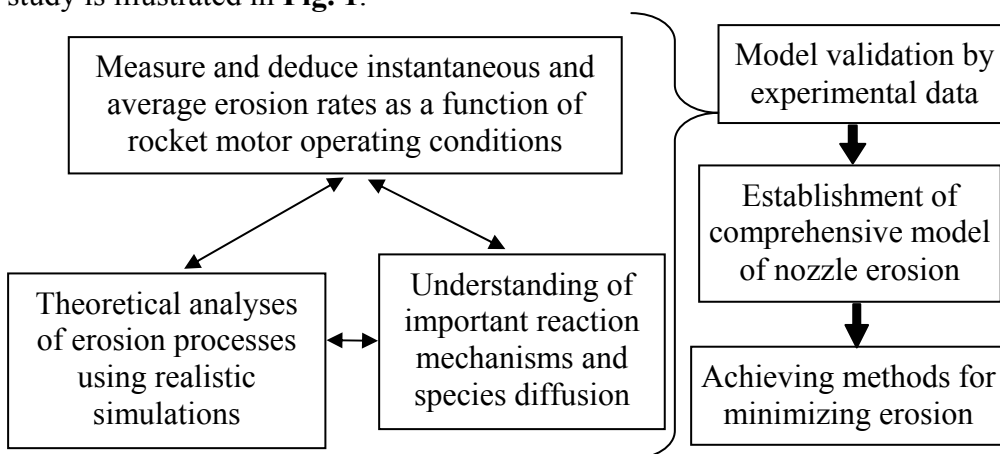


**Figure 1.** Overall Method of Approach for Rocket Nozzle Erosion Minimization (RNEM)

During this reporting period, the specific tasks and objectives of different research groups are given below:

#### **Kuo Group at PSU:**

- Characterization of nozzle erosion processes as functions of nozzle material, propellant composition, and flow conditions in two separate experiments; one with a rocket motor simulator (RMS) and the other with an ultra-high pressure rocket motor.
- Upgrading of a comprehensive theoretical model and numerical code for predicting graphite nozzle recession rate to facilitate the understanding of the erosion process, and to include more detailed kinetics and transport properties.

#### **Yetter Group at PSU:**

- Heterogeneous surface oxidation, carburization, and nitration studies of bulk tungsten, rhenium, and hafnium by conducting flow reactor experiments to gather kinetic data for developing surface reaction mechanisms.

**Yang Group at PSU:**

- Modeling and simulation of nozzle material erosion by a comprehensive theoretical model that includes the surface chemistry for the pyrolysis and thermal degradation of carbon-carbon or graphite materials, using a LES numerical code with parallel processing.

**Brezinsky Group at UIC:**

- Measurement of gas-phase and heterogeneous reaction rates of carbon powders at high-pressure and high-temperatures conditions generated in a shock tube.

**Lin, Musaev, and Irle Group at Emory:**

- Investigation of reactions of  $\text{H}_2\text{O}$ ,  $\text{CO}$ ,  $\text{NO}$  and  $\text{H}$  with graphite with and without defects using exploratory QM/MD trajectory calculations under high temperatures and high pressures, to further investigate transition states using DFT, ONIOM, and VASP, and to calculate the rate constants for these reactions.
- Study of the reaction mechanisms of  $\text{W}/\text{W}^+$  with  $\text{H}_2\text{O}$ ,  $\text{CO}$ ,  $\text{CO}_2$ ,  $\text{NO}$  and  $\text{NO}_2$  at their ground and several lower-lying excited electronic states using the most accurate electronic structure methods.

**Koo Group at UTA:**

- Assistance in nozzle material selection by literature survey, to provide and material property data for **MURI-RNEM** team members, and to maintain a computerized library database for use by the **MURI** team.

**Hanagud, Wilkinson, and Seitzman Group at GaTech:**

- Investigation of the crystalline-to-crystalline transformations, which occur on the nozzle throat surface due to processes such as oxidation and temperature-induced phase transitions, and to provide a time line for these processes.
- Design and fabrication of a nozzle erosion test facility for synchrotron X-ray diffraction and imaging diagnostic technique to determine real-time nozzle erosion process.
- Consideration of zirconium carbide nozzle fabrication.

**Menon Group at GaTech:**

- Simulation of rocket combustion product flow through a choked nozzle with isothermal wall conditions to determine local heat flux and surface shear forces on the walls.
- Development of a “small-scale” subgrid model from first principle that accounts for surface erosion due to external forces and couple this erosion subgrid model within the LES/DNS code.

**Morral Group at OSU:**

- Preparation of literature survey on the oxidation, carburization and nitration of bulk tungsten, tungsten/copper composites, rhenium, tantalum and hafnium as well as oxidation of graphite and carbon/carbon composites.

- Compilation of thermodynamic and kinetic databases for nozzle materials that can be applied to predicting multi-component phase diagrams and diffusion kinetics using Thermo-Calc and DICTRA software.

### Scientific Progress and Accomplishments

## 1. Design of a Rocket Motor Simulator (Kuo Group at PSU)

### 1.1 Simulation of Propellant Product Species to Match Those of Propellant S

To study the effects of combustion product species and temperature on nozzle throat erosion rate, two combustion systems have been designed. One is an actual high-pressure rocket motor to be discussed later; the other is a gas/liquid combustor to simulate the combustion products generated from a non-metallized Propellant S. The goal for the gas/liquid combustor is to vary the composition of the product species by controlling the inlet flow rates of various reactants. The major advantage of this simulator is the ability for systematic variation of the simulated propellant product composition for determining their respective influence on the nozzle erosion rate. To determine which reactants will be needed, a series of calculations using the NASA-CEA code was performed by varying the concentrations of fuels, oxidizers and additives to obtain a similar product composition as that of Propellant S. It is shown in Table 1 that burning a gas/liquid mixture containing: 15 wt% methane, 50% oxygen, 25% HCl, 7.5% nitrogen, and 2.5% water will generate products similar in composition to that of Propellant S. It is useful to note that even though not all the species have close simulation of their concentrations to that of the Propellant S, this simulation result indicates the possibility for varying the reactant flow rates to closely simulate the concentrations of certain interesting species, such as H<sub>2</sub>O.

Table 1 Species Molar Fraction Comparison of Propellant S at 1000 psia

Products of Propellant S		Products of Gas Mixture	
H <sub>2</sub> O	0.43005	H <sub>2</sub> O	0.43502
HCl	0.18374	HCl	0.15743
CO <sub>2</sub>	0.13306	CO <sub>2</sub>	0.1146
N <sub>2</sub>	0.09858	N <sub>2</sub>	0.06576
CO	0.08863	CO	0.1188
H <sub>2</sub>	0.04113	H <sub>2</sub>	0.05977
Cl	0.00814	Cl	0.01351
OH	0.00779	OH	0.01938
H	0.00266	H	0.00762
FeCl <sub>2</sub>	0.00158	FeCl <sub>2</sub>	-----
O <sub>2</sub>	0.00132	O <sub>2</sub>	0.00429
NO	0.00103	NO	0.00215
Al <sub>2</sub> O <sub>3</sub> (l)	0.00082	Al <sub>2</sub> O <sub>3</sub> (l)	-----



## 1.2 Justification for Removing Chlorine from the Rocket Motor Simulator

A literature survey was conducted in order to find the possible reactions and the reaction kinetics of halogens (particularly chlorine) with graphite. In the work by Freedman,<sup>6</sup> basal plane of graphite were exposed to beams of atomic and molecular fluorine and chlorine in an ultrahigh vacuum environment. X-ray photoelectron spectroscopy (XPS) and low-energy electron diffraction techniques were used to elucidate the chemistry involved. The carbon 1s XPS spectra of halogenated HOPG graphite basal plane, which have been exposed to atomic chlorine, was compared to those of annealed samples of graphite. It was found that both spectra were identical to each other. This implies that exposure of the HOPG substrates to molecular chlorine produced no evidence of any uptake of chlorine. Furthermore, only an extremely small quantity (barely above the noise level) of chlorine could be measured by monitoring the 2p peak of Cl. This small quantity of adsorbed chlorine could be entirely the result of the presence of edge planes exposed during the cleaving process; the edge plane of graphite is much more reactive than the basal plane. These results were in accordance with high-pressure data that indicate that graphite etching by fluorine occurs primarily by attack at the edge (prism planes) of graphite. This low reactivity of graphite basal plane to chlorine (and fluorine) is ascribed to the combination of steric and energetic factors, which mitigates against the disruption of the infinite two-dimensional ring structure of the basal plane. The edge (prism) plane of graphite, on the other hand, contains dangling bonds which are readily available for reaction. In another significant work by Pasquevich and co-workers,<sup>7</sup> the oxidation reaction of carbon black, sucrose carbon and graphite in the presence of chlorine was studied by thermal analysis (TGA and DTA). Heating in chlorine caused different degrees of mass increase in each of the three carbons, with two reaction zones due to physisorption and chemisorption of chlorine on the carbon surface. Heating the three carbons in chlorine atmosphere showed that graphite exhibited the smallest mass gain (0.5%) of all three carbons. The chlorine uptake by graphite is due to the joint effect of physisorption at low temperatures (473-573 K) and chemisorption (above 673 K). It was also shown that the oxygen uptake by graphite does not change in the presence of chlorine and vice-versa. Burning of the carbons in the presence of chlorine showed its inhibiting effect, being weakest in graphite. Oxidation in absence of chlorine started at 933 K for graphite. When chlorine was present in the gaseous phase, oxidation started at 1043 K. But since the temperatures at the nozzle surface are going to be much higher than 1043 K, this difference in oxidation temperature is not important.

In another work by Henning,<sup>8</sup> it is shown/suggested that chlorine reacts with graphite at low temperatures only. The graphite sample used was pitch-bonded graphite brominated in carbon tetrachloride solution of bromine and it was suspended in liquid chlorine at -33 C and after three days the electrical resistance of graphite sample decreases only by 0.1 Ohms. In the vapor phase, the reaction was even slower. It was stated in a work by Norman and co-workers<sup>9</sup> that physisorbed chlorine on a carbon cloth had a large influence on the interaction of the carbon with water, while chemisorbed chlorine had only a small effect.

Based on these studies, it can be concluded that the reaction of graphite with Cl is negligible and the presence of Cl atoms in the vicinity of the nozzle surface does not affect graphite reactions with other oxidizing species.

### 1.3 Simulation of Product Species of Propellant S in the Rocket Motor Simulator

The primary purpose of the RMS is to study the effects of specific product species on nozzle throat erosion rate. Based on the results presented above, chlorine and HCl can be eliminated from the important reaction species in the nozzle erosion process for propellant S with graphite nozzles. In addition, it is known that Cu infiltrated W nozzles do not work well with the products of Propellant S (as shown by the third quarterly report of Yetter, et al.). Because of these findings, chlorine compounds have been eliminated from the reactants to be utilized in the study of graphite nozzle erosion process in the RMS. Instead of attempting to study the effects of all the products listed in the above section, two particular product species, water ( $\text{H}_2\text{O}$ ) and hydroxyl radical ( $\text{OH}$ ), were found to be the primary reactants in the graphite nozzle erosion process. The rate of reactions between  $\text{CO}_2$  and graphite is significantly lower than that of water vapor and hence can be disregarded, based upon the work of Chelliah, et al.<sup>10</sup> The effects of the remaining product species are believed to be secondary in causing reactions with the graphite nozzle. Some of the other product species, such as  $\text{O}_2$  and  $\text{O}$ , have extremely low mole fractions and therefore their effects on erosion rate are negligible. The NASA-CEA code was continued in its use for this application, but instead of finding a best match for all the product species of Propellant S, a close match of the two primary product species ( $\text{H}_2\text{O}$  and  $\text{OH}$ ) and the flame temperature has been emphasized.

To simplify the reactant injection system, the water line was eliminated since water vapor is generated in the combustion products of hydrocarbons. The spray of HCl can also be avoided based upon the above observations. With the elimination of both liquid water and HCl in the reactants, the rocket simulator now only uses gaseous reactants to generate important product species and a temperature close to that of Propellant S. Table 2a shows the results of NASA-CEA code simulations of the equilibrium products of a gaseous mixture containing: 2.27 wt% hydrogen, 15% methane, 28.18% nitrogen, and 54.55% oxygen. As given in Table 2a, the product species concentrations of  $\text{H}_2\text{O}$  and  $\text{OH}$  at the nozzle throat are very close to those of Propellant S. The simulated gas temperature of 2,980 K at the nozzle throat is also very close to that of Propellant S at 2,801 K. We will definitely compare the results from our rocket motor simulator with the solid-propellant rocket motor to verify the insignificant effect of HCl on nozzle erosion. In case HCl has non-negligible effect, we can always add a liquid HCl spray injector line to the rocket motor simulator at a later time.

As mentioned above, the primary purpose of the RMS is to study the effect of a given chemical species concentration on the nozzle erosion rate using systematic variation of reactant mass flow rates. Since the study has been focused on the product species  $\text{H}_2\text{O}$  and  $\text{OH}$ , at least one of these products should be varied independently. Since water is one of the primary products in any hydrocarbon combustion, it is very difficult to simulate a reaction that will drop it to a comparatively low level. However,  $\text{OH}$  is a radical that can be varied by simply adjusting the initial concentrations of fuel and oxidizer. In particular when the inlet flow rates of oxygen and hydrogen are

increased and methane flow rate is decreased, a product species with H<sub>2</sub>O at a similar molar fraction to that of Propellant S is formed, while the OH levels drop significantly. This means that the effect of OH will be very noticeable on the nozzle recession rate and thus more easily studied. Given in Table 2b are the equilibrium combustion products of the gaseous mixture of 11.29 wt% hydrogen, 11.29% methane, 9.68% nitrogen, and 67.74% oxygen. Notice that the OH mole fraction in the gas mixture dropped to a level of about 20% of the value that is in the product of Propellant S while the H<sub>2</sub>O mole fraction in the gas mixture remains the same as the H<sub>2</sub>O level in Propellant S. Again, the gas mixture temperature at the throat can be maintained in the close vicinity of Propellant S (~80 K difference).

Tables 2a and 2b. Comparison of mole fractions of the two major oxidizing species with those in the product of Propellant S for two different gas mixtures

a)			b)		
	H <sub>2</sub> O	OH		H <sub>2</sub> O	OH
Propellant S	0.430	0.00779	Propellant S	0.430	0.00779
Gas Mixture A	0.434	0.00848	Gas Mixture B	0.424	0.00164

The simulation of the product species of Propellant M has proven to be more difficult because of the high level of aluminum content in the propellant composition. The primary problem is the practical implementation of this propellant formulation in the RMS. A thermo-chemical equilibrium program was used to simulate the reactants in this case as well. It was found to be difficult in achieving a close match for the metallized propellant case using gas/liquid reactant mixtures. In addition, it was found that the closest species match requires that almost 25 wt% of the reactants to be aluminum particles. Further research has shown that high flow rate with such a high percentage of aluminum and the low O/F ratios required for product species similarity result in many problems. Therefore, the Propellant M composition will not be simulated by the RMS. Instead, actual Propellant M will be utilized in rocket motor firings discussed in a later section.

#### 1.4 RMS Design Description

After the determination of the desirable percentages of reactants in the gas mixtures for RMS, the next process was the design of the main body of the rocket motor combustor, injectors, reactant supply system, and exit nozzle.

##### *1.4.1 Main Body of Rocket Motor Simulator*

In order to study the high-pressure nozzle erosion process, a heavy-walled combustor with multiple instrumentation ports has been adopted. An existing instrumented high-pressure combustion simulator (IHPCS) constructed from 316L stainless steel will be utilized as the combustor of the RMS (shown in **Fig. 2**). This rocket motor simulator will be operated for nozzle erosion experiments at chamber pressures up to 8,000 psig.

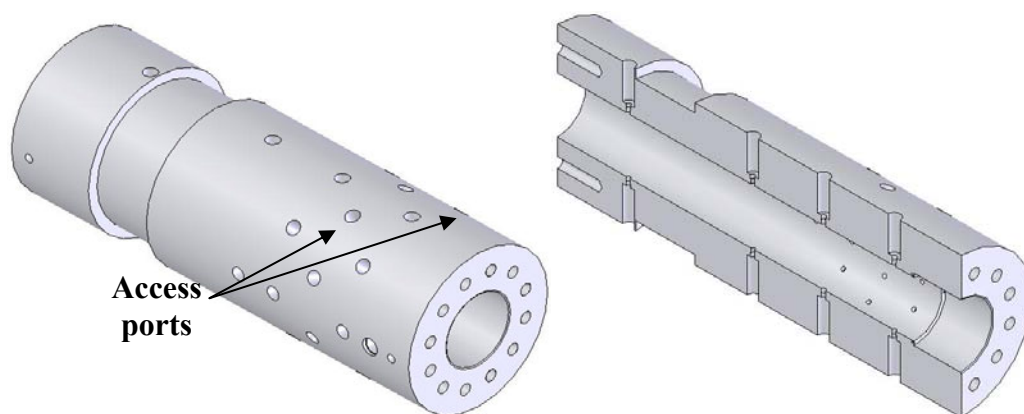


**Figure 2.** Drawings of the rocket motor simulator (RMS) with inner diameter of 12 cm

The RMS has a large free volume (2,565 cc) and an internal diameter of 12 cm. This diameter corresponds very closely to the diameters being considered for the propellant motor casing ( $\sim 12$  cm) of the rocket motor. The RMS has an O.D. of 30.5 cm and an overall length of 87 cm. It is also equipped with numerous diagnostic access ports (30) located around the chamber. These ports contain a  $3/8''$ -24 thread that can be used to mount pressure transducers around the motor. If these pressure measurements are not desired during testing, the ports can be used for instrumentation such as OH concentration measurements by absorption spectroscopic technique. Other unused ports will be plugged. One of the benefits of having a 316L S.S. chamber to hold the rocket motor is that the material has a very high ultimate tensile strength (70.3 ksi) and resistance to corrosion. To protect the internal chamber surface, the RMS can be lined with  $1/2''$ -thick paper-phenolic tubing. This reduces the operating internal diameter of the RMS down to  $\sim 9.53$  cm. The RMS has been hydrostatically tested to 180.7 MPa or 26,200 psig which is more than three times the maximum operating pressure desired for the high-pressure rocket motor ( $\sim 8000$  psig).

The RMS will be mounted onto a test rig that consists of 4 I-beams and a  $3/8''$ -thick steel plate as seen in a drawing of the test rig in Fig. 3. The RMS will be held in place by a low-carbon steel cradle, which wraps around the entire RMS and securely bolted to the test rig to prevent any upward or side movement. The reacting gaseous fuel mixture will enter from the injector side at the head end of the RMS, while the oxidizer will be injected tangentially into the combustor at a station near the cradle assembly. More detailed discussion of the swirl combustor design is given in a later section. The RMS is held in place by a 1"-thick heavy-duty angled steel bracket, which will absorb the thrust during testing.

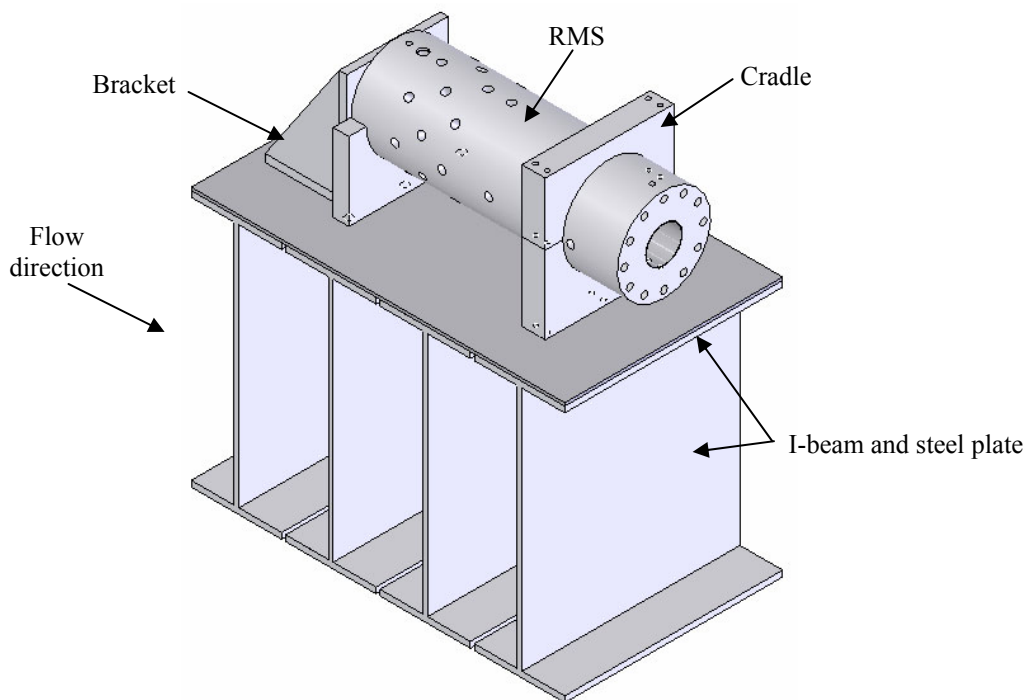


**Figure 3.** Schematic drawing of the RMS test rig.

#### *1.4.2 Reactant Supply System*

Based upon the selection of the reacting gas mixture, it was determined that for the combinations of mass flow rates required, bottle pressure reservoirs of  $\text{CH}_4$ ,  $\text{H}_2$ ,  $\text{O}_2$ , and  $\text{N}_2$  would be sufficient for the RMS testing under relatively low pressures ( $\sim 1,300$  psia). Although these commercially available bottle pressure levels reach a maximum of  $\sim 2,300$  psia, by using appropriate feed lines and orifices, the operating pressure in the RMS would be capable of reaching 1,300 psi.

The overall reactant supply system is shown in Fig. 4. The  $\text{CH}_4$ ,  $\text{H}_2$ , and  $\text{O}_2$  will be introduced into the RMS from a manifold of several commercially available gas bottles, with the upstream pressure levels controlled by a regulator. The nitrogen will be supplied from an existing compressor system (with a maximum pressure capability of 30,000 psig) and will be used not only as a reactant gas, but also as a purge gas. By compressing the nitrogen gas before the test, a sufficient quantity and pressure of nitrogen for the purge can be guaranteed.

A series of ball valves (BV) and check valves (CV) will be used to ensure that gases will not be unintentionally mixed. For instance, should an over-pressurization occur in the chamber, the check valves in the flow system will automatically close and no hot product gas will be allowed to travel back into the feed lines and gas bottles. By using remotely activated ball valves, the test will be started and stopped by a computer-controlled sequencing program. Also, the ball valves in the feed system will be set to close should the system lose power for the fuels and oxidizer, and the purge valves will automatically open.

As mentioned before, in order to match the correct species concentration, a constant mass flow rate of all four reacting gases is required. These constant mass flow rates will be obtained by the use of sonic orifices placed in each line. The diameter of the sonic orifice along with the upstream and downstream pressures will be used to determine the mass flow rate through each orifice. The mass flow rate will remain constant as long as the pressure downstream of the orifice remains sufficiently below the upstream pressure. Therefore, due to the limitations of the commercial gas bottles, the maximum operating chamber pressure in the RMS can reach only 1,300 psia. When the commercial gas bottles are replaced by other high pressure reservoirs, the RMS can then be operated at much higher pressures (~8,000 psia).

In order to achieve variation of concentrations of product species, a broad range of reactant mass flow rates is required. To obtain all of the required flow rates, different orifice diameters have been designed since the upstream bottle pressure is limited. This was accomplished by designing an orifice assembly with interchangeable orifice plates for easy installation for obtaining different flow rates. By varying both the upstream pressure and the orifice diameter, all of the required flow rates can be obtained. Pressure transducers and thermocouples will be installed in each line so that the pressure upstream and downstream of the orifice will be recorded, providing the exact flow rates for each test.

#### *1.4.3 Injectors for Gaseous Reactants*

Several designs have been considered to inject the gaseous reactants into the RMS. These include coaxial, impinging, and radial injections. Although the coaxial and impinging jet designs can be fabricated, the concern of flame holding and chamber heating has ruled out those options. After reviewing recent work in the field of vortex combustion chambers,<sup>11,12</sup> interest in the injector design has shifted toward that used in a vortex combustor, shown in **Fig. 5**.

As can be seen in **Fig. 5**, the outer annular region of swirling gaseous oxygen confines the inner tubular reacting core, creating a co-spinning bi-directional vortex flow field. This outer vortex is induced by the interaction of the tangentially injected oxidizer flow with that of the inner tubular core flow. The angular momentum of the oxidizer flow supports the uprising motion of the outer vortex. Upon mixing with the fuel stream (a combination of gaseous fuels  $\text{CH}_4$  and  $\text{H}_2$ , with certain amount of  $\text{N}_2$  as diluent) from the head-end region, the mixed stream continues to form a swirling flow with reversed axial direction. An added benefit to this type of injector design is that the outer vortex acts as a combustor wall coolant, protecting the chamber wall from high rates of heat transfer, minimizing erosion of the chamber wall. In addition, a stable flame with prolonged mixing duration is created from the vortex flow. In this configuration minimal wall erosion will occur inside the RMS, extending the engine's lifetime, and focus can be turned toward the exit nozzle erosion. In the adoption of this combustor design, the nozzle will not be cooled by incoming oxidizer.

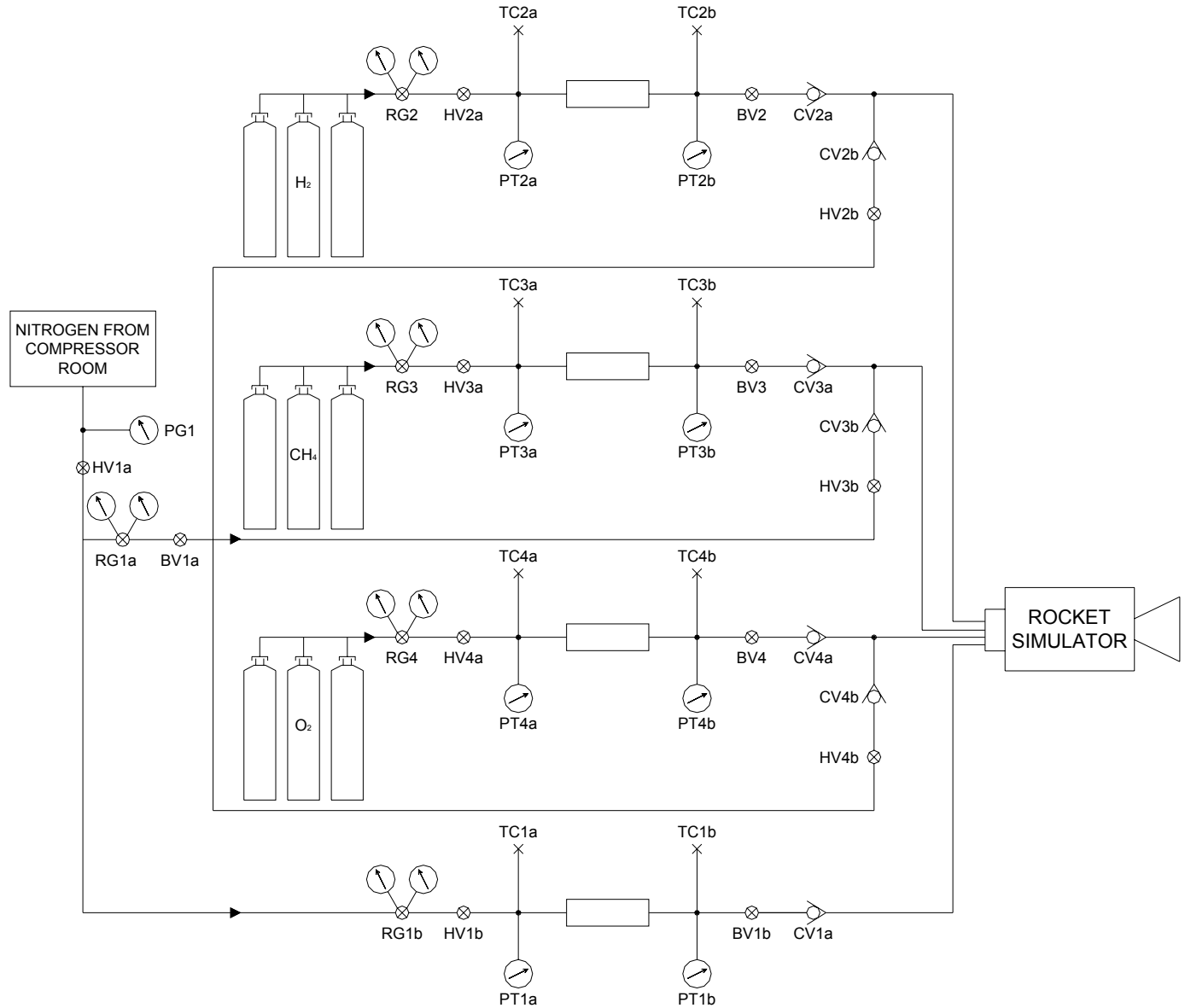


**Figure 4.** Process flow diagram for supply/control of reactants for the rocket motor simulator

Also, the axial distance between the oxidizer swirl injectors and the throat of the nozzle will be selected to have sufficient separation so that the strength of the inner vortex will be reduced before the hot combustion product gases enter the convergent portion of the nozzle. The purpose for reducing the vortex strength is to simulate the actual solid-propellant rocket motor flow conditions near the throat.

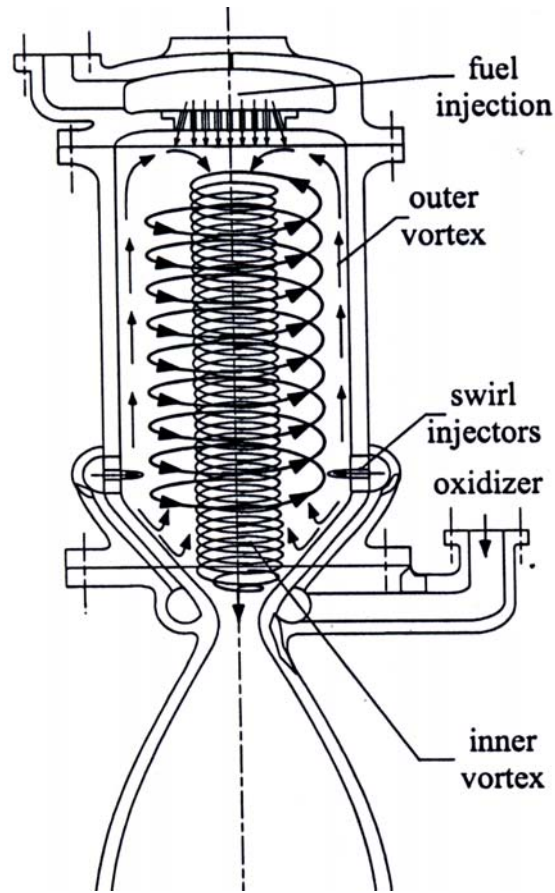


Figure 5. Schematic showing a typical vortex combustor design (Ref. 12)

### 1.5 Baseline X-ray Transparent Nozzle

The initial design of the exit nozzle of the RMS can be seen in **Fig. 6**. The entrance and nozzle will be made of G90 graphite. The entrance piece will cause the incoming flow from the axisymmetric port area to converge into the inlet of the 2-D nozzle. The nozzle piece converges from the inlet area to the throat area while maintaining the same channel width (i.e., only the height of the nozzle changes in the axial direction). The outer X-ray translucent sleeve surrounding the nozzle will be made of a fiberglass material solidified with a high temperature epoxy. The nozzle retainer will be held on with breakaway bolts to be used for the planned failure mode. The main nozzle housing piece also functions as the chamber end cap. This component contains a piston seal for maintaining the pressure in the chamber. This design is also going to be utilized for the solid propellant rocket motor.

It is useful to note that the 2D nozzle we designed has a divergent section in order to expand the flow from high pressure to the ambient pressure. For nozzle throat erosion study, the divergent section could be cut to a shorter length with lower area expansion ratio. However, we chose our design geometry to generate a reasonably sized exhaust jet



for video recording of the stability of the plume jet. The stability of the combustion processes inside the engine can be reflected from the steadiness of the exhaust plume jet. In the test rig mounting arrangement, there is no problem for us to hold the engine in place, since the test frame is extremely strong. The small amount of thrust generated by the discharging jet will be absorbed by the test frame.

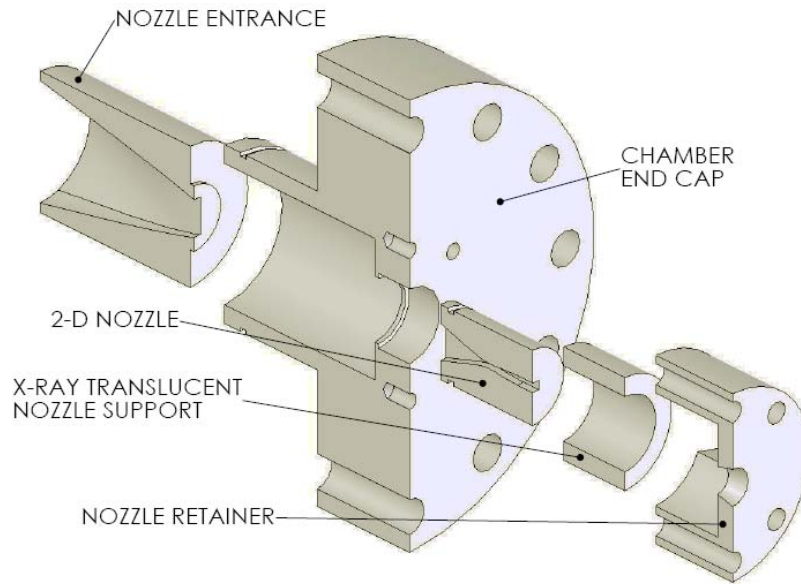


**Figure 6.** Exploded view of exit nozzle

### 1.6 Nozzle Assembly with Boundary-Layer Control Mechanism

Based on conversations with Mr. Jerry Webber of NAWC-China Lake regarding the results of the newly developed Nozzle Boundary Layer Control System (NBLCS)<sup>5</sup>, a second X-ray translucent nozzle configuration is being developed that will allow the introduction of decomposed chemical species from the ablative material into the nozzle throat region to cool the combustion product gases in the boundary-layer region at the throat. The introduction of the products of the sublimated materials upstream of the nozzle throat not only reduces the temperature of the gases in the boundary layer but also introduce chemical species with significantly reduced reactivity with graphite. Highly encouraging results were demonstrated with this boundary-layer control system with average erosion rates 80% lower than that of the baseline-uncooled nozzle system. After the coolant blocks were consumed, nozzle erosion rates returned to uncontrolled levels (~10 mils/s).

Implementation of a similar design into the modular X-ray translucent nozzle configuration will allow the evaluation of the effects of both controlled boundary-layer flow and non-controlled boundary layers (utilizing the initial baseline configuration discussed previously) on the erosion process. Information including the gas-phase temperature required for the onset of oxidative reactions in the nozzle throat, currently an unknown quantity, can be deduced through the systematic variation of the mass of sublimated material introduced to the boundary layer upstream of the nozzle throat. This data can be utilized in the understanding of the reaction kinetics affecting the erosion of

the nozzle throat material. In turn, the Graphite Recession Code (GRC) can be modified to include the newly developed kinetics and further advance the ability of the numerical prediction of the nozzle erosion process. Additionally, the effectiveness of a boundary-layer control device under increased radiative heat transfer from the combustion of aluminized propellant can be evaluated, which currently is an area that has not been considered.

### 1.7 Flow Field Calculations Using Fluent Code

To examine the turbulent boundary-layer thickness relative the half-height of the 2-D nozzle, Fluent Code (version 6.1) was utilized to conduct the computation for the combustor pressure of 1000-psia. The purpose is to make sure there is a core region at the throat so that the viscous effect is limited to the wall region. The computed velocity profile at the nozzle throat is shown in **Fig. 7** indicating the existence of a core region for a nozzle throat height of 3.30 mm.

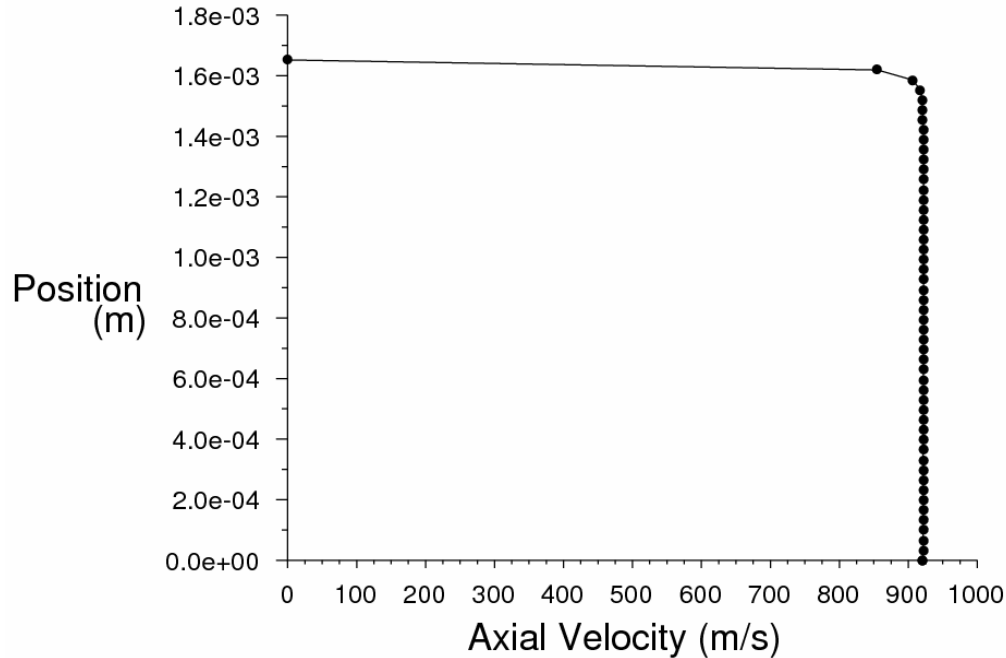


**Figure 7.** Axial velocity profile vs. vertical distance from axis at nozzle throat

## **2. Design of a High-Pressure Rocket Motor (Kuo Group at PSU)**

### 2.1 Pressure Independence of Product Species

The combustion product composition of Propellant M at the nozzle throat location was calculated as a function of chamber pressure by this team and is given in Table 3. It is quite obvious that the pressure dependency of the chemical species composition at the nozzle throat and rocket motor chamber are very weak. Also, the concentrations of O, H, OH, and Cl are very low. This implies that the three-body collision process suppresses

the dissociation processes of chemical species at high pressures. Essentially, the concentrations of chemical species do not differ any significant amount for P=1,000 to 9,000 psi. The product composition generated from the propellant combustion is of main concern and this information was distributed to MURI team members.

Table 3. Mole fractions of product species and thermodynamic parameters of Propellant M at nozzle throat location.

Chamber Pressure (psi)	1000	3000	5000	7000	9000
H <sub>2</sub>	0.28365	0.29022	0.29303	0.29477	0.29602
CO	0.21515	0.21739	0.21834	0.21894	0.21937
HCl	0.13530	0.13786	0.13842	0.13852	0.13844
H <sub>2</sub> O	0.12003	0.12191	0.12264	0.12309	0.12342
Al <sub>2</sub> O <sub>3</sub> (l)	0.09063	0.09175	0.09215	0.09234	0.09245
N <sub>2</sub>	0.07929	0.08007	0.08039	0.08059	0.08074
H	0.03316	0.02346	0.01966	0.01741	0.01585
CO <sub>2</sub>	0.01132	0.01118	0.01112	0.01109	0.01107
Cl	0.01049	0.00736	0.00613	0.00539	0.00488
OH	0.00590	0.00434	0.00369	0.00330	0.00302
AlCl	0.00507	0.00409	0.00359	0.00326	0.00302
AlOH	0.00413	0.00337	0.00299	0.00273	0.00255
AlOHCl <sub>2</sub>	0.00075	0.00144	0.00191	0.00230	0.00262
FeCl <sub>2</sub>	0.00099	0.00128	0.00138	0.00144	0.00148
AlOHCl	0.00059	0.00079	0.00088	0.00094	0.00097
Al(OH) <sub>2</sub> Cl	0.00025	0.00049	0.00066	0.00080	0.00092
AlCl <sub>2</sub>	0.00041	0.00053	0.00058	0.00062	0.00064
AlCl <sub>3</sub>	0.00015	0.00028	0.00037	0.00044	0.00050
AlOCl	0.00039	0.00032	0.00028	0.00026	0.00024
Al(OH) <sub>2</sub>	0.00017	0.00024	0.00027	0.00029	0.00030
NO	0.00039	0.00030	0.00026	0.00023	0.00022
Fe	0.00060	0.00034	0.00025	0.00020	0.00017
Al(OH) <sub>3</sub>	0.00007	0.00014	0.00020	0.00024	0.00028
O	0.00041	0.00021	0.00014	0.00011	0.00009
P_throat (psi)	578.7	1733.4	2887.0	4040.3	5193.5
T_flame (K)	3532.5	3630.2	3670.0	3694.0	3710.8
T_throat (K)	3347.7	3427.1	3458.7	3477.5	3490.5
gamma throat	1.128	1.133	1.135	1.136	1.136
Average M <sub>w</sub> at throat	27.14	27.40	27.50	27.58	27.63
Cp throat (kJ/kg-K)	3.698	3.1747	2.9747	2.8574	2.7771

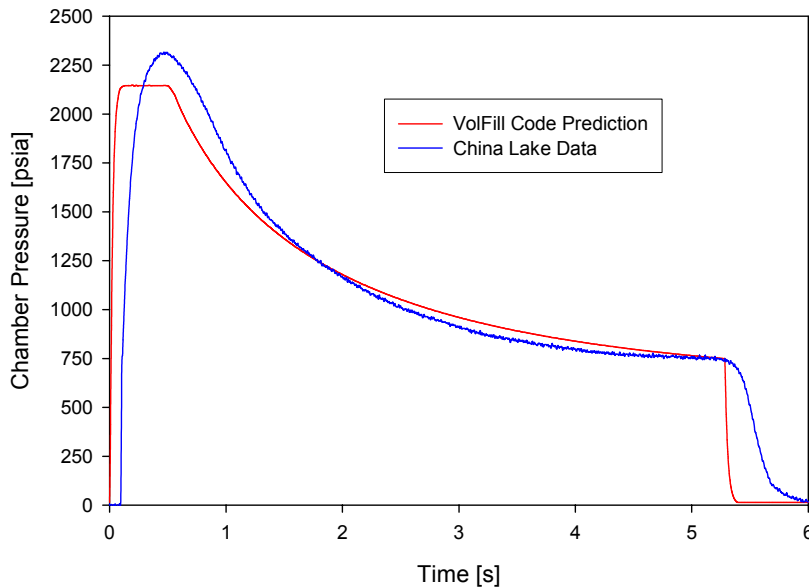
The non-metallized Propellant S was adopted due to its ability to burn at high pressures up to 8,000 psia. Again, the combustion products and thermodynamic properties at the nozzle throat region and rocket motor were calculated by this team and the results were distributed to the MURI team members. The combustion product composition of Propellant S at the nozzle throat location was tabulated as a function of chamber pressure in Table 4. Again, it is quite obvious that the pressure dependency of the chemical species composition at the nozzle throat and rocket motor chamber are very weak. This non-metallized propellant can generate substantial amount of oxidizing species such as H<sub>2</sub>O vapor (39 mole%) and CO<sub>2</sub> species (11 mole %).

Table 4. Mole fractions of product species and thermodynamic parameters of Propellant S at nozzle throat location.

Chamber Pressure (psi)	1000	3000	5000	7000	9000
H <sub>2</sub> O	0.43005	0.43411	0.43564	0.43653	0.43706
HCl	0.18374	0.18628	0.18698	0.18734	0.18782
CO <sub>2</sub>	0.13306	0.13571	0.13672	0.13731	0.13766
N <sub>2</sub>	0.09858	0.09918	0.09944	0.09960	0.09968
CO	0.08863	0.08704	0.08647	0.08615	0.08592
H <sub>2</sub>	0.04113	0.03950	0.03893	0.03861	0.03840
Cl	0.00814	0.00551	0.00450	0.00392	0.00353
OH	0.00779	0.00544	0.00450	0.00393	0.00356
FeCl <sub>2</sub>	0.00158	0.00159	0.00159	0.00159	0.00159
H	0.00266	0.00171	0.00137	0.00118	0.00106
AlOHCl <sub>2</sub>	0.00038	0.00071	0.00094	0.00109	0.00110
Al(OH) <sub>2</sub> Cl	0.00027	0.00051	0.00068	0.00079	0.00080
NO	0.00103	0.00076	0.00064	0.00057	0.00052
Al(OH) <sub>3</sub>	0.00020	0.00037	0.00049	0.00058	0.00058
O <sub>2</sub>	0.00132	0.00064	0.00044	0.00034	0.00028
Al <sub>2</sub> O <sub>3</sub> (l)	0.00082	0.00044	0.00018	0.00000	0.00000
O	0.00032	0.00015	0.00010	0.00007	0.00006
P_throat (psi)	573.6	1712.0	2850.4	3980.0	5113.6
T_flame (K)	2996.2	3054.4	3077.7	3091.4	3100.9
T_throat (K)	2801.2	2837.4	2850.2	2856.4	2861.4
gamma throat	1.158	1.167	1.171	1.178	1.180
Average M <sub>w</sub> at throat	26.53	26.65	26.71	26.74	26.75
Cp throat (kJ/kg-K)	2.829	2.483	2.360	2.275	2.228

## 2.2 Rocket Motor Design Using Volume Filling Code

To determine the required throat size for a given test run of either the solid-propellant rocket motor or the RMS, a volume filling code was developed to predict the pressure in the absence of throat erosion. Verification of the code was completed against test data provided by Dan Miller of NAWC-China Lake. Accounting for an average throat erosion rate (as measured from test data without boundary-layer control) and coning of the solid propellant surface, the predicted chamber pressure shows reasonably good agreement with the measured chamber pressure (see **Fig. 8**). The differences in the results are due to the absence of detailed flame spreading process and use of a time-averaged nozzle erosion rate in the calculations. The general agreement between the predicted pressure-time trace and the recorded data partially validates the volume filling code for motor design purposes. The volume filling code was also used to deduce the necessary end-burning solid-propellant grain lengths for the proposed test matrix.



**Figure 8.** Comparison of China Lake test data with volume filling code prediction

### 2.3 Propellant Grain Requirements: Penn State University

Two propellant formulations will be tested in order to study the nozzle erosion of graphite and copper-infiltrated tungsten nozzles. The complete test matrix for the motor firings during the Base and Option Programs periods is provided at the end of this report in Appendices A and B, respectively. Since it is known that the combustion products of Propellant S will significantly erode Cu/W nozzles, this combination is excluded from the test matrix. To fully evaluate the effect of pressure on the erosion rate, nominal test pressures of 1000, 3000, 5000, and 7000 psi were selected with two different test durations at each pressure. An end-burning grain with diameter of 4.3-in was selected (4.75-in O.D. casing) and the burn duration is altered by varying the length of the grain. As mentioned in the previous section, the newly developed volume filling code was used to determine the required throat size for the desired chamber pressure level. The throat sizes presented in the test matrix were determined assuming no throat erosion. Since throat erosion is imminent, causing a decrease in chamber pressure, a series of nominal chamber pressures can be analyzed from a single test firing. In total, 32 tests are scheduled during the initial phase of testing with an additional 16 tests scheduled for the Option Program of the MURI project. The initial test phase will consider Propellant S with a graphite nozzle at all chamber pressures and Propellant M with graphite and Cu/W nozzles at 1000 and 3000 psia. The Option Program test phase will evaluate Propellant M with both nozzles at 5000 and 7000 psia.

### 2.4 Test Site Design

In order to run the large solid rocket motor, our existing testing facility needs to be expanded. To experimentally study the erosion rates of nozzle materials, a new high-pressure rocket (10,000 psi) for static tests must be designed. The current **High Pressure Combustion Lab** (HPCL) at PSU cannot accommodate such a large motor. A separate

test site is currently being designed by the university civil engineers with input from us to determine what is required to fire such a large solid propellant motor. The current test site design is a large 18' x 18' (inner dimensions) three sided concrete structure constructed from 2' reinforced concrete walls on top of a reinforced concrete pad. At the open end there will be a large dirt mound to prevent any damage from the ejected nozzle assembly in the event of an over pressurization. Mounting tracks will be embedded in the concrete pad to retain the test stand and the rocket motor. There are also portholes at various spacing along the back wall and sides of the structure. These portholes are for passing data cables from many diagnostic instruments located in the control room to the test site. Portholes along the sidewalls will also allow various cameras to view the motor firing without a concern of damaging them in the event of a failure. During the test firing period, the data acquisition systems and testing personal will be located in a remote control room.

### **3. Recent Progress in Theoretical Model and Numerical Code for Nozzle Erosion (Kuo Group at PSU)**

#### 3.1 Literature Review

Extensive literature review was conducted to investigate the reactions of graphite with various gaseous species found in combustion products of Propellant S (i.e.,  $\text{H}_2\text{O}$ ,  $\text{HCl}$ ,  $\text{CO}_2$ ,  $\text{N}_2$ ,  $\text{CO}$ ,  $\text{H}_2$ ,  $\text{OH}$ ,  $\text{H}$ ,  $\text{O}_2$ , and  $\text{O}$ ). The reaction rate parameters for the reactions of graphite with the oxidizing species mentioned above were determined based upon the technical papers reviewed so far. This information also helped in designing the rocket motor simulator using gaseous reactants.

In the combustion products of Propellant S, only the following oxidizing species are found in significant amount:  $\text{H}_2\text{O}$ ,  $\text{CO}_2$ ,  $\text{CO}$ , and  $\text{OH}$ . For Propellant M, due to the formation of a significant amount of  $\text{Al}_2\text{O}_3$  in the product of this metalized propellant, the mole fractions of  $\text{H}_2\text{O}$  and  $\text{CO}_2$  are significantly lower than those of Propellant S. Also the mole fraction of  $\text{CO}$  (which is not a very effective oxidizer) in products of Propellant M is approximately 2.5 times than that of Propellant S. The concentration of  $\text{OH}$  radical does not vary much between Propellant M and Propellant S.

The graphite oxidation kinetics proposed by Chelliah et al.<sup>10</sup> employs two heterogeneous reaction-rate sets: one for porous graphite and the other for non-porous graphite. Since the time scale associated with the diffusion of oxidizing species in the pores of the nozzle material is much longer than the duration of firing, all the heterogeneous reactions are assumed to be confined to the nozzle surface. Thus, their non-porous (NP) graphite oxidation reactions are more relevant to the current study.

Although some efforts to employ elementary heterogeneous reaction mechanisms are being studied by them, there are still many uncertainties associated with the proposed reaction pathways and rate constants in the literature. In a work by Hurt and Haynes<sup>14</sup>, power law kinetics of graphite oxidation with  $\text{O}_2$  was studied. However, the reaction kinetics data proposed was applied to very low temperature (<1000 K) and low pressure (~0.01 bar). In the paper by Sendt and Haynes<sup>15</sup>, the chemisorption of  $\text{O}_2$  on the armchair surface of graphite was studied and two different reaction pathways were proposed and associated activation energies for formation and desorption of  $\text{CO}$  molecules was

evaluated. But these data were also obtained for relatively lower temperature in comparison with the graphite nozzle surface temperature ( $\sim 1500$  K). Therefore, our current modeling computations have been limited to semi-global heterogeneous reaction mechanisms, similar to that employed by Bradley et al.<sup>13</sup> for modeling oxidation of graphite particles and this is listed in Table 5. The reaction rate constant is assumed to follow the Arrhenius form, i.e.,  $k_j = B_j(T_j)^{n_j} \exp(-E_j/R_u T)$ .

The temperature dependency of surface reaction rates of the reactions listed in Table 5 is shown in **Fig. 9**. It can be seen that the reaction NP2 ( $C_s + O \rightarrow CO$ ) is the dominant reaction for  $T_s > 1400$  K, whereas reaction NP4 ( $C_s + CO_2 \rightarrow 2CO$ ) is the least important for the whole temperature range considered. The surface reaction rates shown in **Fig. 9** are consistent with the results obtained by Bradley et al.<sup>13</sup> As shown earlier, the mole fraction of O radical is insignificant in the combustion products of Propellant S and M. Similarly, the concentration of  $O_2$  is very small thereby making reaction NP5 less important in the overall heterogeneous reaction. Based upon the above observations, the remaining two reactions NP3 and NP1 become more important for the nozzle erosion process. Even though the reaction rate of NP3 is relatively low compared to other reactions, there is very high amount ( $\sim 43\%$ ) of  $H_2O$  in the products of Propellant S; therefore, the oxidation of graphite by water vapor is dominant.

Table 5. Heterogeneous Reaction Rate Constants for Non-Porous Graphite<sup>10</sup>

Step	Reaction	j	$B_j$	$n_j$	$E_j$ (kcal/mol)
NP1	$C_s + OH \rightarrow CO + H$	1	3.61E+02	-0.5	0
NP2	$C_s + O \rightarrow CO$	2	6.65E+02	-0.5	0
NP3	$C_s + H_2O \rightarrow CO + H_2$	3	4.80E+05	0	68.8
NP4	$C_s + CO_2 \rightarrow 2CO$	4	9.00E+03	0	68.1
NP5	$C_s + \frac{1}{2}O_2 \rightarrow CO$	5	2.40E+03	0	30.0
		6	2.13E+01	0	-4.1
		7	5.35E-01	0	15.2
		8	1.81E+07	0	97.0

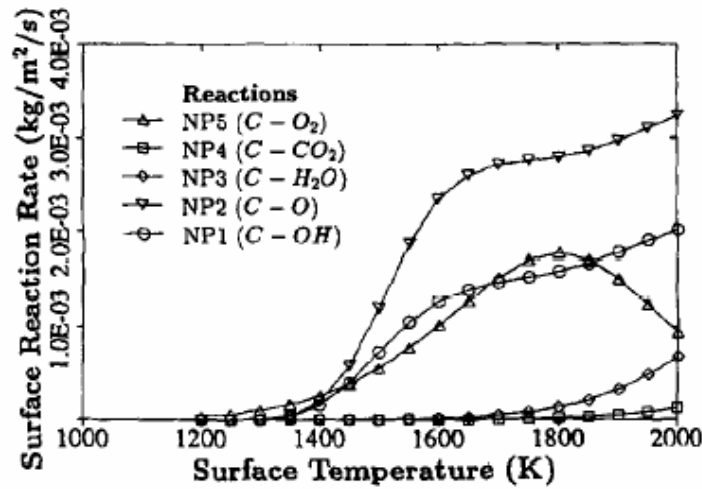


**Figure 9.** Surface reaction rates as a function of the surface temperature in moist air<sup>10</sup>

### 3.2 GRC Code Modifications and Simulation

The Graphite Recession Code (GRC) code developed earlier at PSU by Kuo and Keswani<sup>16</sup> was modified recently to predict the nozzle erosion rate by incorporating the reaction kinetics proposed by Chelliah et. al.<sup>10</sup> The recession rate predictions were obtained using k- $\epsilon$  model for turbulence closure at pressures up to 55 MPa (8,000 psia). Comparison of predicted recession rates using Libby-Blake<sup>17</sup>, Golovina<sup>16, 36, 133</sup> and Chelliah<sup>10</sup> kinetic data is shown in Fig. 10. The net recession rate is harmonic mean of rate of diffusion of species to the graphite nozzle surface and net rate of reaction of species with graphite at the surface. The net recession rate is highest when the reaction kinetics proposed by Chelliah et al.<sup>10</sup> is used with respect to the case for Libby-Blake<sup>17</sup> or Golovina reaction kinetics<sup>16, 36, 133</sup>. In order to investigate this phenomenon, the rate of diffusion and net rate of reaction were also obtained and compared with each other. The rate of diffusion of species from the core region to the graphite surface is very similar for all three cases whereas the net rate of recession due to heterogeneous chemical reaction showed a marked difference. By comparing the diffusion and kinetic rates for these three schemes, it is obvious that the difference in net recession rate for the three cases is due to the difference in heterogeneous chemical reaction rates proposed by these three groups of researchers. Therefore, even though rate of diffusion of oxidizing species from the core region to the nozzle surface is more dominant than the heterogeneous reaction rate in determining the net nozzle surface erosion rate; the overall recession rate of nozzle surface still depends on the reaction kinetics. It is interesting to note that the experimentally measured erosion rate of Propellant S in graphite nozzle at a nominal pressure of 7.9 MPa (1,150 psia) is around 10 mils/s which is close to the predicted erosion rate using reaction kinetics of Chelliah et al.<sup>10</sup>. The reaction kinetics proposed by Chelliah et. al takes into account all the species as shown in Table 5 while the Libby-Blake<sup>17</sup> and Golovina kinetics<sup>16, 36, 133</sup> takes into account the heterogeneous reactions of graphite with H<sub>2</sub>O and CO<sub>2</sub> only. The reason for higher recession rate at higher pressures is mainly due to the rapid increase of heat-transfer rate from the hot gases in the core region to the nozzle throat surface.

The pressure dependency of heat-transfer coefficient at the nozzle throat is shown in **Fig.11**. As pressure increases, the density of the gas mixture increases which cause the Reynolds number at the throat to increase. The Nusselt number strongly depends on the Reynolds number in turbulent flows. Therefore, the heat-transfer coefficient has a strong dependency on pressure. It can be seen that the heat-transfer coefficient at the nozzle throat as predicted by the modified GRC code shows significant increase as the operating pressure is increased. This increase results in higher surface temperature and heterogeneous reaction, which contributes towards increased recession rate of the nozzle throat as pressure increases.



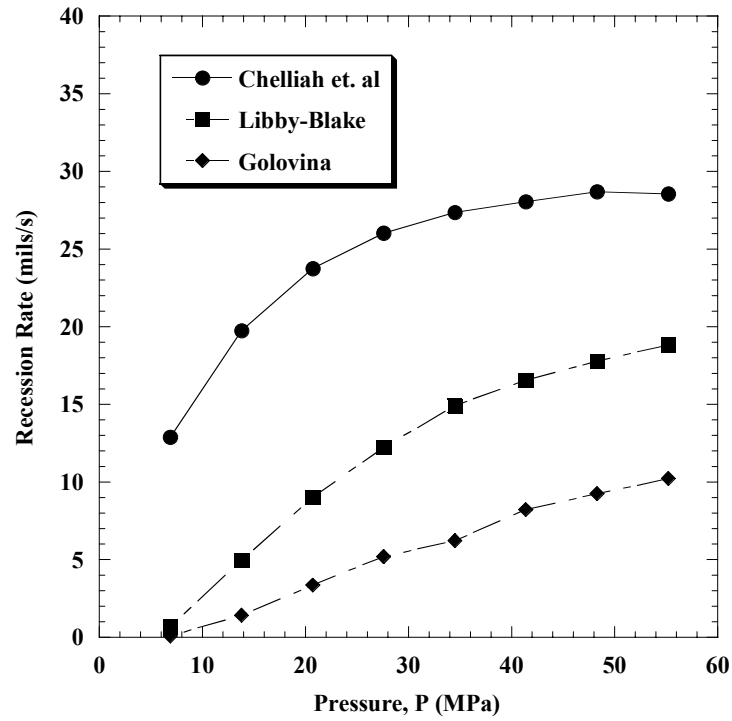


**Figure 10.** Comparison of predicted nozzle throat recession rate using Libby-Blake, Golovina<sup>133</sup>, and Chelliah reaction kinetics for Propellant S with graphite nozzle

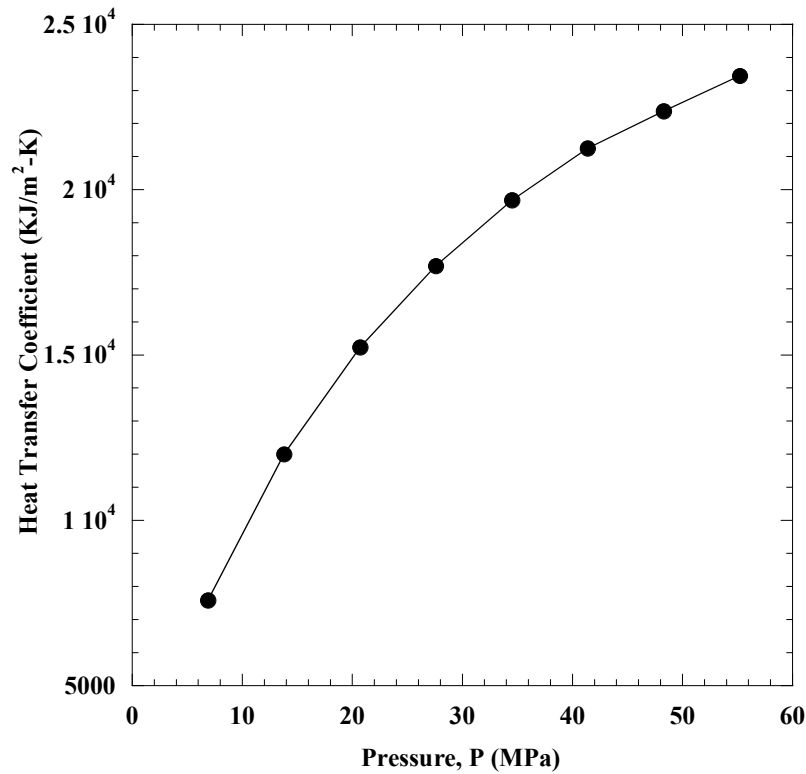


**Figure 11.** Variation of Heat Transfer Coefficient at the Nozzle Throat with Operating Pressure for Propellant S with Graphite Nozzle

#### **4. Heterogeneous Surface Oxidation, Carburization, and Nitration Studies of Bulk Tungsten, Rhenium, and Hafnium (Yetter Group at PSU)**

The bulk oxidation, carburization, and nitration of metals play important roles in the erosion mechanisms of rocket nozzles, and therefore a fundamental understanding of the chemical processes occurring at a metal surface and below its surface are important for developing future nozzles to operate at extreme pressure and temperature conditions. In the present effort, we are conducting flow reactor experiments to gather kinetic data for developing surface reaction mechanisms for use in multidimensional rocket motor calculations. The measurements consist of weight change as well as resistance change as a function of time after a metal sample has been exposed to a controlled high-temperature, variable pressure, chemical atmosphere that could produce oxidation, carburization, or nitration. From modeling studies, the rates of mass loss or gain and the rates of electrical resistance change are correlated to oxidation, carburization, or nitration kinetic rates. Reaction mechanisms are postulated based first upon thermodynamic principles with estimates of the kinetic rates. When available, theoretically derived rates from quantum chemical/molecular dynamics calculations are used. Optimized numerical models developed from fitting the experimental data to the model predictions. Sensitivity analysis is performed to identify the rate controlling reactions and to guide the direction of the present experiments as well as the theoretical efforts of others in the program.

From previous studies on metal oxidation, a general phenomenological understanding of their oxidation kinetics exists. However, only limited kinetic data is available on the overall rates of oxidation, and even less on the rates of individual surface reactions. Furthermore, few studies have examined the conditions relevant to future high-pressure rocket motors. Since rocket nozzle flows will generally be overall fuel rich, little free molecular oxygen will be available for reacting with these metals. Consequently, the major species  $\text{H}_2\text{O}$  and  $\text{CO}_2$  and the minor species  $\text{OH}$ ,  $\text{O}$  and  $\text{NO}$  will play the most important roles in the oxidation mechanism. Because the flow is fuel rich, other processes such as nitration and even carburization may play a role in modifying the behavior of the kinetics at the nozzle surface, particularly since the gaseous combustion products will consist of significant amounts of  $\text{N}_2$  and  $\text{CO}$ .

This research is focusing initially on the oxidation kinetics of tungsten-based materials. We have performed a series of equilibrium calculations to determine the temperature and pressure conditions of the flow reactor experiments necessary to develop reaction mechanisms for use in multidimensional rocket motor calculations and to determine the chemical species necessary to include in the kinetics models. A literature review has been conducted on previous oxidation studies of tungsten. A series of thermo gravimetric analysis experiments have been performed on micron sized tungsten particles in air to determine characteristic reaction times for design of the flow reactor experiments.

Various reactor designs have been developed and multidimensional fluid dynamics calculations have been performed to evaluate the flow fields. A sensitive microbalance for mass measurements has been acquired from the Materials Research Laboratory and various ovens and thermal gravimetric systems have been investigated. A numerical model with sensitivity analysis for studying the kinetics experiments has been developed and applied to iron carburization, which is of interest to the Army with regards to gun barrel erosion. This same code will be applied to the oxidation studies of tungsten.

The equilibrium calculations were performed using the NASA CEA code to determine the speciation of tungsten oxidation products in the boundary layer and on the nozzle surface during high temperature – high-pressure rocket motor combustion. The calculations were performed with a composite propellant (88% AP and 12% HTPB by mass) and a tungsten nozzle. The range of pressures considered was 14.7 to 3000 psi while the temperatures ranged from 1600 to 3400 K. The results are presented in **Figs. 12 and 13**. **Figure 12** reports the equilibrium composition at three pressures (14.7, 1000, and 3000 psi). Under all conditions, except the lowest pressures and highest temperatures, the dominant tungsten containing species was gaseous  $\text{WO}_2\text{Cl}_2$ . In fact, under the complete range of conditions, tungsten generally formed gaseous species, and the erosion mechanism would appear to be a chemical oxidation process and therefore be free of condensed phase species and physical mechanisms of erosion. It is known that rocket motors with tungsten nozzles and non-aluminized AP-based propellants result in a significant amount of nozzle erosion.

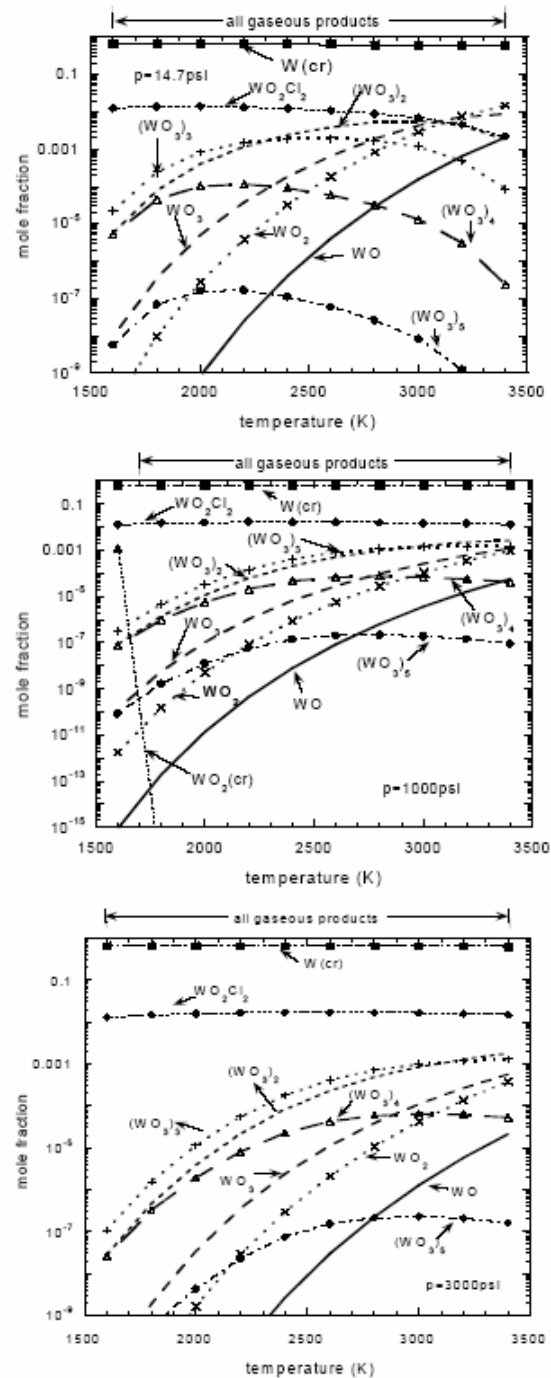


**Figure 12.** Equilibrium speciation in the boundary layer of a tungsten nozzle at pressures of 14.7, 1000, and 3000 psi.

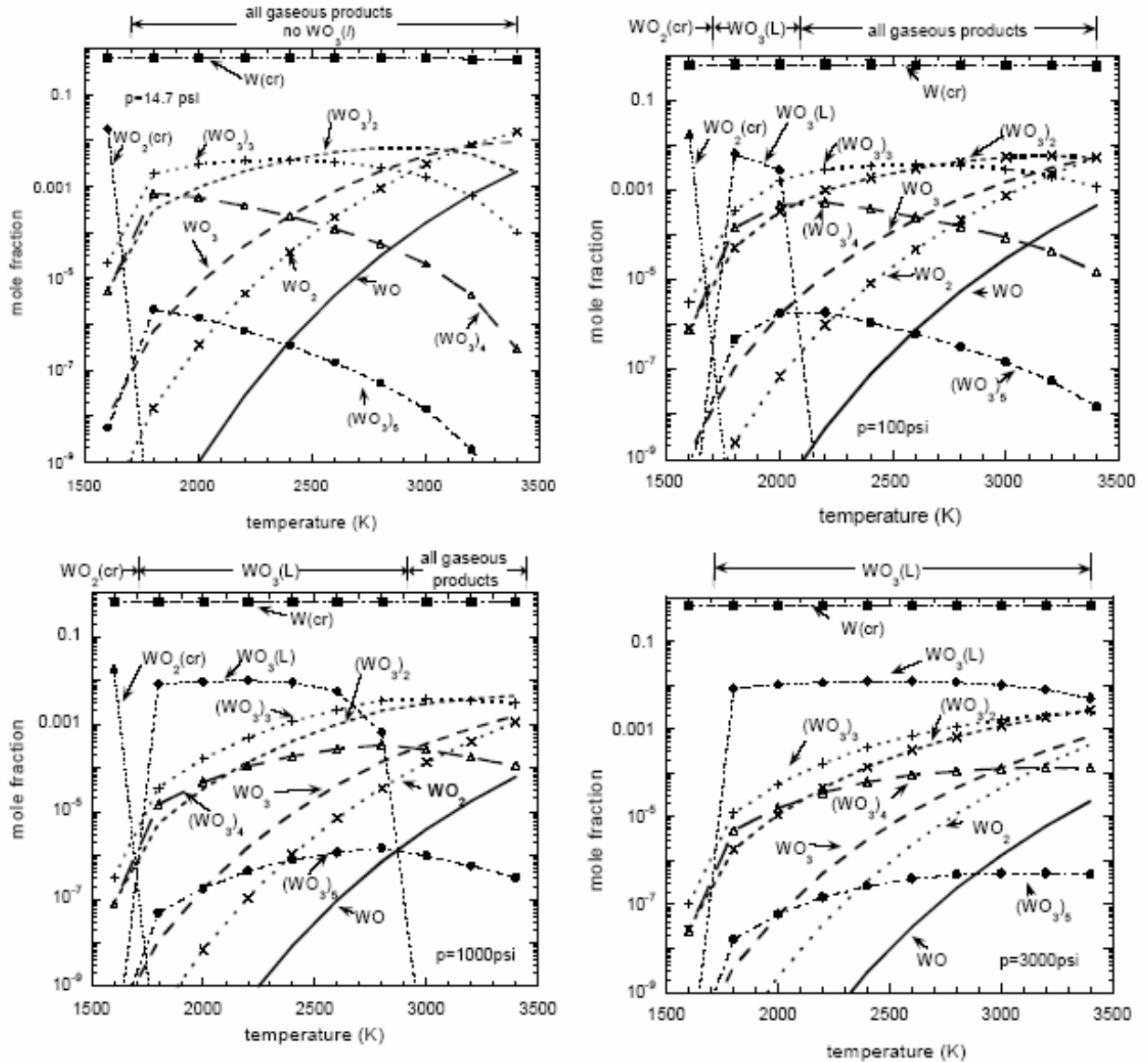


**Figure 13.** Equilibrium speciation in the boundary layer of a tungsten nozzle at pressures of 14.7, 100, 1,000, and 3,000 psi without tungsten oxychloride formation.

Even though this combination of propellant and nozzle is not practical, these equilibrium calculations will be shown below to provide a simple explanation for the experimentally observed trends of excessive erosion.

In another set of calculations, it was assumed that the tungsten oxychlorides were kinetically limited and not formed in the boundary layer. These calculations are also representative of a propellant without chlorine. The results, presented in **Fig. 13** for pressures of 14.7, 100, 1,000, and 3,000 psi, show that the major product species range from gaseous oxides to liquid and solid oxides as a function of pressure and temperature.

Solid  $\text{WO}_2$  forms at the lowest temperatures, i.e., 1700 K and below. At atmospheric pressure and temperatures higher than 1700 K, the products are entirely gaseous, much the same as when chlorine was present in the combustion gases. The dominant species are the trimer and dimer of tungsten trioxide. As the pressure increases (e.g., to 100 psi), liquid  $\text{WO}_3$  is formed over a narrow temperature window (from about 1700 to 2200K). As the pressure is further increased, the temperature window of liquid  $\text{WO}_3$ , as the major product species containing tungsten, increases to temperatures as high as 2900 K at 1000 psi and to considerably higher temperatures at 3000 psi. This liquid could be envisioned to form on the tungsten nozzle surface, and hence physical erosion mechanisms in addition to chemical oxidation would be important. However, the present equilibrium calculations do not restrict the liquid oxide formation to the surface and depending on the oxidation mechanism of tungsten suboxides, the liquid could equally form in the gas-phase within the boundary layer.

It is interesting to note that halogens have a similar effect on the products of tungsten as they do with aluminum and boron combustion where condensed phase oxidation products at combustion temperatures are converted to oxychlorides (or oxyfluorides), which are generally gaseous products.

Another set of equilibrium calculations performed used a composite aluminized propellant (69% AP, 11.5% HTPB and 19.5% Al by mass) and a tungsten nozzle. Results of predominate equilibrium tungsten oxide speciation over the range of temperatures considered are presented in **Fig. 14**, at pressures of 14.7, 1000, and 3000 psia. As with the previous calculations of the non-aluminized AP/HTPB propellant, the dominant tungsten containing species was gaseous  $\text{WO}_2\text{Cl}_2$ ,

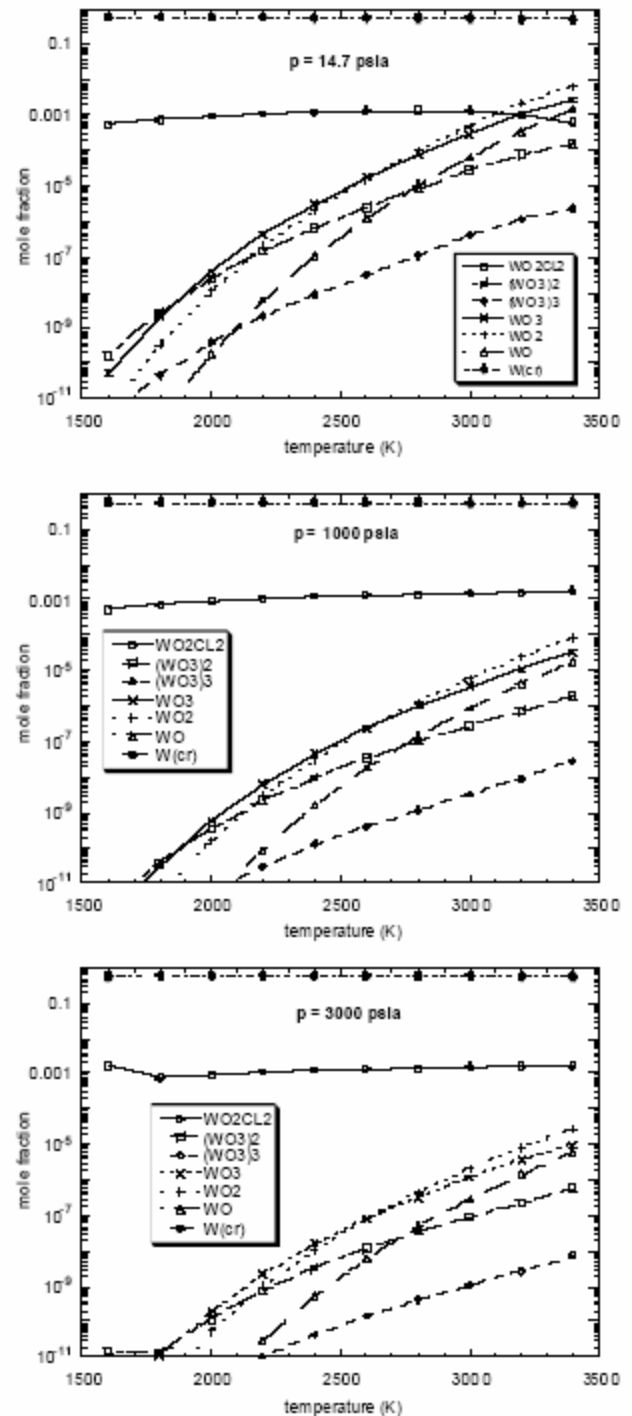


**Figure 14.** Equilibrium speciation in the boundary layer of a tungsten nozzle at pressures of 14.7, 1000, and 3000 psia using 69% AP, 11.5% HTPB, and 19.5% Al by mass propellant

except for the highest temperature and lowest pressure conditions. The addition of aluminum into the propellant reduces the amount of all tungsten oxides in the boundary layer.  $\text{WO}_2\text{Cl}_2$  is reduced by approximately one order of magnitude while the other species were reduced even more.

As in the non-aluminized propellant calculations, a second set of calculations was performed where it was assumed that tungsten oxychlorides were kinetically limited and not formed within the boundary layer. Using the same percent mass quantities of the AP/HTPB/Al propellant as above, results of both the tungsten and aluminum containing dominant equilibrium species are presented in **Fig. 15** and **Fig. 16**, respectively. Both figures illustrate the quantities of each species over the range of temperatures considered at pressures of 14.7, 100, 1000, and 3000 psia.

Unlike earlier calculations of the non-aluminized propellant, no liquid  $\text{WO}_3$  is found over the entire range of temperatures and pressures considered. There is however liquid  $\text{Al}_2\text{O}_3$  formed at temperatures above approximately 2,300 K over the entire range of pressures. Below this temperature the  $\text{Al}_2\text{O}_3$  solidifies. Under most conditions,  $\text{WO}_2$  and  $\text{WO}_3$  are the dominant species, with the exception being the dimer of tungsten trioxide at temperatures below approximately 1,800K. As the temperature is increased, WO surpasses  $(\text{WO}_3)_2$  and nearly reaches the same mole fractions as  $\text{WO}_2$  and  $\text{WO}_3$ .

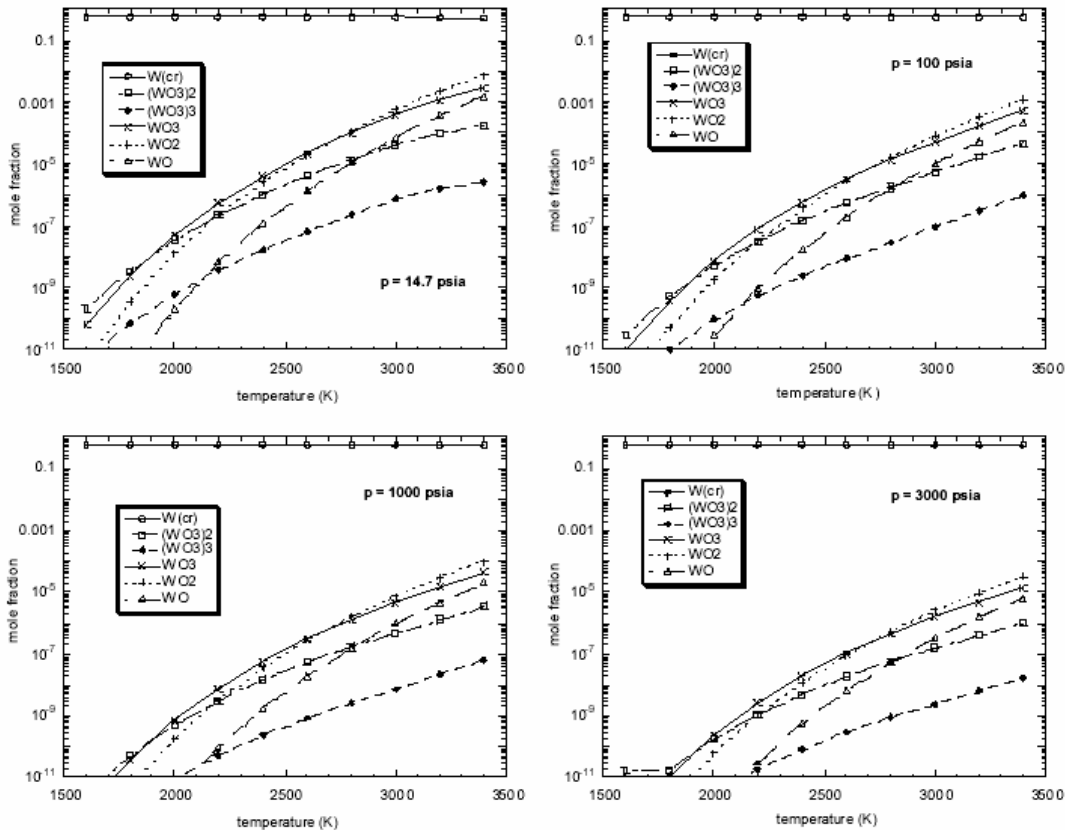


**Figure 15.** Equilibrium mole fractions of tungsten and oxygen containing species in the boundary layer of a tungsten nozzle at pressures of 14.7, 100, 1000, 3000 psia without tungsten oxychloride formation using 69% AP, 11.5% HTPB, and 19.5% Al by mass propellant

**Figure 16** shows that under all conditions either liquid or solid  $\text{Al}_2\text{O}_3$  is the dominant aluminum containing species. This species, which occupies a very large mole fraction of the combustion products, contains a large amount of the oxygen that may otherwise oxidize with the tungsten nozzle, increasing erosion. Since this species does not include chlorine this same effect should occur with non-chlorine containing propellants as well.

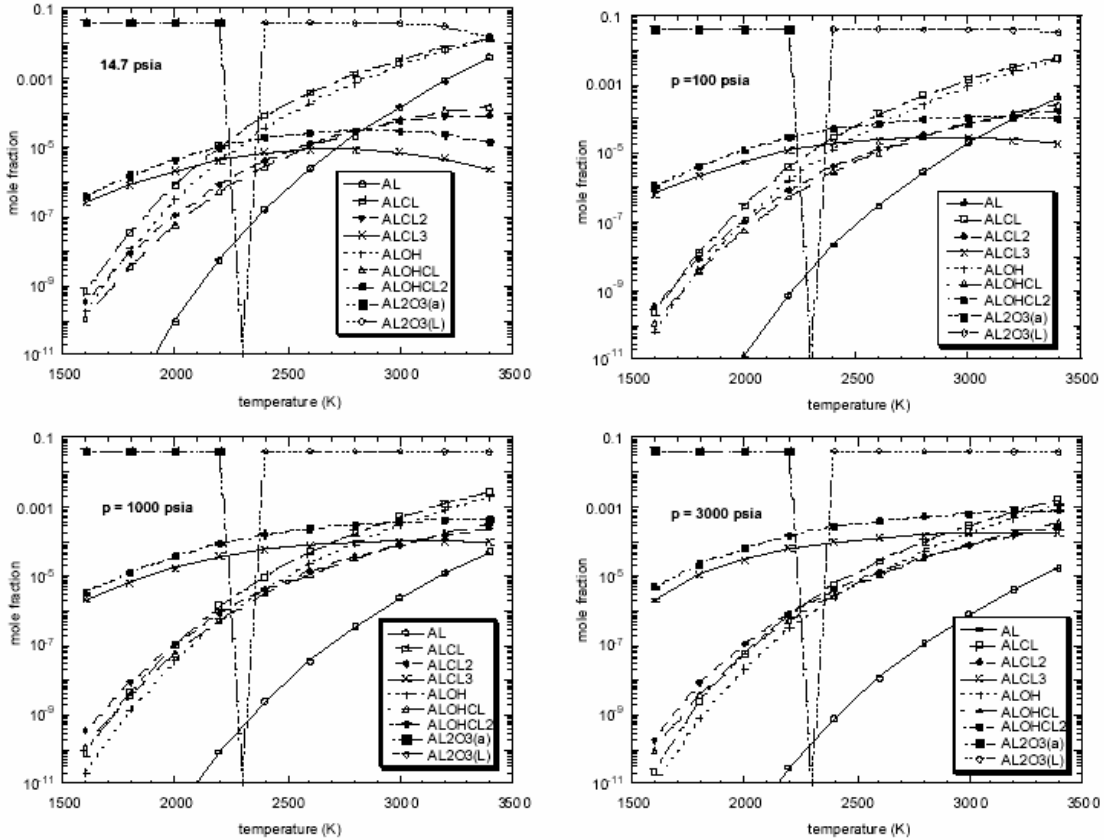


**Figure 16.** Equilibrium aluminum containing speciation in the boundary layer of a tungsten nozzle at pressures of 14.7, 100, 1000, 3000 psia without tungsten oxychloride formation using 69% AP, 11.5% HTPB, and 19.5% Al by mass propellant.

In order to confirm some of the general trends established thus far, a third set of calculations was performed with a second non-aluminized and aluminized propellant containing ammonium dinitramide (ADN), a non-chlorine containing compound. The ADN was considered in these calculations as an illustration of energetic oxidizer without chlorine yet still with a high oxygen percentage. There is no plan for testing and evaluating such a propellant. Using the non-aluminized propellant with ADN in place of AP (88.4% ADN and 11.6% HTPB by mass) and the same temperature and pressure ranges as before, **Fig. 17** was created which presents the tungsten and oxygen containing species at pressures of 14.7, 100, 1000 and 3000 psia.

As expected, the results presented in **Fig. 17** are close to those of the non-aluminized AP/HTPB propellant equilibrium speciation when  $\text{WO}_2\text{Cl}_2$  is assumed not to occur. As pressures increases (e.g., to 100 psia), liquid  $\text{WO}_3$  is formed over a narrow

temperature region (from approximately 1700 to 2200K). As pressure is increased to 3000 psia, this window of liquid  $\text{WO}_3$  widens until it covers all the temperatures considered above about 1,700 K. Since the tungsten nozzle must react to form this liquid it may be envisioned to form on the nozzle surface, and therefore the physical erosion mechanism in addition to the chemical oxidation is important. However, the equilibrium calculations do not restrict the formation of liquid  $\text{WO}_3$  to the surface and depending on the oxidation mechanisms of the tungsten suboxides, the liquid may also be formed in the gas-phase boundary layer.

Equilibrium calculations of the aluminized ADN propellant (69% ADN, 11.5% HTPB and 19.5% Al by mass) were also performed. The results of these calculations are similar to the results of the aluminized AP propellant, excluding the chlorine containing species. The same tungsten oxides dominate and exist in the same relative proportions, and the dominant aluminum containing species is  $\text{Al}_2\text{O}_3$  throughout. As shown in the prior calculations, liquid-phase tungsten oxide was not found in the equilibrium products.

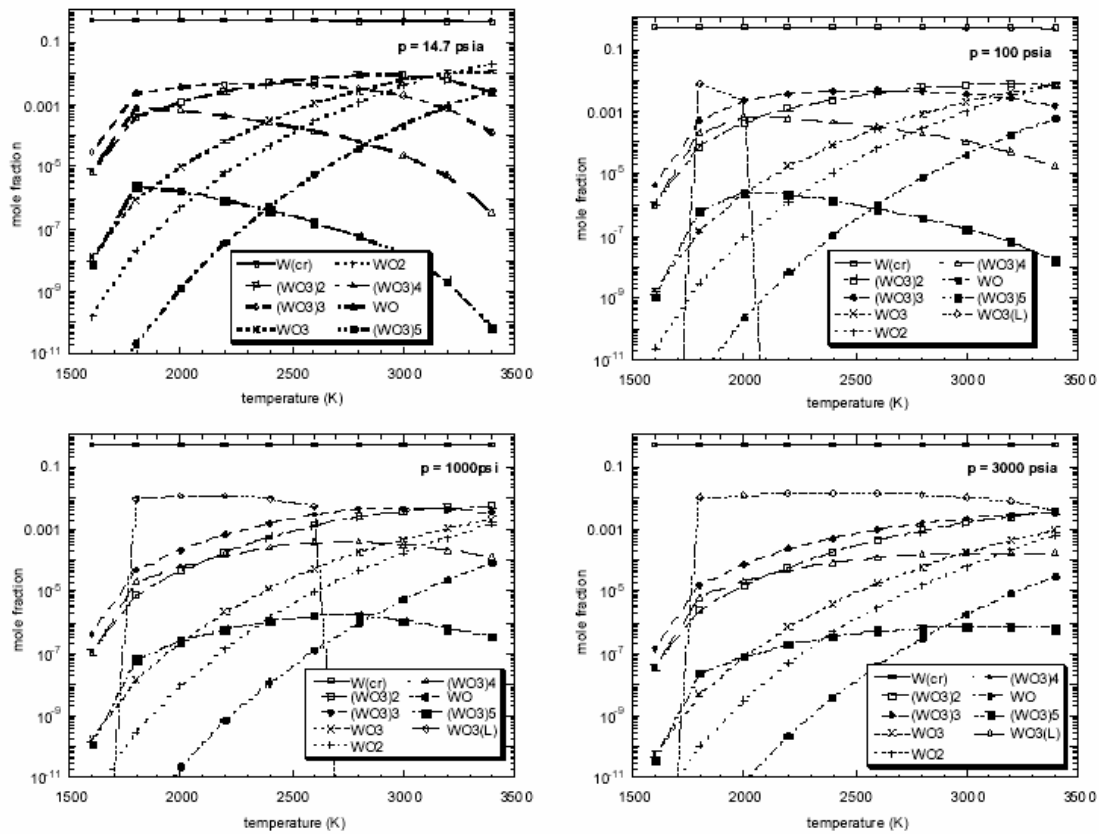


**Figure 17.** Equilibrium mole fractions of tungsten and oxygen containing species in the boundary layer of a tungsten nozzle at pressures of 14.7, 100, 1000, 3000 psia using 88.4% ADN and 11.6% HTPB by mass propellant.

## 5. Modeling and Simulation of Nozzle Material Erosion (Yang Group at PSU)

During this report period, emphasis was placed on the establishment of a general formulation for treating nozzle material erosion in solid-propellant reacting flow



environments. The purpose is to construct a unified analysis taking into account propellant chemistry, fluid dynamics, gas-phase homogeneous reaction kinetics, heterogeneous surface reaction kinetics, and nozzle material properties.

Calculations were first carried out using the CEC (Chemical Equilibrium Calculation) code to characterize the species concentrations of propellant combustion products at different chamber pressures. The flame temperatures and product species concentrations of AP/HTPB (non-metallized) and AP/HTPB/Al (metallized) propellants were obtained as functions of pressure and propellant compositions. A comprehensive theoretical formulation was developed and a detailed literature survey was carried out to establish the surface chemistry for the pyrolysis and thermal degradation of carbon-carbon or graphite materials. In addition, the development of an LES numerical code and its parallelization is progressing well.

The comprehensive theoretical model is being developed for

- Gas-phase processes;
- Condensed-phase processes;
- Boundary conditions at the interface between the gas and condensed phases;
- Turbulence closure;
- Heterogeneous chemical kinetics at the gas-solid interface;
- Homogeneous chemical kinetics in the gas phase.

### 5.1 Heterogeneous chemical kinetics at the gas-solid interface

In the combustion of solid propellants of concern, the following species are found in significant amounts:  $\text{H}_2\text{O}$ ,  $\text{HCl}$ ,  $\text{CO}_2$ ,  $\text{N}_2$ ,  $\text{CO}$ ,  $\text{H}_2$ ,  $\text{Cl}$ ,  $\text{OH}$ ,  $\text{H}$ , and in addition to these,  $\text{Al}_2\text{O}_3$  in the case of metallized propellant. It is vital to know the relative importance of the heterogeneous reactions of the aforementioned species with the graphite materials. As a preliminary analysis, a chemical equilibrium calculation (CEC calculations) is performed between  $\text{C}_s$  and each of the reacting species obtained from the propellant combustion. The following table shows the extent of reaction of the individual chemical species, present in the propellant combustion products, with graphite ( $\text{C}_s$ ) at equilibrium. To start with 1 mole of each,  $\text{C}_s$  and the other reactants are considered at 3,500 K and 200 atm (2,940 psia). The results show the calculations using the CEC code at constant temperature and pressure conditions (i.e., the TP case). The number of moles of  $\text{C}_s$  at equilibrium is calculated to get an idea of the extent of the reaction that has taken place, which in turn gives us an estimate of consumption of  $\text{C}_s$ . The Gibbs free energies,  $G$  of the reactions are also provided. The more negative the value of  $\Delta G$ , the more is the  $K_p$  for the reaction. This implies more forward reaction due to the shift of the equilibrium in the forward direction. Apart from the estimate of the extent of the reactions, to start with, it is important to consider the relative amount of these species concentrations present at the nozzle throat, so that we can prioritize and select those reactions which are sufficiently important to be considered in the heterogeneous reactions kinetic model.

**Table 6** Equilibrium mole fractions of various chemical species at graphite surface, Gibbs free energy change, and heat of reaction

Species reacting with C <sub>s</sub>	Mole fraction of C <sub>s</sub> at equilibrium	Mole fraction of the Spices at equilibrium	Moles of C <sub>s</sub> at equilibrium	$\Delta G$ for reaction cal /g	$\Delta H$ for reaction cal /g
H <sub>2</sub> O	0	0.00214	0	-10603.7	975.58
CO	0.49986	0.49996	0.99	-5617.01	458.12
CO <sub>2</sub>	0	0.00017	0	-7010.26	14.547
HCl	0.47412	0.42891	0.9679	-4370.82	630.22
H <sub>2</sub>	0.35906	0.48836	0.5634	-10141.6	4047.75
H	0.60837	0.01420	0.7816	-6555.61	2867.90
Cl	0.54554	0.31639	0.9308	-2780.37	1077.15
OH	0	0.00006	0	-8933.86	523.87
N <sub>2</sub>	0.49562	0.49989	0.9845	-4822.32	1131.29
O <sub>2</sub>	0	0.10596	0	-6898.30	-748.63
Al <sub>2</sub> O <sub>3</sub> (l)	0	0.25609	0	-5708.11	1101.74

The column shows the moles of C<sub>s</sub> at equilibrium (for each mole of C<sub>s</sub> in the beginning). Based on the preliminary CEC calculations, the reactions of graphite with the species H<sub>2</sub>O, CO<sub>2</sub>, OH, O<sub>2</sub>, and Al<sub>2</sub>O<sub>3</sub>(l) seem important. The reactions with species H<sub>2</sub> and H also appear important. The reactions with species CO, HCl, Cl, and N<sub>2</sub> do not appear significant based on the CEC calculations. But to rule out any reactions with certain chemical species further detailed kinetic studies are needed.

## 5.2 Chemical kinetics model for graphite oxidation

For the graphite oxidation kinetics, two heterogeneous reaction-rate sets: one for porous graphite and the other for non-porous graphite are used. Since the time scale associated with the diffusion of oxidizing species in the pores of the nozzle material is much longer than the duration of firing, all the heterogeneous reactions are assumed to be confined to the nozzle surface. Thus, the non-porous graphite oxidation is more relevant to the current study. But results will also be obtained for porous graphite oxidation for completeness and comparison. The kinetic parameters given in the table below depend on the specific temperature range. Care must be exercised when extrapolating to a different temperature condition.

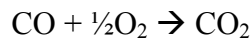
**Table 7** Chemical kinetics at the gas-solid interface for non-porous graphite

$$k_j = B_j T^{n_j} \exp\left(\frac{-E_j}{R_u T}\right), \text{ units of } P \text{ in atm. and } T \text{ in K}$$

Reaction	$B_j$	$n_j$	$E_j$ (kJ/mol)	$\dot{s}_j$ (Kg/m <sup>2</sup> s)	Ref.
$C_{(s)} + OH \rightarrow CO + H$	361	-0.5	0.0	$kP_{OH}$	Bradley et al. <sup>13</sup>
$C_{(s)} + O \rightarrow CO$	665	-0.5	0.0	$kP_O$	Bradley et al. <sup>13</sup>
$C_{(s)} + H_2O \rightarrow CO + H_2$	480000	0.0	68800	$kP_{H_2O}^{0.5}$	Bradley et al. <sup>13</sup>
	2470	0.0	41900	$kP_{H_2O}$	Libby and Blake <sup>17</sup>
$C_{(s)} + CO_2 \rightarrow 2CO$	9000	0.0	68100	$kP_{CO_2}^{0.5}$	Bradley et al. <sup>13</sup>
	2470	0.0	41900	$kP_{CO_2}$	Libby and Blake <sup>17</sup>
$C_{(s)} + \frac{1}{2}O_2 \rightarrow CO$	(1) 2400 (2) 21.3 (3) 0.535 (4) 18100000	0.0 0.0 0.0 0.0	30000 -4100 15200 97000	$\left\{ \frac{k_1 P_{O_2} Y}{1 + k_2 P_{O_2}} + k_3 P_{O_2} (1 - Y) \right\}$  where, $Y = \left[ 1 + \frac{k_4}{k_3 P_{O_2}} \right]^{-1}$	Bradley et al. <sup>13</sup>
	87100	0.0	35770	$kP_{O_2}$	Libby <sup>18</sup> (1000-2000 K)
$C_{(s)} + 4H \rightarrow CH_4$	192	-0.5	0.0	$kP_H$	Bradley et al. <sup>13</sup>

### 5.3 Chemical kinetics in the gas phase

The major gas-phase species are CO<sub>2</sub>, H<sub>2</sub>O, HCl, CO and H<sub>2</sub>. The major reaction taking place in the gas phase is the CO oxidation which implies that the gas-phase and surface reactions are strongly coupled. Makino et al.,<sup>20,21</sup> Matalon<sup>22</sup>, and Reinelt et al.<sup>23</sup> have considered a one-step overall irreversible gas-phase reaction:



In the gas phase, Chelliah et al.<sup>10</sup> used a CO/H<sub>2</sub>/O<sub>2</sub> reaction mechanism by Yetter et al.<sup>24</sup> It involves 12 species and 28 reactions. Inclusion of a complete reaction mechanism, however, is not computationally practical for LES-based nozzle-flow simulations. Thus,

studies are underway to determine the important and critical gas-phase reactions to be included in the chemical kinetics model within the context of LES.

**Table 8** Chemical kinetics at the gas-solid interface for porous graphite

$$\dot{s}_j = W_j c_j B_j T^{n_j} \exp\left(\frac{-E_j}{R_u T}\right) \text{ Units of } \dot{s}_i \text{ in (Kg/m}^2\text{s)}, B_j T^{n_j} \text{ in (m/s) and } T \text{ is in K}$$

Reaction	$B_j$	$n_j$	$E_j$ (cal/mol)	Ref.
$\text{C}_{(s)} + \text{OH} \rightarrow \text{CO} + \text{H}$	1.65	0.5	0.0	Bradley et al. <sup>13</sup>
$\text{C}_{(s)} + \text{O} \rightarrow \text{CO}$	3.41	0.5	0.0	Bradley et al. <sup>13</sup>
$\text{C}_{(s)} + \text{H}_2\text{O} \rightarrow \text{CO} + \text{H}_2$	$6 \times 10^7$	0.0	64300	Assumed by Chelliah et al. <sup>10,19</sup>
	$2 \times 10^8$	0.0	64750	Makino <sup>20</sup>
$\text{C}_{(s)} + \text{CO}_2 \rightarrow 2\text{CO}$	$6 \times 10^7$	0.0	64300	Makino et. al <sup>21</sup>
$2\text{C}_{(s)} + \text{O}_{2(g)} \rightarrow 2\text{CO}$	2200000	0.0	43000	Makino et. al <sup>21</sup>
$\text{C}_{(s)} + 4\text{H}_{(g)} \rightarrow \text{CH}_4$	-	-	-	-

#### 5. 4 Turbulence closure using LES (Large-eddy simulations)

Turbulence closure in the modeling of the gas-phase process is obtained based on a large-eddy simulation technique in which larger, energy-carrying structures are computed explicitly and the effect of smaller, unresolved scales of motion is modeled either empirically or analytically.<sup>25, 26</sup> A spatial filter  $G$  is used to decompose the flow variables into large (resolved) and subgrid (unresolved) scales:

$$\begin{aligned} \mathfrak{T}(\mathbf{x}, t) &= \mathfrak{T}^r(\mathbf{x}, t) + \mathfrak{T}^s(\mathbf{x}, t) \\ \text{with } \mathfrak{T}^r(\mathbf{x}, t) &= \int_D G(\mathbf{x} - \mathbf{x}', \Delta) \mathfrak{T}(\mathbf{x}', t) d^3x' \end{aligned}$$

where  $D$  is the entire domain,  $\Delta$  the filter length scale which determines the size and structure of the unresolved scales, and  $\mathfrak{T}$  any flow property viz.  $\rho$ ,  $p$ ,  $u_i$ ,  $T$  or  $Y_i$ . The superscripts  $r$  and  $s$  represent the resolved- and subgrid-scales of flow properties, respectively. It is worth noting that for LES-based, finite-volume algorithms, the governing equations are not explicitly filtered. The filtering is based on an open-hat filter (Piomelli (1986)) and is implicit in the formulation. In the present work, the subgrid-

scale (sgs-) quantities are modeled using either an improved Smagorinsky's model or a dynamic Smagorinsky model (DSM).

### 5.5 Numerical treatment

The theoretical formulation is solved numerically by means of a density-based, finite-volume methodology. Spatial discretization is achieved using a fourth-order central difference schemes along with sixth-order artificial dissipation in generalized coordinates. A multi-block domain-decomposition method is implemented to facilitate parallel processing in a disturbed computing environment using the Message Passing Interface (MPI) library. All the calculations are being conducted on an in-house Beowulf system consisting of 510 Pentium CPUs.

## **6. Measurement of Gas-Phase and Heterogeneous Reaction Rates of Carbon and Tungsten Systems at High-Pressure and High-Temperature Conditions (Brezinsky Group at UIC)**

This year, design and complete assembly of the major equipment necessary for this project were done. Furthermore, a method to study the performance of the particle injector and evaluate the desired chemical kinetics was devised.

### 6.1 Shock Tube

The new test section of the shock tube has been bored, honed, electro-polished, and machined. A few steps still remain before the new test section can be used. The pressure transducer ports still need to be machined, but the difficult buttress thread machining has been completed. Additionally, the particle injector must be mounted to the shock tube's frame.

### 6.2 Particle Injector

All parts of the particle injector are now complete. We added copper tubing and an isolation valve to use when flushing air out of the injector and replacing it with the test gas that fills the shock tube. We also built a replica of the test section out of plexiglass (**Fig. 18**). This device allowed us to view the behavior of the particles when they are injected into the tube. We used a high-speed camera to film the particles once they were injected into the plexiglass tube. The information we gathered from analyzing the resulting images helped us select the optimal air pressure to use when injecting particles into the shock tube. We want to maximize the time that the particles are suspended and minimize the length of the particle cloud.

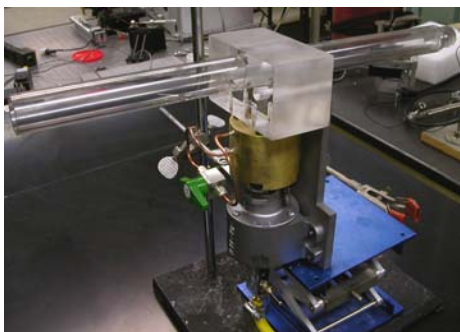
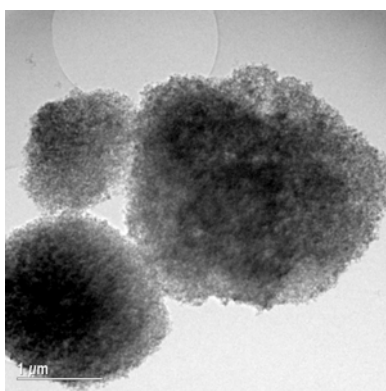


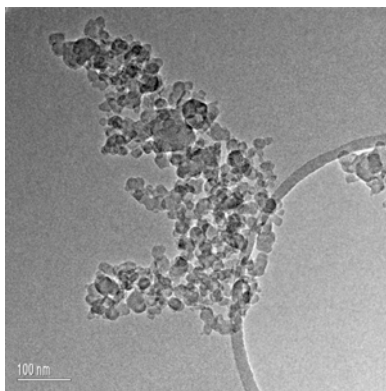
**Figure 18.** Plexiglass tube attached to particle injector

We intend to use the carbon black from Cabot Corporation in experiments to determine the kinetic parameters of carbon oxidation by water and carbon dioxide. We selected this material over the baseline graphite material for the MURI project because Metallurgy G-90 is not available in powder form. The carbon black powder from Cabot (Monarch<sup>®</sup> 800; Density: 1.9 g/cm<sup>3</sup>, Specific Area: 210 m<sup>2</sup>/g, Crystalline State: Amorphous, and C/H ratio: 99) has the same density as the G-90 material (1.9 g/mL) and has a well-defined diameter range (20 to 100 nm). The particles' diameter range is of concern because it determines whether the reactions will be diffusion or reaction limited.

We used UIC's TEM to further characterize the carbon black powders. Two TEM images from this analysis are in **Fig. 19**. These images show aggregates of 20 nm diameter particles. We will obtain more TEM images to clarify the structure of the carbon and whether such agglomerations are common or if the sample preparation method that we used caused the carbon to agglomerate. Banin and coworkers<sup>27</sup> indicate that at pressures above 1 bar, carbon particles with a diameter below 6 μm undergo reaction-limited combustion. Therefore, we expect to be in the reaction-controlled regime because the particles have a diameter below 6 μm and because we will conduct experiments from 550 to 700 bar.



A



B

**Figure 19.** Transmission electron microscope images of carbon black powder from Cabot Corporation. (A: 1 μm, B: 100 nm)

### 6.3 Injector Problems

Evenly distributing the carbon/tungsten particles throughout the shock tube cross section was the original hurdle we thought we had to overcome. However, when using the high speed camera, we noticed a slightly different problem; a large percentage of the particles were never going into suspension. Instead, as the particle jet formed and hit the opposite wall of the tube, some particles trickled down the side until they came to rest, never going into suspension. The carbon/tungsten not going into suspension could pose a problem. Any particles we inject into the shock tube have to be available to react with the test gas in order to properly identify the reaction properties. Carbon/tungsten in the boundary layer is an issue with other injectors, but Bazyn et al.<sup>28</sup> optically analyze only the burn time of the particles which make their way to the reaction zone, so some particles can remain in the boundary layer without negative consequences. Fedorov<sup>29</sup> review outlines papers related to coal dust lifting resulting from the Saffman force, a force perpendicular to and resulting from a velocity gradient. As a shockwave travels across a dust layer, the dust is entrained in the flow above. The Saffman force increases with decreasing boundary-layer thickness and decreasing particle size. With the UIC HPST boundary layer being minimal and the particles nominal size being less than a micron, we are confident that all the carbon/tungsten injected into the shock tube, whether originally in suspension or not, will be available for reaction after the incident shock wave passes over the particles.

#### 6.4 Shock Tube Heating

Water will be present in the heterogeneous reactions as both a reactant and product. It will condense if the temperature of the shock tube is not appropriately high. To avoid condensation, we have added heating equipment to the shock tube that is capable of maintaining the tube at 150°C. The heat tape (Clayborn Precision Heat Tape, Truckee, CA) adheres to the shock tube to eliminate heat loss from poor tape-tube contact. A layer of insulation (Auburn Manufacturing Inc., Mechanic Falls, ME) further limits heat loss. The tapes are controlled by three four-zone temperature controllers (Omega Engineering, Stamford, CT). **Figure 20** contains pictures of the insulated, heated shock tube.

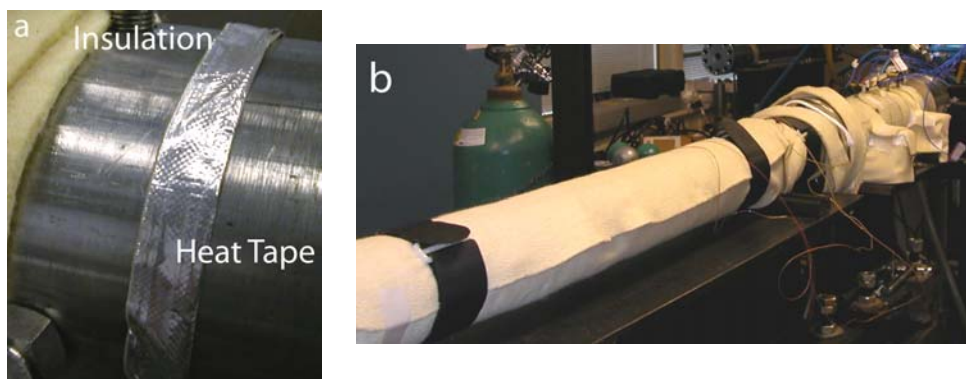


**Figure 20.** a) Heat tape on shock tube before covering with insulation. b) Insulated shock tube.

## 6.5 Kinetics Study

### 6.5.1 Background

One of our objectives is to assess the validity of the kinetic parameters for two key heterogeneous oxidation reactions (R1 and R2) that are used in the Kuo and Keswani model for rocket nozzle erosion<sup>16,30</sup>, the basis for the model currently under development.



Despite numerous studies of Reactions 1 and 2, disagreement exists about the reaction mechanism and values of kinetic parameters<sup>31</sup>. Here, we briefly review several investigations into the kinetics and mechanisms of carbon oxidation by H<sub>2</sub>O and CO<sub>2</sub>.

In some of these studies<sup>32-39</sup>, reaction rates were determined by measuring the mass change of carbon in the form of rods, spheres, or coal char. In the present study, however, collecting and accurately measuring the mass of post-shock particles is not feasible. Therefore, we will extract kinetic parameters from the final and initial concentrations of gaseous species.

Several previous investigators have taken this approach. Van Heek et al.<sup>40</sup> measured the reaction rates of the gasification of coal samples in a sweep gas reactor from 400 – 1100°C. They analyzed the gaseous reaction products (H<sub>2</sub>, CO, CO<sub>2</sub>, and CH<sub>4</sub>) via GC-MS and calculated the degree of carbon conversion. They used a non-isothermal technique to develop the kinetics.

Overholser and Blakely<sup>41</sup> determined the overall reaction rate for the reaction of water and carbon dioxide with graphite by measuring both the concentrations of the gaseous species in the quartz tube reactor effluent and the weight change of spherical graphite samples. The reaction temperature ranged from 825 to 1025°C in their work. Reaction rates based on gaseous product analysis were derived from the concentration of either H<sub>2</sub> or CO, although the calculations were not described. Rates based on H<sub>2</sub> concentrations were less than those calculated from CO concentrations. Reaction rates determined from the weight change of the specimen were consistently lower than the CO- and H<sub>2</sub>-based rates. The authors stated that these results must be due to an unidentified systematic error.

Story and Fruehan<sup>42</sup> conducted a recent study to provide data at higher temperatures (1300-1500°C) for CO<sub>2</sub> and H<sub>2</sub>O oxidation of carbonaceous materials. These authors calculated the limited mixed rate constant based on the flux of CO<sub>2</sub> and H<sub>2</sub>O.

### 6.5.2 Kinetic Strategy

We have developed a strategy to confirm the two rate constants of interest in the Kuo and Keswani model,  $k_1$  and  $k_2$ , based on the gas phase composition in the shock tube before and after a shock wave is fired. These rate constants will be for the global reactions because we will be unable to measure the rates of adsorption and desorption reactions. First, to determine  $k_1$ , we will conduct experiments in the shock tube with carbon particles and use CO<sub>2</sub> as the sole reactant gas. We will then use the integration



method<sup>43</sup> to calculate a rate constant for Reaction 1. In this method, the rate of a reaction with the stoichiometry of Reactions 1 and 2 and unequal initial concentrations of reactants can be described by Eq. (1).

$$\frac{dx}{dt} = k_A (A_0 - x)(B_0 - x) \quad (1)$$

In this equation,  $A_0$  is the initial concentration of reactant A,  $B_0$  is the initial concentration of reactant B,  $x$  is the amount of A that has reacted per unit volume, and  $t$  is the reaction time. Integrating this equation yields Eq. (2).

$$k_A = \frac{1}{t(A_0 - B_0)} \ln \left[ \frac{B_0(A_0 - x)}{A_0(B_0 - x)} \right] \quad (2)$$

When this equation is applied to calculating  $k_1$ , the identity of reactant A is carbon and that of reactant B is  $\text{CO}_2$ .  $x$  is the conversion of carbon per unit volume. A carbon balance will provide this parameter because each mole of CO that forms consumes one mole of carbon.

We will also apply this method to calculate  $k_2$ . In experiments with  $\text{H}_2\text{O}$  as the sole reactant gas, the water-gas shift reaction (R3) will occur.



This reaction, however, does not produce or consume carbon on net, so performing a carbon balance will reveal the extent of carbon conversion from Reaction 2. Eq.(2) can then be applied (with  $\text{H}_2\text{O}$  as the identity of reactant B) to calculate the rate of Reaction 2.

## 7. Computational Approach towards Prediction of Kinetic Rate Constants (Lin, Musaev, and Irle Group at Emory)

Computationally, the chemistry involved in rocket nozzle erosion is complex and technically difficult to unravel because of the size of the system required for realistic simulations and many unknown factors, namely local pressure and temperature fluctuations, as well as unknown surface composition of nozzle throat materials. Our first year objectives were twofold: (i) to investigate reactions  $\text{H}_2\text{O}$ , CO, NO and H with graphite with and without defects using exploratory QM/MD trajectory calculations under high temperatures/pressures, to further investigate transition states using DFT, ONIOM, and VASP, and to calculate the rate constants for these reactions; (ii) to study the reaction mechanisms of  $\text{W}/\text{W}^+$  with  $\text{H}_2\text{O}$ , CO,  $\text{CO}_2$ , NO and  $\text{NO}_2$  at their ground and several lower-lying excited electronic states using the most accurate electronic structure methods.<sup>44</sup>

Since this entire complex of high-temperature/high-pressure nozzle erosion is uncharted territory, a new theoretical methodology for the *a priori* prediction of reaction rate constants had to be developed and extensively tested by us.<sup>45</sup> It is comprised of a

three-stage strategy: 1). isokinetic DFTB-D QM/MD simulations are carried out at high temperatures to probe bias-free reaction pathways for exhaust molecules and their dissociation products on dimers of surface models, 2). identification and characterization of stationary points along these pathways using the ONIOM(B3LYP/6-31+G(d):DFTB-D) level of theory with parts of the surface models and the exhaust molecules and/or fragments in the ONIOM high level model system, and 3). calculation of reaction rate constants based on the characterized TS's. In addition, careful examination of electronic states involved in molecule/surface reactions using highly correlated CCSD(T) and more sophisticated levels of theory is prerequisite for a detailed atomistic understanding of surface erosion processes, especially when transition metal atoms are involved.<sup>46</sup>

In the first year of our project participation, we have successfully implemented approaches to study elementary reactions of water, OH and H radicals, NO, CO and CO<sub>2</sub> species on pure graphite and tungsten surfaces, of which water and OH/H reactions were reported first,<sup>(45-46)</sup> and papers on NO/CO/CO<sub>2</sub> studies following the spirit of these ground-breaking works are nearly ready for submission. The motivation for attacking the OH problem first is the fact that it is the key radical chain carrier in propellant combustion and thus prototype for all nozzle erosion elementary reaction processes.

### 7.1 DFT, ONIOM, and DFTB-D Studies of Water Clusters on Graphite

In the first stage of our studies, we have successfully established the reliability of our proposed quantum chemical methods of choice for exploratory research of reaction systems involving combustion product H<sub>2</sub>O on graphite surfaces, using single level DFT, self-consistent charge DFTB (in the following simply denoted as DFTB), and two-level ONIOM calculations. In order to describe the van-der-Waals attractive forces between graphite layers, a modified version of DFTB had to be utilized, which employs an empirical Heitler-London type dispersion term<sup>47</sup> for the description of these forces. The structures studied at this stage are exclusively equilibrium geometries to ensure that the chemistry described with future QM/MD simulations is reproduced qualitatively correct. Three different model systems have been employed: a) pure water clusters, b) pure graphene sheet clusters, and c) water clusters on graphene layers. In the following, we will discuss the results of our studies on these three model systems in detail.

#### *7.1.1 Pure Water Clusters*

We have computed energetics and geometries of water clusters (H<sub>2</sub>O)<sub>n</sub> with  $n=1-5$ . Vibrational frequencies have been computed as well in order to confirm that the structures correspond to local minima on the potential energy surfaces (PES). Geometries of these water clusters were calculated by B3LYP/6-311+G(3df,2p), B3LYP/6-31+G(d), and DFTB-D. It is noticeable that B3LYP values for O-H bonds not participating in hydrogen bonds show little distinction between different sizes of basis sets, while H-O bonds involved in hydrogen bonds differ by up to half of a tenth of an Ångstrom. This does not come as a surprise, as the presence of polarization functions, particularly on H atoms, are known to be important for the accurate description of hydrogen bonds. DFTB-D performs equally well as B3LYP/6-31+G(d), even though deviations are less systematic. Yet, the observed geometrical differences are small enough to endorse the use of the computationally less expensive B3LYP/6-31+G(d) and DFTB-D levels of theory,

particularly in the light that the chemistry of interest takes place at extremely high temperatures and pressures. The same can be said about the performance of DFTB and B3LYP/6-31+G(d) with respect to vibrational frequencies, with largest deviations from B3LYP/6-311+G(3df,2p) values being less than 100 wavenumbers.

The interaction energies between individual water molecules in the water clusters  $(\text{H}_2\text{O})_n$  with  $n=1-5$  are tabulated in Table 9. The total interaction energies ( $\Delta E_1$ ) as well as incremental interaction energies ( $\Delta E_2$ ) at all three levels of theory follow the same trends, namely increasing total interaction energy with number of water molecules, and a peak of incremental interaction energies for  $n=4$ . The smaller basis set in the B3LYP

**Table 9.** The calculated binding energies (in kcal/mol) of the water clusters. Here,  $\Delta E_1$  and  $\Delta E_2$  are the energies of the reactions  $(\text{H}_2\text{O})_n \rightarrow n(\text{H}_2\text{O})$ , and  $(\text{H}_2\text{O})_n \rightarrow (\text{H}_2\text{O})_{n-1} + \text{H}_2\text{O}$

	DFTB-D		B3LYP/6-31+G(d)		B3LYP/6-311+G(3df,2p)	
	$\Delta E_1$	$\Delta E_2$	$\Delta E_1$	$\Delta E_2$	$\Delta E_1$	$\Delta E_1$
2H <sub>2</sub> O	-3.4	-3.4	-6.4	-6.4	-4.9	-4.9
3H <sub>2</sub> O	-9.8	-6.4	-19.2	-12.7	-15.0	-10.2
4H <sub>2</sub> O	-18.2	-8.4	-34.0	-14.8	-27.0	-11.9
5H <sub>2</sub> O	-23.8	-5.6	-44.5	-10.5	-35.5	-8.6

calculations results in larger interaction energies, presumably due to basis set superposition effect. DFTB-D interaction energies, on the other hand, are consistently too small, revealing a problem of this method in dealing with hydrogen bonded systems. However, the largest deviation of interaction energy between DFTB-D and B3LYP/6-311+G(3df,2p) is less than 5 kcal/mol per molecule, which is acceptable and sufficient to describe high-temperature water clusters.

### 7.1.2 Pure Graphite Layers

We have studied two model systems of pure graphene layers: C<sub>96</sub> and C<sub>216</sub>. The model systems were terminated with hydrogen atoms, and arranged using the experimentally favored ABA layer scheme. We noticed that DFTB-D predicts inter-layer distances that are too small by almost 0.2 Å, but that layer binding energies per atom are reproduced within a few tenth of a kcal/mol. This finding demonstrates the usefulness of DFTB-D for the description of interlayer interactions in graphite, and we are confident to use this methodology in figure QM/MD simulations of reactions on multi-layer graphite surfaces.

### 7.1.3 Water Clusters on Graphite

Because even the C<sub>96</sub> system is too large for practical investigations using pure DFT calculations, we have explored the usefulness of a two-layer ONIOM approach, where 7 heptagons at the center of the C<sub>96</sub> graphene sheet are treated at a high level B3LYP/6-31+G(d) level of theory, together with  $(\text{H}_2\text{O})_n$ ,  $n=1-5$  clusters adsorbed on top of them. The low level of theory in these ONIOM2 calculations is DFTB-D. We found that O-O distances (intramolecular water geometries) are reproduced by B3LYP and DFTB-D very reasonably, as was mentioned in paragraph 2.1.a. However, O-C(surface) distances are computed much too small at the pure DFTB-D level of theory, once more

emphasizing the problems of this method to deal with intermolecular interactions. However, trends are systematic compared to the ONIOM results, as the O-C(surface) bonds become increasingly longer with increasing water cluster size, and for qualitative exploratory investigations of water-graphene reactions, the qualitatively accurate description of this effect is most important and well reproduced at the DFTB-D level.

Table 10 illustrates the differences between a) ONIOM and pure DFT calculations on one hand, and b) ONIOM and pure DFTB-D calculations on the other. Concerning a), it can be seen that the addition of more circumcoronene layers around the 7-hexagon high-level ONIOM model leaves the interaction energies of the water clusters with the graphene layer virtually unchanged. DFTB-D again delivers rather crude agreement with

**Table 10.** The binding energies (kcal/mol) of H<sub>2</sub>O clusters on the surface of the single-layer graphite C<sub>96</sub>H<sub>24</sub> calculated at the ONIOM and DFTB-D, and B3LYP levels. Here, BE1 and BE2 stand for the energy of the reactions C<sub>96</sub>H<sub>24</sub>(H<sub>2</sub>O)<sub>n</sub> → C<sub>96</sub>H<sub>24</sub> + (H<sub>2</sub>O)<sub>n</sub> and C<sub>96</sub>H<sub>24</sub>(H<sub>2</sub>O)<sub>n</sub> → C<sub>96</sub>H<sub>24</sub> + n(H<sub>2</sub>O), respectively.

	ONIOM(B3LYP/6-31+G(d): DFTB-D)		DFTB-D		B3LYP/6-31+G(d) <sup>a)</sup>	
	BE1	BE2	BE1	BE2	BE1	BE2
H <sub>2</sub> O	-1.8	-1.8	-2.9	-2.9	-2.1	-2.1
2H <sub>2</sub> O	-2.3	-8.8	-4.8	-8.2	-2.3	-8.7
3H <sub>2</sub> O	-1.9	-21.1	-7.1	-16.9	-2.2	-21.4
4H <sub>2</sub> O	-1.2	-35.2	-8.4	-26.6		
5H <sub>2</sub> O	-2.6	-41.7	-10.6	-34.4		

a) B3LYP calculations were performed for the C<sub>24</sub>H<sub>12</sub> model system.

pure DFTB calculations concerning interaction energies between water clusters and graphite surfaces, yet the difference is less than 10 kcal/mol per water molecule, which can be considered acceptable for exploratory high-temperature QM/MD simulations. In particular, geometries obtained at DFTB-D are very reasonable when compared to ONIOM geometries.

#### 7.1.4 Summary

In summary, we conclude that for the description of water on graphene sheets, the DFTB-D level of theory performs reasonably well when compared to computationally expensive high-level *ab initio* B3LYP/6-311+G(3df,2p) calculations, as well as in comparison to two-level ONIOM(B3LYP/6-31+(G(d):DFTB-D) calculations. We are therefore confident to employ the DFTB-D method (abbreviated DFTB-D in the following paragraphs) in further high-temperature QM/MD simulations of water-graphene interactions, as well as for systems containing OH and H radicals interacting with perfect as well as defect-containing graphene sheets. Similar studies on interactions of NO and CO with graphene sheets are underway.

#### 7.2 Dissociative Adsorption of H<sub>2</sub>O on Graphite

As test case for an ONIOM(B3LYP:DFTB-D) exploration of stationary points on the water-graphite reaction system, we found two dissociative adsorption pathways of a water molecule by manual search on a single coronene C<sub>1</sub> and dicircumcoronene S<sub>1</sub> molecule. **Figure 21** illustrates these reaction pathways, one connecting all three *ortho*-

(**P1**), *meta*- (**P3**), and *para*- (**P2**) products with multiple TS's, the other one connecting reactants and the *para*-product directly via a single **TS2**. Zero-point corrected energetics and imaginary frequencies are given for ONIOM(B3LYP/6-31+G(d):DFTB-D) and DFTB-D using **S1**, and for B3LYP/6-31+G(d) and DFTB-D using **C1** graphite monolayers. Compared to corresponding stationary states on the **C1** graphite model, the larger **S1** graphite model shifts TS and product energies down by up to about 8 kcal/mol, indicating that the more extended p-conjugated **S1** system stabilizes sp<sup>3</sup>-defects better than the smaller **C1** model. This finding is true for both ONIOM/B3LYP as well as DFTB-D levels of theory, and affirms our previous evaluation that a graphite model of size **S1** is required to correctly account for the horizontal bulk graphite effect. Consistent with chemical intuition and previous findings, the energy order of dissociative water adsorption products is *ortho* (**P1**) < *para* (**P2**) < *meta* (**P3**) at all levels of theory for both graphite models. In the following discussion of individual reaction pathways, we will only refer to ONIOM results for model **S1** for the sake of simplicity, other energetics are given in **Fig. 21** and Cartesian coordinates of all structures at all levels of theory are provided in the Supplemental Material. Starting from a weakly bound reactant complex **RC1**, **TS1** leads via a 83.5 kcal/mol barrier to the energetically most favorable *ortho*-addition product **P1**, which is 65.3 kcal/mol endothermic with respect to the reactants. This *ortho*-product **P1** with its very local distortion of the graphite p-conjugation is directly connected with the *meta*-product **P3** via a late **TS3** with a relative energy of 98.4 kcal/mol. The geometry of *meta*-product **P3** resembles that of an allylic system, with the radical center in between C-OH and C-H sp<sup>3</sup> sites. Finally, this product can convert into the *para*-product **P2** via a barrier of 6.0 kcal/mol for **TS4**. As to the direct pathway to **P2**, we find that a **TS2** with 92.1 kcal/mol relative energy exists, connecting a pre-positioned water molecule with hydrogen atoms pointing in 1,4-positions of the closest graphite hexagon in structure **RC2** with the asymmetric dissociation product **P2**, which is endothermic with respect to reactants by 70.5 kcal/mol energy. All transition states have been confirmed by vibrational mode analysis and possess only one imaginary frequency, which can differ on the order of several hundred wavenumbers between DFTB-D, B3LYP and ONIOM(B3LYP:DFTB-D). However, qualitatively, DFTB-D predicts the same TS's as B3LYP at a small fraction of the computational cost and can therefore be efficiently used in the search for TS's, before more expensive ONIOM calculations are employed for more accurate characterization. IRC calculations verifying the reaction pathways were only carried out at the DFTB-D level of theory for the **C1** model, as IRC calculations are computationally extremely demanding.

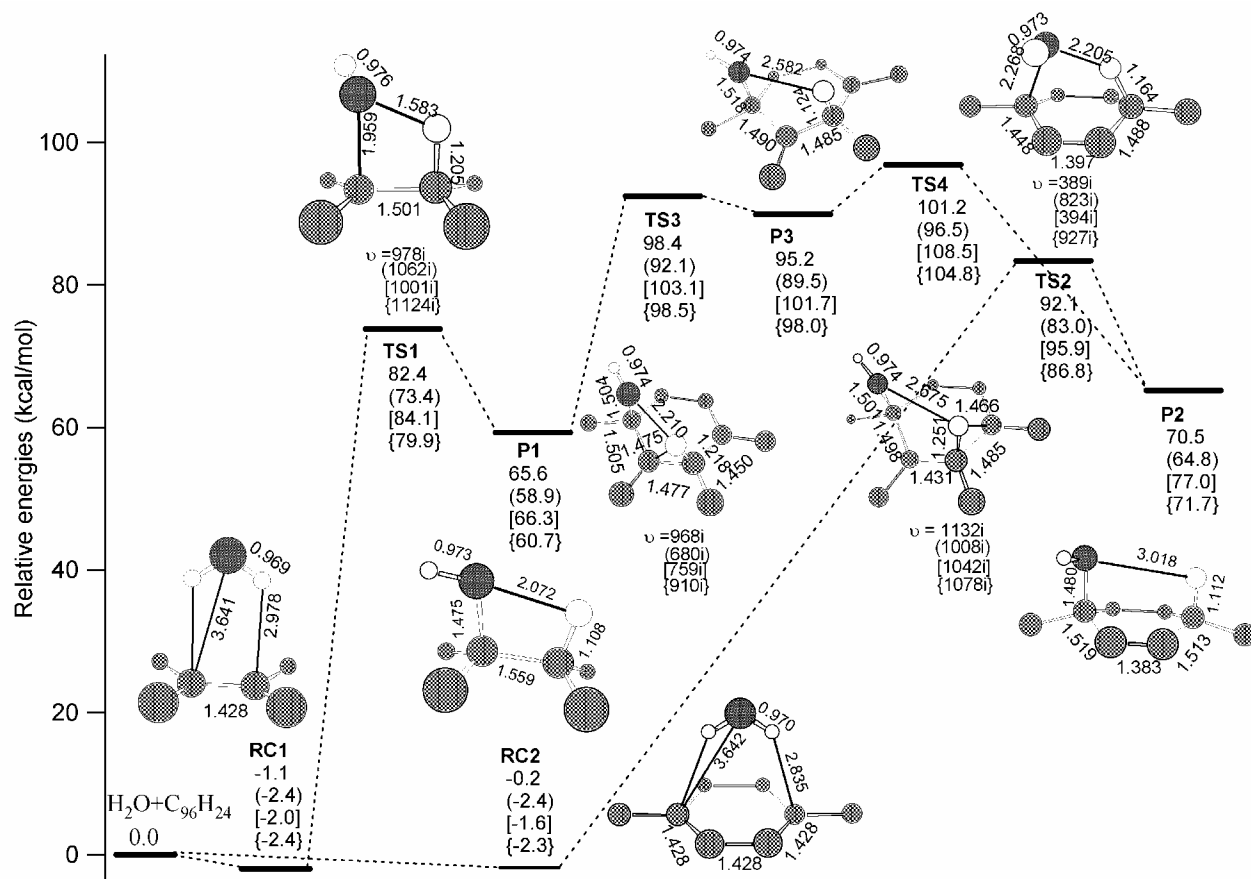


**Figure 21.** Schematic reaction pathways, zero-point corrected energetics, and optimized stationary structures of reactants, products, and transition states of two water dissociative reactions on  $C_1$  and  $S_1$  graphite model systems. Plain numbers denote ONIOM(B3LYP/6-31+G(d):DFTB-D) results and numbers in parenthesis DFTB-D results using the  $S_1$  graphite model, and numbers in square and curly brackets denote B3LYP/6-31+G(d) and DFTB-D results using the  $C_1$  graphite model, respectively.

The rate constants of the one-step H<sub>2</sub>O dissociative adsorption reactions via **RC1** to **P1** and **RC2** to **P2** on **S<sub>1</sub>** have been predicted by the ChemRate program,<sup>48</sup> based on the energetics and vibrational frequencies obtained by the ONIOM(B3LYP/6-31+G(d):DFTB-D) method. According to ChemRate, the predicted rate constants for the two processes:



in the temperature range from 1000 to 5000 K can be represented respectively by Eqs. (3)-(4) in units of cm<sup>3</sup>/s:

$$k_1 = 1.5 \times 10^{-27} \times \exp(-46300/T) \quad (3)$$

$$k_2 = 1.7 \times 10^{-28} \times \exp(-51100/T) \quad (4)$$

The rate constants for the dissociative adsorption processes ( $k_i$ ) are defined by Eq. (5)<sup>49</sup>:

$$d[\text{X}]_{\text{surf}}/dt = k_i (\theta/A_s) [\text{X}]_g \quad (5)$$

which has the unit of a flux, *molecule/cm<sup>2</sup>/s*. In the rate equation  $\theta$  represents the fraction of available surface sites,  $A_s$  is the surface area and  $[\text{X}]_g$  is the gas phase concentration of H<sub>2</sub>O in molecules/cm<sup>3</sup>. The above result means that on account of the very high barriers and low rate constants for the dissociative adsorption processes, the dissociative reactions of H<sub>2</sub>O on a defect-free graphite surface can only occur at extremely high temperatures.

### 7.3 Dissociative Adsorption of CO<sub>2</sub> on Graphite

The dissociative adsorption of CO<sub>2</sub> on graphite has been calculated by DFTB-D and ONIOM(B3LYP/6-31+G(d): DFTB-D) methods using the C<sub>96</sub>H<sub>24</sub> **S<sub>1</sub>** model surface. Three dissociative adsorption processes giving CO + O(a) and CO(a) + O(a), have been identified; where (a) stands for an adsorbed state. Geometries and PESs for these reactions are shown in **Fig. 22**. In the first path, CO<sub>2</sub> dissociates to CO + O(a) by the Rideal-Eley mechanism with a 93.7 kcal/mol endothermicity, occurring with a 116.9 kcal/mol barrier calculated by the ONIOM method. In the second path, CO<sub>2</sub> reacts with graphite to give a 4-centered OC-O-CC- local structure (**P3**) with an endothermicity of 79.8 kcal/mol, via a transition state with an 82.2 kcal/mol barrier. **P3** can dissociate to give an O< + -O-C-C-C- ring-structure (**P4**) with an overall endothermicity of 201.4 kcal/mol and an O< + O=C< structure (**P5**) with an endothermicity of 155.8 kcal/mol. The formation of **P4** takes place with a 220.3 kcal/mol barrier and that of **P5** with a 163.3 kcal/mol barrier. In the third path, CO<sub>2</sub> reacts with graphite to give a 6-centered OC-C-O-C-C- (**P2**) structure with an endothermicity of 154.5 kcal/mol with a 154.7 kcal/mol barrier. The transition states have all been confirmed by the vibrational mode analyses each with one imaginary frequency. The rate constants of the CO<sub>2</sub> dissociative adsorption reactions have been predicted by the ChemRate Program<sup>48</sup> based on the energetic predicted by the more reliable ONIOM method. The predicted rate constants for the 3 processes are given by reactions R6-R8:



in the temperature range from 1000 to 5000 K. The corresponding rate constants can be represented respectively by the Eqs.(6)-(8) in units of cm<sup>3</sup>/s:

$$k_1 = 7.3 \times 10^{-10} \exp(-88600/T) \quad (6)$$

$$k_2 = 1.7 \times 10^{-11} \exp(-139300/T) \quad (7)$$

$$k_3 = 9.9 \times 10^{-11} \exp(-110900/T) \quad (8)$$

Here the rate constants for the dissociative adsorption processes ( $k_i$ ) have been defined above for the H<sub>2</sub>O adsorption/decomposition processes. On account of the very high barriers for the dissociative adsorption processes, the effect of CO<sub>2</sub> on the erosion of a defect-free graphite surface is expected to be negligible.

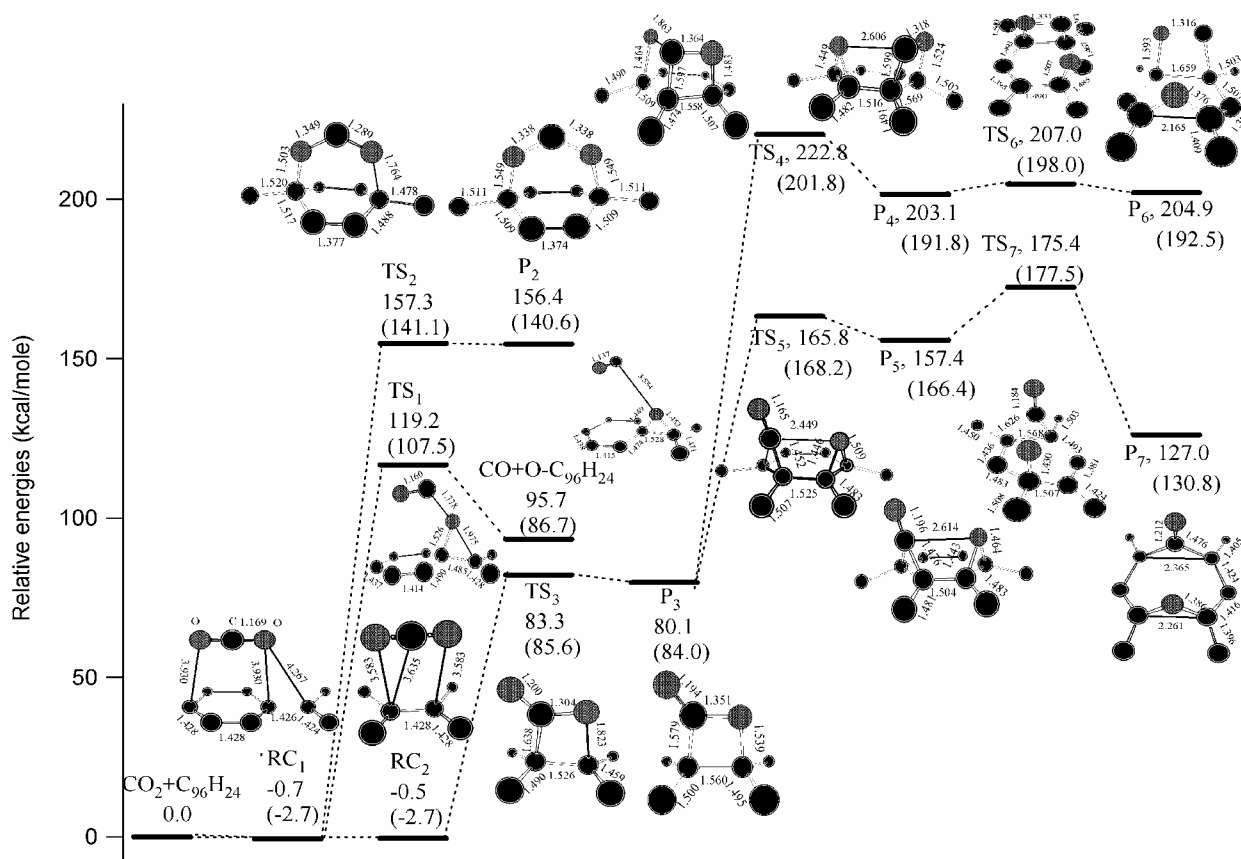


**Figure 22.** Optimized geometries and potential energy surface of the CO on the surface of C<sub>96</sub>H<sub>24</sub> graphite calculated by the ONIOM(B3LYP/6-31+G(d):DFTB-D) without ZPE corrections and DFTB-D with ZPE corrections (data in parenthesis) methods, energies are in [kcal/mol].



## 7.4 Reactions of W/W<sup>+</sup> with H<sub>2</sub>O

We have carried out calculations for the reactions of the M = W atom and M = W<sup>+</sup> ion with H<sub>2</sub>O at the CCSD(T)/(SDD + 6-311G(d,p) // B3LYP/(SDD + 6-31G(d,p)) level of theory. The results of the calculation show that the reaction of W atom with H<sub>2</sub>O can occur without an intrinsic barrier initially giving the H<sub>2</sub>OM complex ( $\Delta H^\circ = -24.3$  kcal/mol for singlet state, -14.1 kcal/mol for triplet state, and -14.2 kcal/mol for quintet state) which rapidly isomerizes consecutively to HWOH ( $\Delta H^\circ = -83.0$  kcal/mol for singlet state, -75.8 kcal/mol for triplet state, and -53.0 kcal/mol for quintet state) with a barrier of 14.7 kcal/mol for singlet state, 5.5 kcal/mol for triplet state, and 20.0 kcal/mol for quintet state and to H<sub>2</sub>WO ( $\Delta H^\circ = -136.5$  kcal/mol for singlet state, -123.9 kcal/mol for triplet state, and -37.3 kcal/mol for quintet state), where the energies are 0 K values. The final primary products for the reactions of W + H<sub>2</sub>O are H<sub>2</sub> + WO. For the reaction of W<sup>+</sup> with H<sub>2</sub>O, the reaction of the doublet state is similar to the reaction of W with H<sub>2</sub>O.

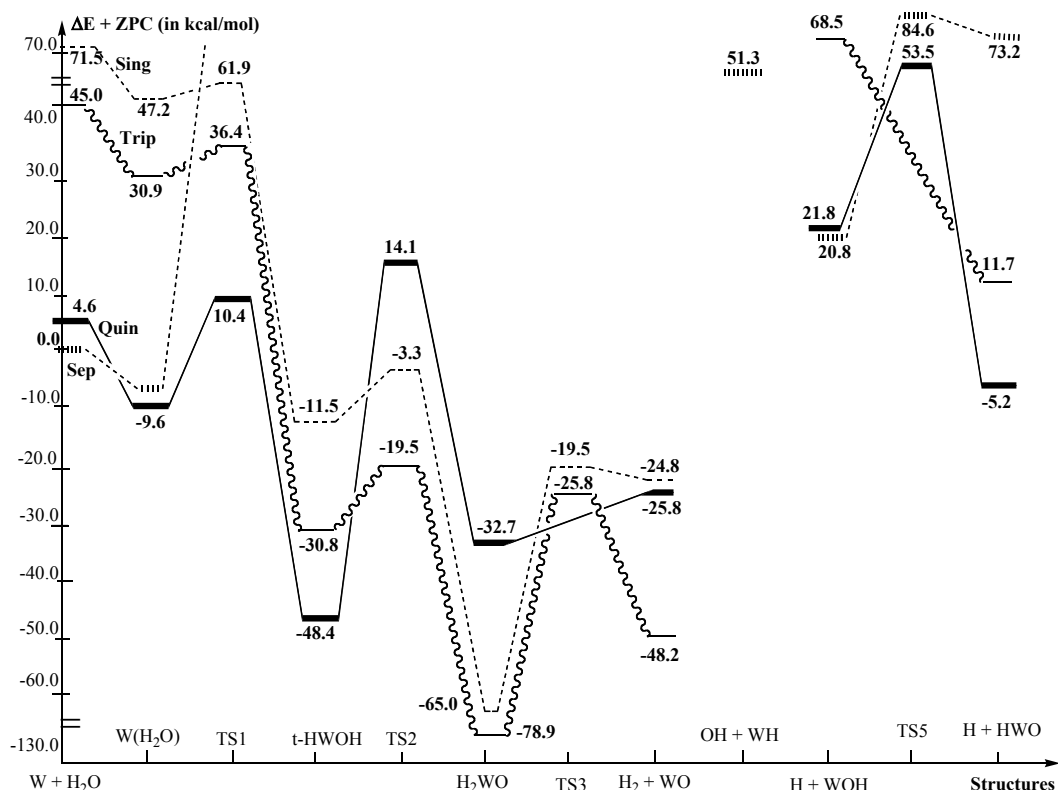


**Figure 23a** Schematic presentation of potential energy surface of the reaction W+H<sub>2</sub>O at various lower-lying electronic states of reactants

However, for the reactions of the quartet and sextet W<sup>+</sup> with H<sub>2</sub>O, the primary products are H + W<sup>+</sup>HO. The entire PES for neutral and cationic species is shown in **Figs. 23a** and **23b**, respectively.

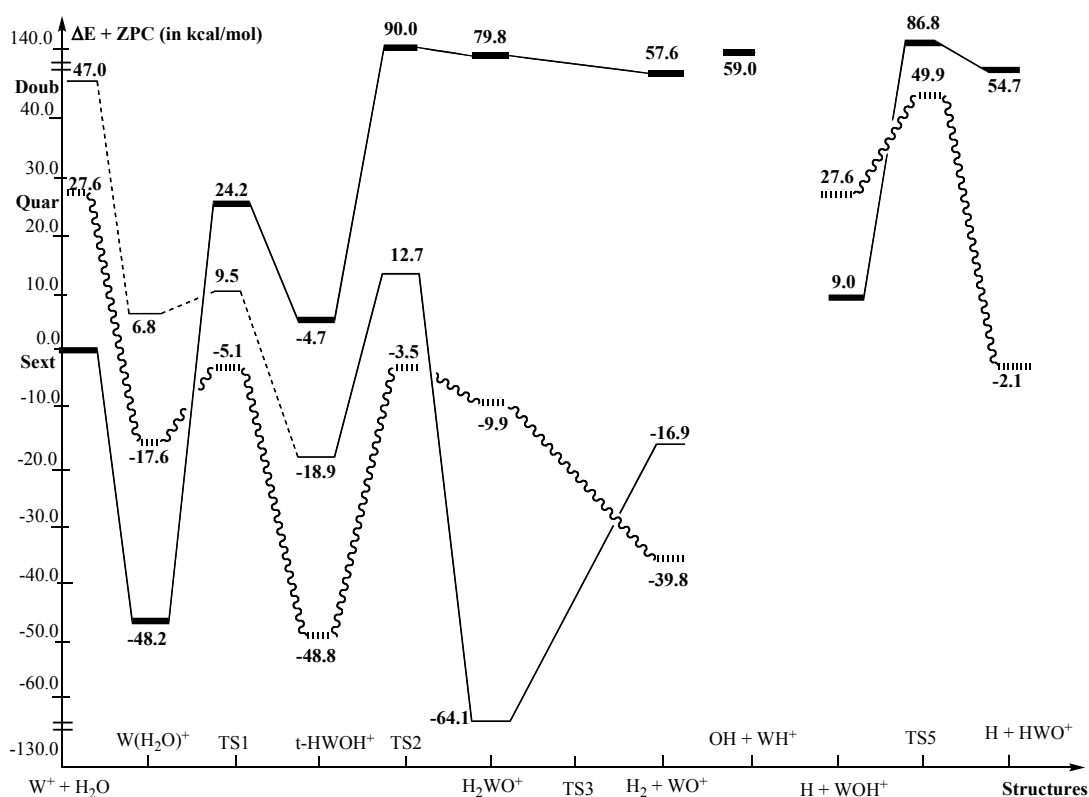
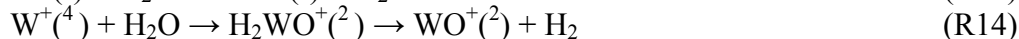
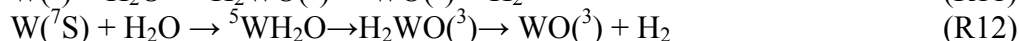
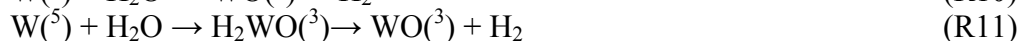


**Figure 23b** Schematic presentation of potential energy surface of the reaction  $W^+ + H_2O$  at various lower-lying electronic states of reactants, intermediates and products

The rate constant for the  $W + H_2O$  and  $W^+ + H_2O$  reactions are under calculation using the variational RRKM theory with the Variflex code.<sup>50</sup> The reactions for the following seven processes are predicted by R9-R15 :



The predicted rate constants in the temperature range from 200 to 3000 K can be represented respectively by the Eqs. (9)- (15) in units of  $cm^3/s$ :

$$k_1 = 2.0 \times 10^{-10} T^{0.26} \exp [-(30/T)] \quad (9)$$

$$k_2 = 4.8 \times 10^{-10} T^{0.16} \exp [-(44/T)] \quad (10)$$

$$k_3 = 9.8 \times 10^{-8} T^{-0.42} \exp [-226/T] \quad (11)$$

$$k_4 = 2.8 \times 10^{-9} T^{0.19} \exp [-67/T] \quad (12)$$

$$k_5 = 1.7 \times 10^{-9} T^{0.05} \exp [-(39/T)] \quad (13)$$

$$k_6 = 4.8 \times 10^{-9} T^{0.05} \exp [-60/T] \quad (14)$$

$$k_7 = 3.1 \times 10^{-9} T^{0.06} \exp [-42/T] \quad (15)$$

These results show that the reaction of W and W<sup>+</sup> with H<sub>2</sub>O can occur readily and lead to oxidation products of tungsten.

## 7.5 Reactions of CO and OH with Pristine Graphite Surfaces

### *7.5.1 Reactions of CO with a Pristine Graphite Surface*

We have investigated the CO/pristine graphite system using the DFTB-D and ONIOM(B3LYP/6-31+G(d):DFTB-D) methods using a C<sub>96</sub>H<sub>24</sub> defect-free model surface. We found that dissociative addition reactions of CO with pristine graphite are even more endothermic than with CO<sub>2</sub> due to the chemical inertness of the CO molecule, and we conclude that the dissociative addition process of CO is not likely to play a role in the nozzle erosion process. The predicted rate constant for the process CO + C<sub>96</sub>H<sub>24</sub> → P<sub>1</sub> in the temperature range 1000 - 5000 K can be represented by Eq. (16) in units of cm<sup>3</sup>/s:

$$k = 1.09 \times 10^{-12} \exp(-48600/T) \quad (16)$$

### *7.5.2 Reaction of the OH Radical with a Pristine Graphite Surface*

For the dissociative adsorption processes of the OH radical on graphite, the mechanism and energetic are completely different from the reactions of H<sub>2</sub>O, CO<sub>2</sub>, and CO with pristine graphite. Without undergoing a physisorption process, the OH radical can add directly to a carbon atom of the graphite surface to give a radical R<sub>1</sub> (HO-site) with 8.1 kcal/mol exothermicity. The OH in R<sub>1</sub> can dissociate to P<sub>1</sub> (site-H + O-site) with a 42.8 kcal/mol endothermicity by overcoming a 51.3 kcal/mol barrier at TS<sub>1</sub>. Furthermore, P<sub>1</sub> can isomerize in various ways undergoing transition states that are associated with feasible barrier heights at the prevailing high-temperature conditions.

The rate constant for the OH + C<sub>96</sub>H<sub>24</sub> → P<sub>1</sub> can be represented by Eq. (17) in units of cm<sup>3</sup>/s:

$$k = 1.46 \times 10^{-12} \exp(-30,000/T) \quad (17)$$

The magnitude of the rate constant for the OH dissociative adsorption reaction on graphite is considerably greater than those of analogous reactions involving H<sub>2</sub>O, CO<sub>2</sub>, and CO, as one should expect.

## **8. Literature Survey and Database Compilation on Nozzle Materials (Koo Group at UTA)**

### 8.1 Literature Survey

Literature search was conducted on rocket nozzle material selection and materials property data by the team members at the **University of Texas-Austin** and Air Force Research Laboratory/Edwards AFB librarians. A list of papers and reports were obtained for this task, these papers and reports will be transferred to **Kuo** at PSU. Selective papers and reports will be posted under Technical Papers at the MURI: Rocket Nozzle Erosion Minimization (RNEM) website: [www.mne.psu.edu/muri-rnem/index1.htm](http://www.mne.psu.edu/muri-rnem/index1.htm). A list of papers and reports are included in reference section of the report<sup>51-99</sup>. This list will be updated periodically.

## 8.2 Survey of rocket propulsion companies

Several rocket propulsion companies were visited namely **Aerojet at Sacramento, CA** (under AFRL/Edwards AFB funding) and **ATK Thiokol, Brigham City, UT** (under AFRL/Edwards AFB funding) in Sept. 2004. **Kuo's** group discussed the needs of a **carbon/carbon** composite as a rocket nozzle throat material for our MURI research program especially for ultra-high pressure tests. **Paul Marchol** of **Aerojet** recommended a **Fiber Materials, Inc. (FMI)** coarse weave (CW) 4D carbon/carbon material for our studies. He also gave technical reports on “Mechanical and Thermal Properties of FMI’s Coarse Weave 4D Carbon/Carbon” and “Mass Loss Testing of Carbon-Carbon at High Temperatures,” Aerojet’s NPE and MSDS for the C/C composites, and a summary of the FMI’s CW-4D Carbon-Carbon properties including tensile strength, tensile strain, elastic modulus, compressive strength, compressive strain, shear modulus, shear strength, coefficient of thermal expansion, thermal conductivity, and thermal heat capacity. These are ITAR restricted reports and should be treated accordingly. Copies were sent to **Kuo** at PSU for reference.

Tom Richardson of ATK Thiokol, Brigham City, UT provided limited ITAR sensitive data of their Integrated High-Payoff Rocket Propulsion Technology (IHRPT) Phase I demo 3-D C-C throat properties (excerpts from AFRL-PR-ED-TR-2001-0025 report). The following properties are available (the data were sent to **Kuo** at PSU for reference):

- Bulk density
- Radial thermal conductivity
- Hoop thermal expansion
- Axial compressive strength
- Axial compressive strain
- Hoop ring tensile strength
- Hoop ring tensile strain
- Hoop compressive strength
- Hoop compressive strain

## 8.3 Baseline nozzle material

At the advice of Dan Miller of NAVAIR-China Lake, G-90 graphite manufactured by Metaullics in Sanborn, NY (<http://www.metaullics.com>) was selected as our baseline rocket nozzle throat material for relatively high pressures. After communicating with Rick Corbi (Sales Product Manager, Specialty Graphite for Metaullics), physical, mechanical, thermal properties were obtained and are included in **Tables.11-13** and **Fig. 24**. **Table 11** shows the density, flexural, ash content, and CTE of the 9-inches in diameter G-90 rod. The average value of density is 1.918 g/cc, flex is 4,269 psi, ash content is 0.0097%, and CTE is  $1.89 \times 10^{-6}/\text{C}$ . **Table 12** shows the average flex and ash content values of the 2½-inches G-90 rod where the average values of flex is 4,082 psi and ash (pph) is 0.02.

**Table 11.** Physical, mechanical, and thermal properties of the 9-inches in diameter G-90 graphite rod.

Sample ID#	Density (g/cc)	Flex (psi)	Ash (%)	CTE (RT - 300°C) $\times 10^{-6}/C$
1	1.922	4411	0.011	1.86
2	1.908	4150	0.009	1.87
3	1.912	4284	0.003	1.95
4	1.925	4523	0.011	1.91
5	1.913	4454	0.010	1.95
6	1.904	4184	0.015	1.91
7	1.926	4237	0.015	1.89
8	1.925	4010	0.008	1.79
9	1.923	4415	0.011	1.86
10	1.924	4024	0.004	1.86

**Table 12.** Physical and mechanical properties of the 2 ½-inches in diameter G-90 graphite rod.

Sample ID#	Flex (psi)	Flex (avg) (psi)	Ash (pph)
1	3650	3426	0.01
1	3201		
2	4147	4234	0.03
2	4321		
3	3518	3439	0.01
3	3359		
4	3980	3908	0.01
4	3835		
5	4864	4769	0.02
5	4674		
6	4692	4718	0.01
6	4744		
<b>Average</b>	<b>4082</b>		<b>0.02</b>

**Figure 24** shows the thermal expansion tests conducted according to ASTM E228. The samples were tested in air from room temperature to 300°C at a heating rate of 1 °C/min. It shows the G-90 behavior of the percentage of thermal expansion versus temperature. **Table 13** shows the values of percentage of thermal expansion and coefficient of thermal expansion versus temperature obtained by fitting a fourth order polynomial curve to the experimental data. The estimated accuracy of these tests is  $\pm 1\%$ .

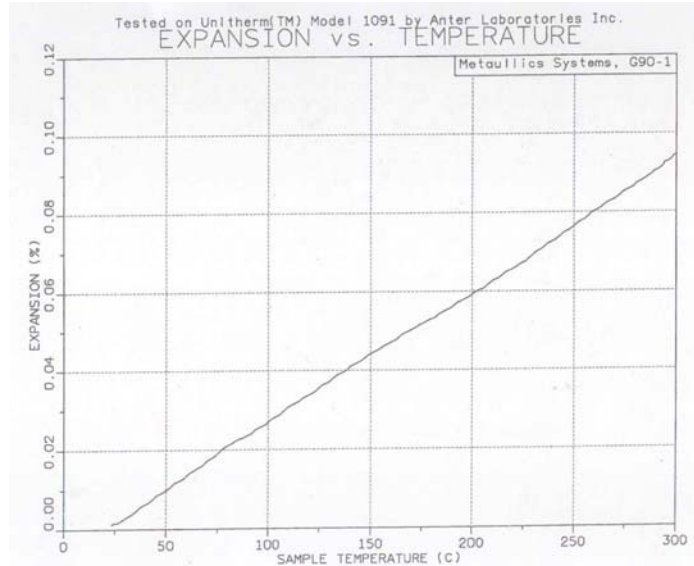


**Figure 24.** Thermal expansion percentage versus temperature of G-90 graphite.

**Table 13.** Thermal expansion versus temperature values of G-90 at 23 °C.

#### THERMAL EXPANSION TEST RESULTS

CALCULATIONS (normalized to 23 degrees C):

Data file name : E6517.010

Data file information: Metaullics Systems, G90-1

Starting Date 01/09/03

Starting Time 06:55:06

Test Number 5781

Delay .5

Safety Limit 500

Repeat 0

Sample ID No. E6517

Sample Length (in) 1.98625

Uncorrected coefficients:

X<sup>0</sup> -4.6308577856E-05

X<sup>1</sup> 2.2872027942E-06

X<sup>2</sup> 1.6064625809E-09

X<sup>3</sup> -1.0249924679E-11

X<sup>4</sup> 2.4602101149E-14

X<sup>5</sup> 0.0000000000E+00

Corrected coefficients:

-8.4526159506E-05

3.7295350394E-06

-2.3550006733E-09

-1.0072782250E-12

1.7526058508E-14

0.0000000000E+00

Correlation Coefficient

(r) : 0.999576

Coefficient of Determination

(rsq) : 0.999152

Standard Error of Estimate

(see) : 0.000006

Referenced to 23 degrees C.

Temp. (C)	Expansion (%)	Inst.Alpha (x10-6/C)	Avg. Alpha (x10-6/C)
25.0	0.001	3.611	3.616
50.0	0.010	3.495	3.557
75.0	0.018	3.389	3.501
100.0	0.027	3.298	3.450
125.0	0.035	3.230	3.404
150.0	0.043	3.192	3.365
175.0	0.051	3.188	3.336
200.0	0.059	3.227	3.317
225.0	0.067	3.315	3.311
250.0	0.075	3.459	3.319
275.0	0.084	3.664	3.342
300.0	0.094	3.937	3.383

## 9. Mechanisms of time dependent nozzle erosion processes (Hanagud, Wilkinson, and Seitzman Group at GaTech)

### 9.1 Erosion tests

#### 9.1.1 Synchrotron X-Ray Diffraction Technique (Background)

This technique is unique and uses the powerful synchrotron X-ray diffraction techniques. Powder X-ray diffraction is the “classic” method for identifying the crystalline. Until relatively recently, the time resolution of the technique has been poor (minutes) due to the low intensity of x-ray sources that are typically available and the limitations of x-ray detector technology. In the last 20 years, the time resolution achievable with x-ray diffraction has improved markedly due to the development of extremely high intensity synchrotron x-ray sources and very high performance 2D detectors. In addition to the very good time resolution that can now be achieved at many 3rd generation synchrotron sources, provide access to very high-energy photons (in some cases, energies in excess of 100 keV). These characteristics combine to enable experiments where x-ray beam penetrating power and a good time resolution are a necessity. In the current test design, we follow in real time the changes that take place on the interior surface of a solid fuel rocket nozzle as the motor is in operation. This experiment will uncover all of the crystalline to crystalline transformations that occur on the surface due to processes such as oxidation and temperature-induced phase transitions, and provide a time line for these processes. There have been previous diffraction experiments looking at processes such as the propagation of solid flame fronts during Self propagating High temperature Synthesis (SHS)<sup>100</sup> and the formation of intermediate phases during the flash setting of cement<sup>101</sup> that have demonstrated adequate time resolution (<100 ms) in less challenging sample environments.

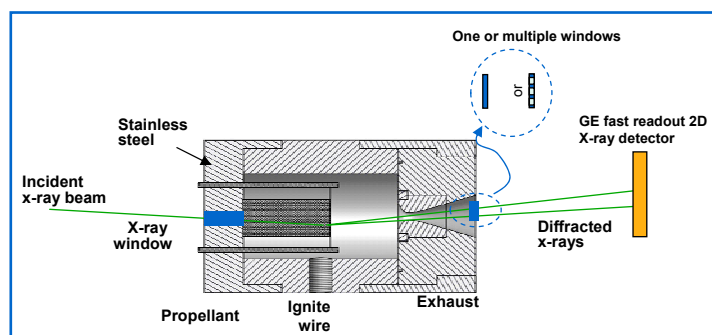


**Figure 25.** General experimental arrangement for *in-situ* time resolved studies of nozzle erosion. Note this is not to scale. 2D X-ray detector would be approximately 3 meters from the exit X-ray window.

With the choice of monochromatic and white beam (energy dispersive) diffraction experiments, the monochromatic approach appears to be superior and will be initially pursued. The combustion chamber would be arranged so that its axis is almost parallel with the synchrotron X-ray beam path, with X-rays entering the combustion chamber



through a window made from sapphire (or some other relatively low atomic number material) and impinging at glancing angles on the throat surface. The scattered x-ray beam would then exit the test equipment through one or several further x-ray transparent windows down stream of the nozzle and be recorded on a fast 2D detector (see **Fig. 25**). We propose to use ~120 keV photons from an undulator at the Advanced Photon Source, Argonne National Laboratory, monochromated using a special high throughput double crystal Laue arrangement. At this photon energy the exit window need only span ~4 degrees. The diffraction patterns can be recorded using a recently developed detector from GE that is based on amorphous silicon technology combined with a scintillator that is optimized for high-energy X- rays. This detector can be read out at up to 30 Hz potentially enabling the acquisition of many diffraction patterns during a single motor burn.

### *9.1.2 Synchrotron X-Ray Diffraction Technique (Progress to date)*

As shown in **Fig. 25**, this task requires a propellant combustion chamber with a nozzle. We have selected the propellants (M & S). We have completed a preliminary design of the combustion chamber. The combustion chamber will be first used to conduct interrupted nozzle tests and optimize test conditions for limited number of tests to be conducted at Argonne National Laboratory with synchrotron X-ray diagnostics “set-up”. We have designed a test matrix to provide an optimum test plan for synchrotron X-ray tests to observe the time-dependent erosion process in a modified strand d burn system. First stage of the strand burn test will be conducted in a pressure range will vary from 1000 to 3000 psi. We are initially considering two throat diameters and three different nozzle materials. The maximum test duration is being determined. However, to study the time-dependent erosion process, tests will be of a duration that will be less than the full duration. The next item of interest in the test matrix is the metallized and non-metallized propellants. First series of tests will be with non-metallized propellants. Following these tests, metallized propellants will be considered, including any needed redesign of the burn strand. The test matrix is designed to conduct first shake down tests to estimate the performance of the burn system. Next series will be to compare the throat diameters. Following the tests, we will explore the needed duration and the pressure realized and needed to study the nozzle erosion. This will be followed by tests to understand the time-dependent process of erosion by studying recovered nozzle at varying duration of times. The last series of tests will be to validate and provide input to ab initio studies. Because the needed number of tests will be large and all tests cannot be included in the test matrix, we are studying the reaction and erosion process by the use of ab initio techniques. In particular we have very encouraging results in our current studies that use ab initio/molecular dynamics (MD) techniques. We expect to supplement the test matrix with results from validated ab initio studies that can replace some of the tests that can not be included in the test matrix.

## 9.2 Nozzle Fabrication

Besides the tungsten and graphite nozzles, we have considered zirconium carbide nozzles. The melting temperature of zirconium carbide at 3,540°C, which is higher than the tungsten materials at 3,410°C. We have completed fabrication of zirconium carbide



nozzles (in addition to carbon and tungsten nozzles). The procedure for fabricating a ZrC nozzle<sup>102</sup> is as follows. First, we obtained preforms of tungsten carbide in the shape of cylinder. The WC preform is plain WC with no metallic binder (not Co bonded WC). The preforms are around 50% dense and thus easy to machine. Secondly, the cylindrical WC preform was machined into the desired nozzle shape. Thirdly, dense, near net-shaped ZrC/W-based nozzles can be fabricated at modest temperatures and at ambient pressure by a reactive infiltration process known as the Displacive Compensation of Porosity (DCP) method. Porous WC preforms with desired nozzle shapes were exposed to molten  $\text{Zr}_2\text{Cu}$  at 1,200–1,300°C and ambient pressure. The  $\text{Zr}_2\text{Cu}$  liquid rapidly infiltrated into the preforms and underwent a displacement reaction with the WC to yield a more voluminous mixture of solid products, ZrC and W. This displacement reaction-induced increase in internal solid volume filled the prior pore spaces of the preforms (“displacive compensation of porosity”) to yield dense, ZrC/W-based composites. Because the preforms remained rigid during reactive infiltration, the final composites retained the external shapes and dimensions of the starting preforms. The starting porosity of WC can be carefully selected to ensure full reaction. WC of 52% starting porosity has resulted in a final Zr/W composite with a phase content of 37.2 vol% tungsten, 60.7 vol% zirconium carbide, and 2.1 vol% copper. A DCP-derived, ZrC/W-based nozzle insert was found to be resistant to the severe thermal shock and erosive conditions of a Pi-K rocket motor test<sup>103</sup> (see **Fig. 26**). The DCP process enables dense, ceramic/refractory metal composites to be fabricated in complex and near net shapes without the need for high-temperature or high-pressure densification or for extensive machining (i.e., relatively expensive processing steps are avoided).

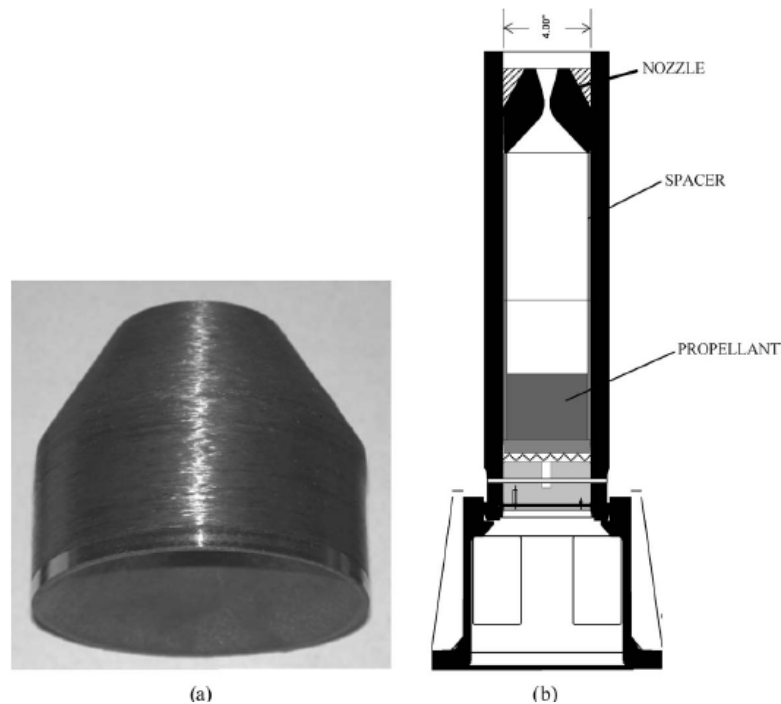


**Figure 26. (a) ZrC/W nozzle insert. (b) Pi-K test motor.**

### 9.3 First Principles Studies of Time Dependant Nozzle Erosion: Chemisorption of CO on tungsten surfaces

#### *9.3.1 Introduction*

In this part of the report, we discuss the redox chemistry of a solid propellant rocket motor nozzle throat material, with propellant combustion products, in the forms of gas of ions and radicals, etc, by using ab initio methods or first principles. The primary objective is to narrow the test matrix for synchrotron X-ray tests at the Argonne national laboratories. The first problem addressed in this work concerns an ab initio study of the chemisorption of CO on tungsten surface at high temperatures. The previous work and inferred results, on this subject, is based on experimental work at a selected temperature and associated models. This work is to examine the previous inference, from ab initio methods, and provide results at higher pressures and other temperatures.

In general, there are many processes that occur at the nozzle/gas interface. These processes involve thermomechanics and chemical reactions. Among these processes, the oxidation/reduction (redox) processes are some of the most important processes that affect the nozzle and the transport of gas species in the subsurface. Redox processes are difficult to understand because the fundamental process of electron exchange between oxidants and reductants can involve multiple pathways and numerous intermediate species and structures, all of which can vary with the specific thermodynamics and chemical conditions. This situation makes theoretical models of electron exchange valuable in providing insight into the fundamental nature of the processes, and indicating how these processes are altered by changes in thermodynamics and chemical conditions. The addition of bulk materials makes the task even more arduous. The simulation region must be large enough so that the reaction involves the chemical participation of the solid<sup>104,105</sup>. Based on redox processes for geochemical analysis (using QM/MM<sup>106,107,108</sup>), in a long term run, we propose to use a QM/MM model to extend these studies to the nozzle erosion problem. First, we study a simplified problem, by selecting the material). tungsten as the nozzle throat material and only one species of combustion product at a time (**Fig. 27**). The reaction of one single species with a selected bulk material under high pressures and high temperature is studied by using ab initio molecular dynamics (ABMD).

This simplified problem can be further divided into two parts. First part is the characterization of nozzle material including the determination of the electronic structure, the equation of state, phase transition, constitutive relation and effect of defects. There is a considerable amount reported research activity on this area. The second part is the study of chemical reactions. On the basis of published literature and review articles<sup>109,110</sup>, quantitative studies of surface reactions are limited to very simple cases.

#### *9.3.2 Ab Initio Studies of Chemical Reactions*

Specifically, the study of chemical reactions involves a study of the surface reactions of the selected nozzle material, tungsten, with propellant decomposition product. In this paper, CO has been selected as one of the propellant decomposition

product. In general, reactions take place at high temperatures and high pressures. In this paper, the study of reactions is restricted to high-temperature effects.

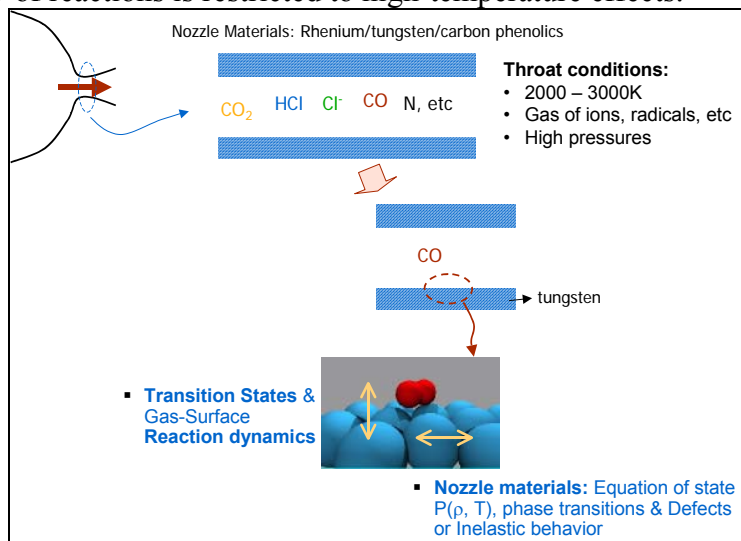


**Figure 27.** Simplification of the problem and the categories of ab initio studies.

The objectives of any theoretical (or ab initio) surface science are to understand the fundamental mechanisms that are taking place at the gas/metal surface interface. This includes all possible processes, including chemical reactions at the surface. In one way, the chemical reactions at the surface can also be classified into two categories. One class of reactions is used, in the chemical industries, to produce useful products. Very often, catalysts are used to accelerate the reactions. A second class of reactions produces undesirable effects such as corrosion wear and erosion of the surface. The present study is focused on understanding the second class of reactions to minimize wear and erosion.

In ab initio studies, the reaction path of interest is the minimum energy path that combines the regions of reactants with the region of products in the potential energy surface (PES). Thus, PES of the system is important in understanding the fundamental mechanisms. In the study of PES of the system, it is necessary to understand the reaction barrier (or the transition states). In studying reactions, to develop useful products, chemists are interested in catalysts that can lower the barrier. In the present study, the objective is to understand the barrier to minimize erosion in future designs. Specifically, in the nozzle erosion problem the reaction barriers are surmounted by the temperature and pressure of the decomposition product. As discussed in the previous section, we focus on the study of the effects of the temperature of CO to overcome the barrier. Very often, the reaction barrier (or the transition state) is considered with a single reaction coordinate. However, the PES is multidimensional and the reaction route can find a path with smaller barriers. Thus, the multidimensional PES is important in discussing chemical reactions<sup>111</sup>. The current computational tools can be used to track the reactants on an abstract PES. Another approach is to track the atomic positions along the reaction path. To understand the mechanism, it is necessary to combine the information of atomic

positions with the information on energetics and the interpolation functions that are used in the computation of the PES.

### 9.3.3 Method of Approach

#### Procedure for ABMD Studies

A Car-Parrinello MD (CPMD) has been selected to simulate the chemical reaction events. CPMD is based on ab initio methods and can produce reaction path for given initial conditions. The kinetic data of reaction can then be obtained through appropriate statistical ensembles through the reaction path. In CPMD, a series of Nosé-Hoover-Chain Thermostats are introduced to control the temperature. A series of barostats are introduced to control the pressure and maintain the ground state, with electron masses used in CPMD. The procedure for the analysis that is required in the paper is listed as follows.

- Input the initial equilibrium system
  - Construct a super cell including gas and the crystalline solid
- Select a specific P, T
  - Calculate the evolution of system at each time step
  - Calculate the free energy at each time step by a NPT ensemble
  - Construct the PES and TS at specific (P, T)

An isotherm-isobaric (NPT) statistical ensemble is used in the above in the calculation of the free energy at each time step (**Fig. 28**). The reaction kinetics can be obtained through the information of free energy as function of reaction coordinates along the reaction path.

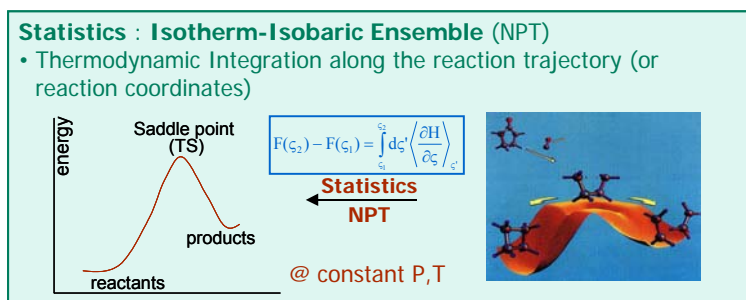


**Figure 28.** NPT to construct PES (CPMD)

#### CO and Tungsten at Temperatures Higher Than 800 °C

The chemisorption of carbon monoxide on tungsten surfaces have been studied and has led to an understanding of the energetics of the adsorption process.<sup>112-120</sup> In the experimental studies, no evidence was found for the dissociation of CO into adsorbed C and O atoms. Many of the experimental results agreed on models that predicted a chemisorption of CO on tungsten. This process involved a surface bonding of both carbon and oxygen<sup>120</sup>. To date, the chemisorption of CO on tungsten surface has not been studied by ab initio methods. The objective of this work is to study the CO chemisorption on the tungsten surface by using ab initio techniques or first principle

based methods. The resulting study will also form a foundation to study reactions of other hot gasses on other metallic or ceramic nozzles, at high pressures.

A super cell is built to simulate the CO + W surface processes. Tungsten is a body-centered cubic (bcc) crystal in space group 229 with Im-3m symmetries (a symmetry group associated with the body centered cubic). The measured cell parameters are  $a = b = c = 3.1652 \text{ \AA}$ . The (100) surface of tungsten was selected, for the study of possible reaction. Carbon monoxide molecules were above the tungsten surface. The studies included variations of selected parameters, like the number of the layers of tungsten, the position of the CO molecule, the environmental temperature and pressure. The number of the layers of tungsten was selected to 3, 4, and 6. The position of the CO molecule included: a configuration with O atom close to the W layer and C atom above the O atom, and the other configuration with an opposite order of C and O atoms. The temperature was first selected at 0 K and 800 °C. In CPMD, a series of Nosé-Hoover-Chain Thermostats are introduced to control the temperature. A series of barostats are introduced to control the pressure. The time step is selected as 5 a.u. (where 1 a.u. = 0.0241888428 fs). We have run 10,000 or 20,000 steps. It gives the entire duration around 0.24 or 0.48 ps.

The density functional theory (DFT) calculations were based on Martin-Troullier type pseudopotentials with in the plane wave basis set. The energy cutoff for the calculation of the gradient correction is 0.2E-07 Rydberg. Becke-Lee-Yang-Parr(BLYP) was employed for the exchange and correlation (xc) functional. The convergence with cutoff values were studied All pseudopotential functions were first initialized on a evenly spaced grid in g-space and then calculated at the needed positions with a spline interpolation The spline points are selected to be 3,000.

#### *9.3.4 Results and Discussions*

1. Number of tungsten layers: Based on the published literature and our experience, it was decided that a larger number of tungsten layers are needed to simulate bulk tungsten. From our studies, we observed that only first four layers of tungsten, which are close to the CO molecule, are involved in the reactions. Therefore, the number of tungsten layers should be chosen larger than four. Therefore, we have selected six layers of tungsten for the studies of reaction of CO with tungsten.

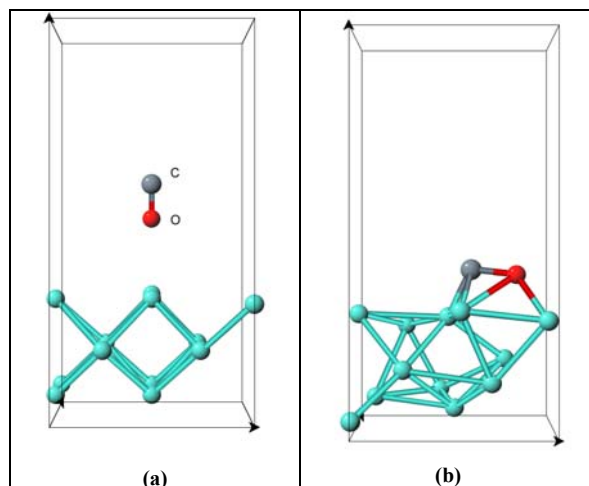


**Figure 29.** Reaction path (at  $T = 800\text{ }^{\circ}\text{C}$ ) of CO + 3 layers of W at time step n:  
(a)  $n = 1$ , (b)  $n = 10,000$  (front view).

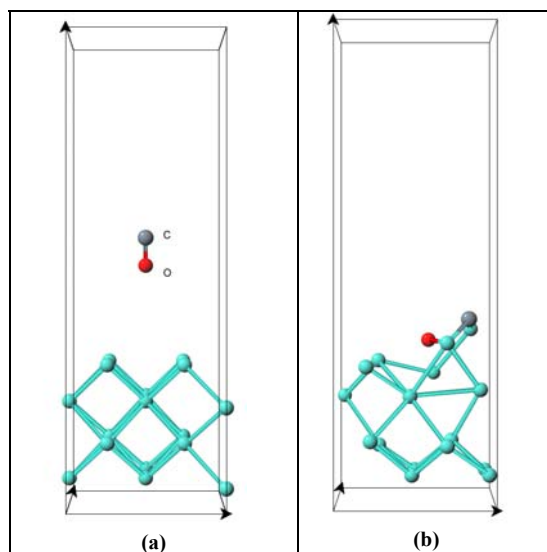


**Figure 30.** Reaction path (at  $T = 800\text{ }^{\circ}\text{C}$ ) of CO + 4 layers of W at time step n:  
(a)  $n = 1$ , (b)  $n = 10,000$  (front view).

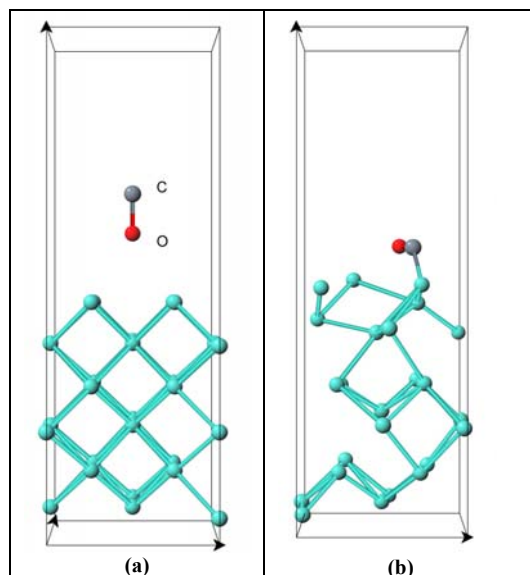


**Figure 31.** Reaction path (at  $T = 800\text{ }^{\circ}\text{C}$ ) of  $\text{CO} + 6$  layers of W at time step n: (a)  $n = 1$ , (b)  $n = 10,000$  (front view).

2. Initial Positions of CO molecule: Two types of initial positions of CO molecule on the top of W surface were studied: (1) with O atom close to the W layer and C atom on the top of the O atom and (2) with C atom close to the W layer and O atom on the top of the C atom. It is seen that the initial positions of the CO molecule does not affect the reactions (**Figs. 31 and 32**).

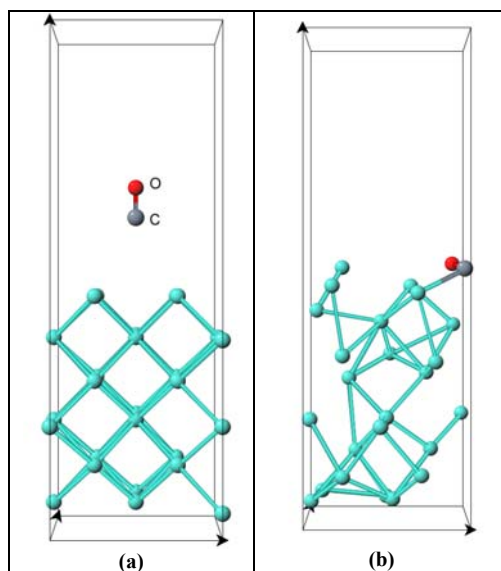


**Figure 32.** Reaction path (at  $T = 800\text{ }^{\circ}\text{C}$ ) of  $\text{OC} + 6$  layers of W at time step n: (a)  $n = 1$ , (b)  $n = 10,000$  (front view).

3. Reaction Temperature: As indicated in the literature, reactions start at temperature greater than 800 °C, not at  $T = 0$  K. This fact was verified by studying the reaction path of CO + 6 layers of W at 0 K. The results are listed in **Figs. 33** and **34**.

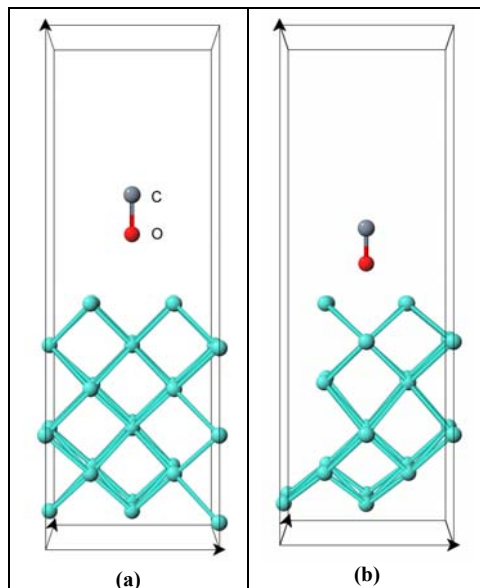


**Figure 33.** Reaction path (at  $T = 0$  K) of CO + 6 layers of W at time step  $n$ :  
(a)  $n = 1$ , (b)  $n = 10,000$  (front view).

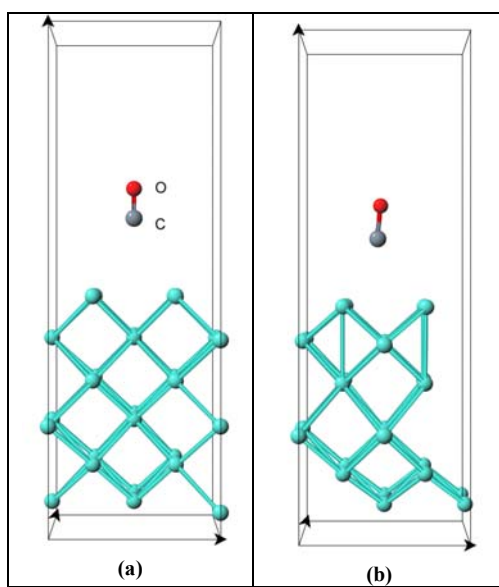


**Figure 34.** Reaction path (at  $T = 0$  K) of OC + 6 layers of W at time step  $n$ :  
(a)  $n = 1$ , (b)  $n = 10,000$  (front view).



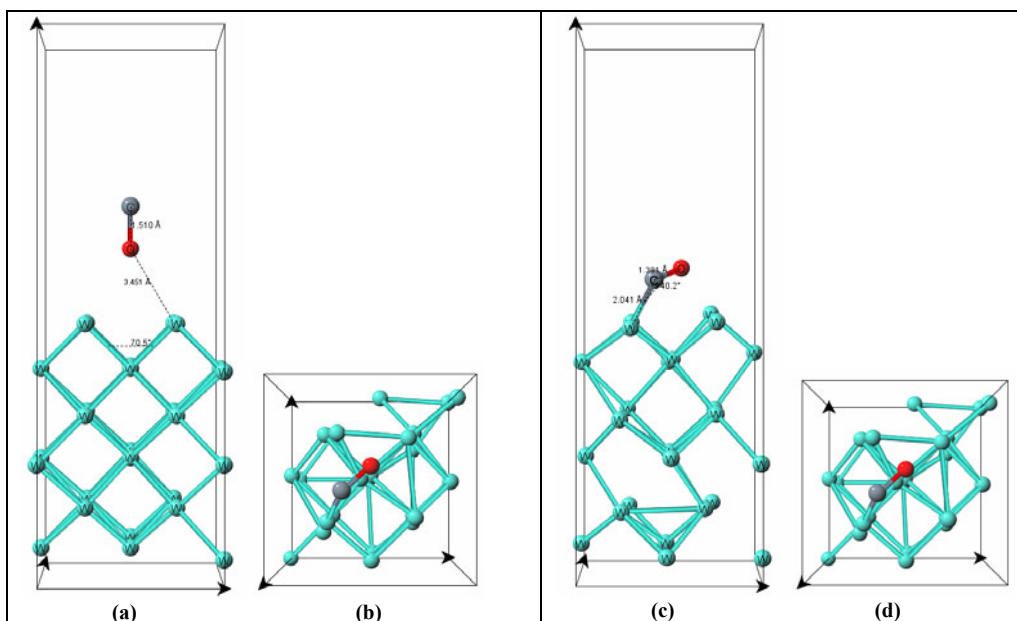


**Figure 35.** Reaction path (at  $T = 800\text{ }^{\circ}\text{C}$  and  $P = 10,000\text{ psi}$ ) of CO + 6 layers of W at time step n: (a)  $n = 1$ , (b)  $n = 10,000$  (front and top views).

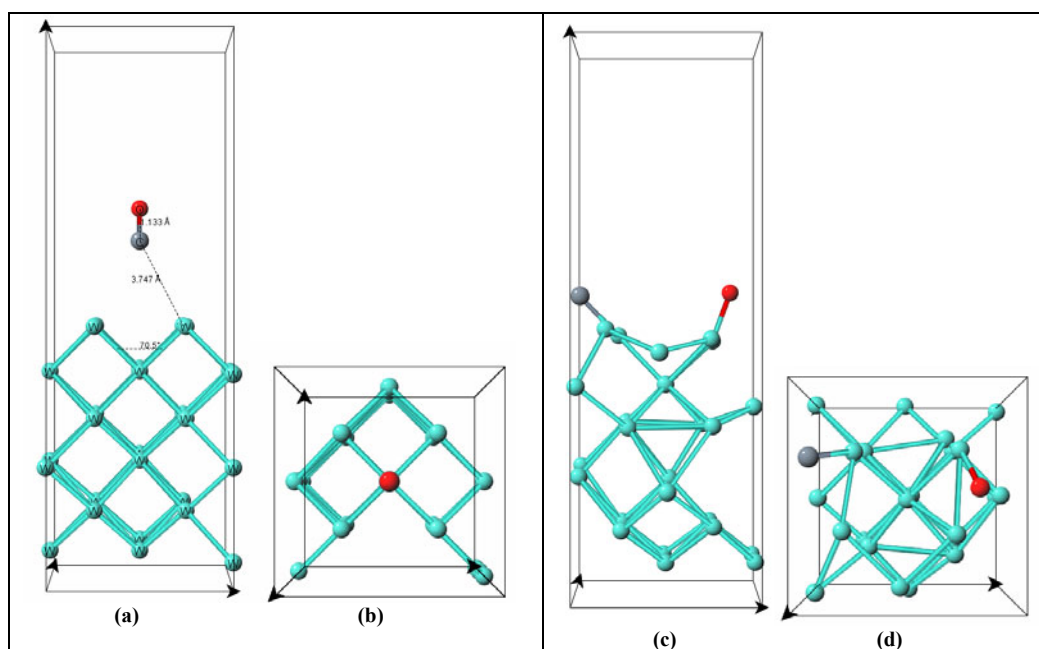


**Figure 36.** Reaction path (at  $T = 800\text{ }^{\circ}\text{C}$  and  $P = 10,000\text{ psi}$ ) of OC + 6 layers of W at time step n: (a-b)  $n = 1$ , (c-d)  $n = 10,000$  (front and top views).

4. Pressure effects on reactions at  $T = 800\text{ }^{\circ}\text{C}$ : Even though the primary objective of the study was the effect of temperature in overcoming the energy barrier, the study also included preliminary work the effects of pressures at the reaction which take place at  $T = 800\text{ }^{\circ}\text{C}$ . We first selected a pressure at 10,000 psi. We used the concept of barostats to introduce an isotropic pressure. Later, pressures with various constraints will be selected. In particular, we are interested in the ‘z-direction pressures’, which only allows the deformation in z-direction. The results are shown in **Figs. 35** and **36**. With pressures, the deployment of the CO molecule does affect the reactions. Different intermediate products are formed when C and O atoms switch their positions. When the O atom is near to the tungsten, only a W-C bond formed and C-O bond remained; however, with the C atom near to the tungsten, the C-O was broken with new bonds W-C and O-W formed. We have obtained the intermediated products. The computation will continue to reach the final product  $\text{WC} + \text{O}$ .
5. Two CO Molecules: Studies were also done, with two CO molecules instead of a single molecule. The results still show no dissociation but a complete bonding with the tungsten surface.
6. Bonding of CO and W: The results clearly indicate that the carbon monoxide does not disassociate into C and O atoms. The results also indicate that there is a complete bonding of carbon and oxygen atoms bond completely to the surface of tungsten. This confirms the inference of previous results that were based on experiments and the associated models. The new results include the effects of higher pressures.
7. High Pressure Chemisorption: In this research effort, we have presented an ab initio study and simulation of the chemisorption of CO on tungsten. This study clearly shows the bonding of C and O atoms on the tungsten surface. The study also clearly indicates that there is no dissociation of C and O atoms and provides results for the chemisorption at high pressures. These studies confirm the previous inferences by experiments and associated models. More importantly, this study forms foundations and a benchmark problem to understand the fundamental mechanisms of different chemical processes that take place at the propellant combustion products and metallic or ceramic nozzle, of a solid propellant rocket motor.

## **10. Simulation of Erosion in a Solid Rocket Nozzle (Menon Group at GaTech)**

In this task, a fundamental study of the underlying processes is being carried out with a goal of developing models that can be used to simulate the erosion process in a rocket nozzle during actual test firing. The methodology developed here will be eventually integrated within a direct numerical simulation (DNS) and/or large-eddy simulation (LES) code to simulate the fully coupled process.

## 10.1 Method of Study

To study how the actual solid propellant combustion products and heat transfer affects the flow in the nozzle we are employing an existing 2D/3D DNS/LES code. This code, denoted LESLIE3D hereafter, is a well-established DNS/LES solver used extensively for combustion studies. It is a finite-volume structured grid solver that is second-order accurate in time, and second or fourth order accurate in space. Typically, simulations are run using the second order accurate option but final statistics are collected using the fourth order option. The code has been extensively validated for single phase and two-phase gas turbine combustion, spray combustion and solid propellant combustion. It is highly optimized in parallel using MPI and runs on all parallel machines available to us.

For the current study, this code has been set up to simulate flow of the hot burned products from just upstream of the nozzle to the supersonic outflow. Isothermal wall conditions have been employed (using wall temperature profile based on our past studies) in order to predict heat flux into the wall. This setup allows prediction of what surface forces, chemical species, and heat flux are at the rocket nozzle surface. However, in order predict the effects of these thermo-fluid properties on nozzle erosion, additional issues have to be modeled. So far we have identified four effects that have to be modeled and incorporated into the code:

1. Effect of surface kinetics on the wall properties and erosion process.
2. Effect of wall shear forces (both tangential and normal) on the erosion process.
3. Effect of wall heat flux on the erosion process
4. Effect of particle impact on the erosion process
5. Effect of particle melt layer on the erosion process

Other processes may be important but these five effects are considered the most important ones to consider. Since the scale at which these processes impact the surface behavior is very small, full resolution of these processes is nearly impossible based on current availability of resources. Therefore, we are exploring the development of a new unique subgrid model that incorporates most of the physics in a fundamental manner but resides within the grid resolution typically used for LES. In the following, we briefly summarize the progress in incorporating each of the above effects.

### *10.1.1 Effect of surface kinetics on the wall properties and erosion process*

Although LESLIE3D code has the capability to simulate arbitrary number of chemical species in the gas or solid phase, additional models for surface kinetics have to be incorporated in order to account for chemical reactions between gas species and the surface. Our current approach is to integrate a version of SURFACE CHEMKIN<sup>121-123</sup> into the LESLIE3D code. This formulation requires proper discretization of the near-surface domain and classifying the various species as “gas phase,” “surface phase” and “bulk phase” depending on their location. The gas phase comprises of the species in the gas phase, residing above the material surface. The surface phase consists of those

species at the surface of the material and the bulk phase comprises of species within the material. In Section 3 we describe the current implemented model.

At present, a baseline version of SURFACE CHEMKIN has been integrated into the LESLIE3D code and it is currently being used to simulate some classical test problems as given in the manuals. Examples include, deposition of silicon from  $\text{SiH}_4$ , GaAs from  $\text{Ga}(\text{CH}_3)_3$  and  $\text{AsH}_3$ , and  $\text{Si}_3\text{N}_4$  from  $\text{SiF}_4$  and  $\text{NH}_3$ . These are non-reacting (non-reacting in the flow, reacting at the surface) cases. Eventually, we will need to incorporate more realistic chemical physics into this model. In order to do this we will be working with our collaborators in this project from **Kuo** at PSU and **Hanagud** at GaTech, to identify the key species and surface chemical process (and rates).

#### *10.1.2 Effect of wall shear forces (both tangential and normal) on the erosion process*

This model is denoted a micro-scale dynamic (MSD) model<sup>124-127</sup>. This model is based on an earlier model that was used to predict surface erosion due to particle impact. In our current effort this model has been extended to include elasticity, and enables the calculation in real time, of the surface shape of a material under prolonged shear and normal forces. We have completed this phase of development and some representative results are reported below.

#### *10.1.3 Effect of wall heat flux on the erosion process*

An extension of the model to include surface heat flux and its effect on the material properties within the MSD model is currently being developed.

#### *10.1.4 Effect of particle impact on the erosion process*

As noted above, the original MSD model was developed to account for particle impacts<sup>128</sup> so this version is already operational. How the type of particles that can impact the surface will depend on the propellant mixture. For metallized propellants, Al particles are likely to impact the surface.

#### *10.1.5 Effect of particle melt layer on the erosion process*

This effect is primarily applicable to metallized propellants with embedded Al particles. It has been suggested (**Kuo** at **PSU**, private communication) that when hot Al particles impact on the nozzle surface, a molten  $\text{Al}_2\text{O}_3/\text{Al}$  layer could form, which could cover a good portion of the convergent section of the rocket. When an  $\text{Al}_2\text{O}_3/\text{Al}$  particle entrained in the gaseous combustion products hit the wall of the rocket nozzle, it will first hit the liquid layer which can absorb a lot of the impact energy. The existence of this liquid layer has not been considered in the current model but will be addressed in the coming year.

In the following two sections we describe briefly the key features for surface kinetics and erosion modeling that is being integrated into the code.

## 10.2 Modeling of Surface Kinetics

The SURFACE CHEMKIN approach is adopted here. This approach was developed by researchers at the Sandia National Laboratories to model surface chemical reactions. This formulation uses chemical kinetics to simulate the chemical reactions between different species. This in turn enables the estimation of the deposition of different species on the surface of the material. In this formulation, three types of species are considered: gas phase (g), surface (s) and bulk (b). Chemical reactions at the surface are considered in the formulation to relate the different species taking part in the surface chemical reactions. Different types of surface sites and different types of bulk species can exist in the formulation.

Arbitrary number of gas phase species can be included but the exact number will be limited due to computational cost limitations and the need for the particular problem. Each surface species occupies a surface “site.” It is assumed that the total number of these surface sites per unit area is conserved. There can be any number of these surface sites. The surface species are monitored based on surface molar concentrations. The material comprises of different bulk phases, as mentioned earlier. The total number of bulk phases to be included depends upon the material properties and kinetics that needs to be monitored.

The current implementation is made consistent with the approach used in SURFACE CHEMKIN so that we can use the methodology in that approach for our simulations as well. At this time, the exact choice of the gas, surface and bulk species relevant for the nozzle erosion studies have not yet been finalized but is expected to be determined in the next quarter.

## 10.3 Micro Scale Dynamic (MSD) Model

The MSDM approach was developed by investigators at the University of Alberta, Canada,<sup>124-127</sup> to study the effect of wear of a material due to particle impact. However, for the present application, this model has been extended to study erosion due to shear and normal forces and the effect of heat transfer to the walls.

This model involves the discretization of the target material and mapping them onto a lattice. Each site of the lattice represents a small fictitious volume of the material. During the erosion process, any lattice site is vulnerable to movement due to the action of the external forces caused by the surface shear and normal loads, as well as due to interactions of any pair of adjacent sites. Each pair of adjacent sites is linked by an imaginary “bond.” This bond should not be mistaken for a bond between a pair of atoms, but as a hypothetical bond for the purpose of modeling. The deformation of this imaginary bond is responsible for the interactions between any pair of adjacent sites. This deformation is, in turn, dependent on the mechanical properties of the material. Any bond between two adjacent sites will break if the mechanical strain caused in the bond due to

its deformation exceeds the fracture strain of the material. Any site or a group of sites is liable to get eroded away if all the bonds surrounding it break due to fracture.

First, the target material is discretized into a lattice. At the initial instant of time, there is no site-site interaction. Due to surface shear and normal loads, the sites at the top of the material can get displaced. This displacement can cause their immediate neighbors to also get displaced. This process is carried on to other sites all throughout the material, thereby resulting in wear in the material. The total force on any particular site is due to the external force, as well as due to interaction between any pair of adjacent sites. For homogeneous materials, the force of interaction between a pair of adjacent sites can be expressed as:

$$f = k\Delta l \quad (18)$$

where  $k$  is a force coefficient, which is dependent on the Young's modulus ( $E$ ), yield strength ( $\sigma_y$ ) and tensile strength ( $\sigma_T$ ). Here,  $\Delta l$  represents the deformation of a bond between a pair of adjacent sites. The value of  $k$  depends on whether the current strain in the bond is in the elastic or plastic region. The stress strain curve of any solid homogeneous material indicating the elastic and plastic regions is shown in **Fig. 37**. The elastic region is linear by Hooke's law while the plastic region is approximated to be linear in the present model (this approximation can be relaxed later). The value of  $k$  is equal to  $E_e l_0$ , where  $E_e$  is the elastic modulus and  $l_0$  is the initial bond length under undeformed state. In the plastic region, the value of  $k$  is given by  $E_p l_0$  where  $E_p$  is the stress to strain ratio in the plastic region as shown in **Fig. 37**. The value of  $E_p$  is equal to  $(\sigma_T - \sigma_y)/(\varepsilon_T - \varepsilon_y)$ , where  $\varepsilon$  denotes the corresponding strains. The material is assumed to be isotropic at present, and therefore the orientation of the deformed bond does not change the value of  $k$ , and hence the magnitude of the bond force. The total force on any site (e.g. site  $p$ ) on the surface of the material is given by:

$$F_p = \sum_q^n k\Delta l(p, q) + f_p \quad (19)$$

where  $n$  is the number of sites  $q$  adjacent to site  $p$  and  $f_p$  is the external force as a result of surface shear and normal stresses. The value of  $n$  depends on the location of the site  $p$ .

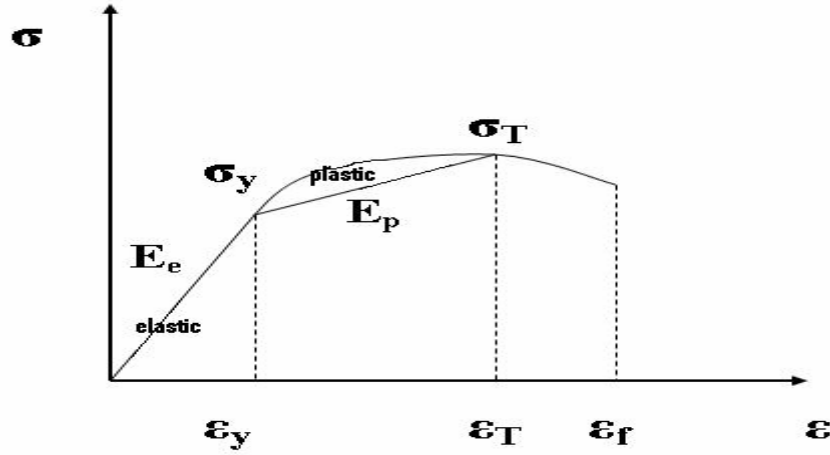


**Figure 37.** Stress-strain curve

For example, in 2D, if  $p$  is an interior point then  $n=4$ . If it is an edge point then  $n=3$  and if it is a corner point  $n=2$ .

The  $x$ -displacement can also cause a  $y$ -force on a site and vice versa. This is accounted by the Poisson's ratio,  $\nu$ . The deformation vector of the bond between any two adjacent sites  $p$  and  $q$  is given by:

$$\Delta l(p,q) = l(p,q) - l_0(p,q) = [r(q) - r(p)] - l_0(p,q) \quad (20)$$

The term  $f_p$  exists only for a site on the top surface of the material in direct contact with the impacting particle. Thus, knowing the force on a site at time  $t$ , the velocity and position of the site at a time  $t+\Delta t$  can be determined from the following equations:

$$V_{t+\Delta t}(p) = V_t(p) + \frac{1}{m} F_t(p)\Delta t \quad (21)$$

$$r_{t+\Delta t}(p) = r_t(p) + V_t(p)\Delta t \quad (22)$$

Thus, using the above equations, the velocities and positions of each site can be predicted for different time steps from which the force can be calculated. The mechanical strain caused in any bond can be denoted by:

$$\varepsilon = \Delta l/l_0 \quad (23)$$

If the strain is less than the elastic limit  $\varepsilon_y$ , the displacement of a site is recoverable. If the strain is within the plastic limit ( $\varepsilon_y < \varepsilon < \varepsilon_T$ ), a plastic deformation occurs to the bond, resulting in a permanent displacement even upon removal of the external load.

Under these circumstances, the length of the stress-free bond ( $l_0$ ) changes to a different value given by:

$$l_o^* = l_o(1 + \Delta\epsilon_p) \quad (24)$$

where the residual strain is given by:

$$\Delta\epsilon_p = \Delta l/l_o - \epsilon_y \quad (25)$$

As mentioned earlier, if the strain  $\epsilon$  exceeds the fracture strain  $\epsilon_f$ , the bond will break. Erosion of a site or a group of sites is caused when all the bonds surrounding it are broken. Upon transferring the forces from the impacting particle to the material sites, the velocities and positions of the sites can be calculated at the next time step and this procedure is repeated, thus simulating wear of the material due to particle impact.

Tungsten is used in the construction of several solid rocket nozzles as it has the highest melting point (3,683K) amongst metals and is relatively more resistant to oxidation. Hence of particular interest in the present research is the erosion behavior of tungsten. For reference, we also simulated the erosion behavior of copper although it is not directly relevant. Some of the basic mechanical properties of tungsten and Copper are shown in **Table 14**.

**Table 14.** Mechanical properties of Tungsten and Copper

Material	Tensile modulus (GPa)	Tensile strength (MPa)	Yield strength (MPa)	Poisson's ratio
Tungsten	411	1920	550	0.28
Copper	110	200	69	0.28

From the surface heat flux and wall temperature profile, the temperature profile can be obtained at all the sites of the material by solving the heat equation. The above mentioned mechanical properties of the material change with temperature and the incorporation of this effect would also include the effect of heat transfer in the simulation of erosion in the solid rocket nozzle. The MSDM is in the process of development and validation at this stage. Once fully validated, it will be integrated within the LESLIE3D code as subgrid model for surface processes. Coupling with the fluid solver will involve accounting for not only the thermo-chemical processes but also for subgrid turbulence effects. These issues are currently being formulated.

## 10.4 Results and Discussion

In the following sections we report some the key results obtained so far.

### *10.4.1 Simulation of Choked Nozzle Flow*

We employ the LESLIE3D code to simulate the gas phase flow in a two-dimensional nozzle. Hot combustion products are allowed to flow through the nozzle and the nozzle is allowed to naturally choke. The initial goal is to determine the how the wall heat flux and surface forces vary along the choked nozzle. The current simulation employs a representative rocket nozzle and is limited to 2D; however future simulations



will focus on two specific nozzle configurations: (a) the PSU rocket motor that is being used for high pressure studies and (b) the Georgia Tech nozzle design that is being built to investigate surface erosion process. We plan to use the exact dimensions from these two setups and also simulate all combustion-flow process in full 3D.

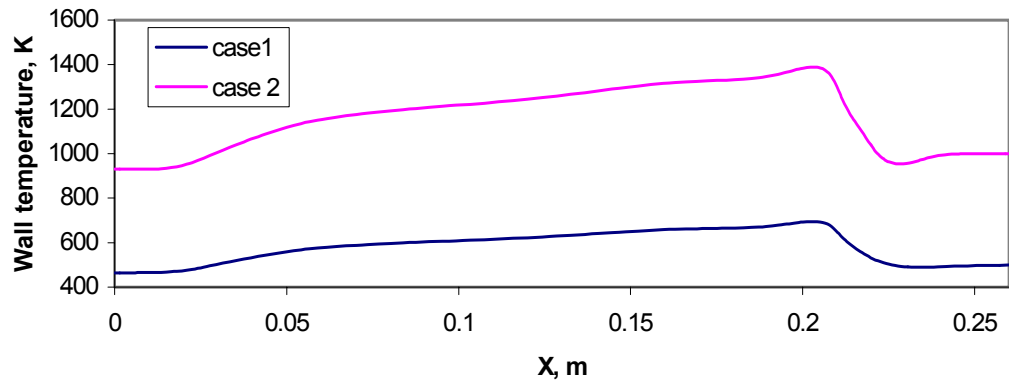
The current configuration consists of a 2D duct with a convergent-divergent nozzle attached to the duct. The total length is 0.26 m with the nozzle throat at approximately 0.206 m. The width at the inlet is 0.08 m and the throat is 0.0268 m. Different exit areas for the supersonic outflow were investigated earlier. Since we are doing fully viscous calculations the wall boundary layer can separate if the nozzle divergence is poorly designed. The surface shear forces and the wall heat flux can also be affected depending on the nature of the wall boundary layer.

A 121 x 121 grid is used with grid clustering near the walls to resolve the wall region. No-slip, isothermal condition is applied at the nozzle walls. A mixture of CO<sub>2</sub> and H<sub>2</sub>O is considered for the computations, although such a mixture is not considered realistic for solid propellant burned products. A calorically perfect gas model is assumed for the present computations, however thermally perfect and real gas simulations are also planned for later computations. The initial velocity was assumed to be 200 m/s and axial. The inlet temperature and pressure were assumed to be 2500K and 50 bar pressure respectively. The inflow is modeled using subsonic characteristic conditions while the outflow being supersonic is extrapolated.

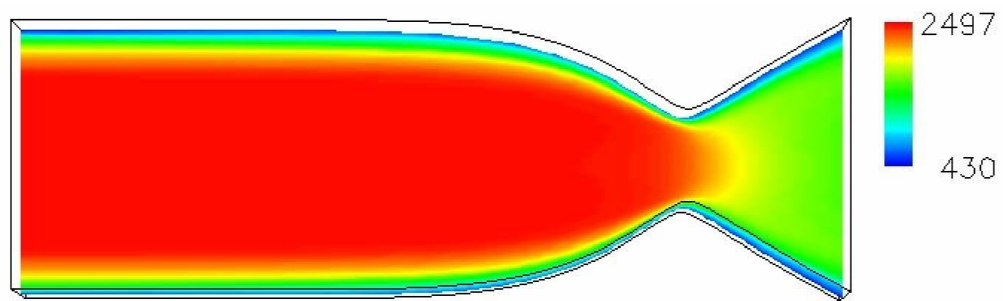
The wall isothermal profiles used here are shown in **Fig. 38 (a)**. Two simulations were conducted using different wall temperature profiles. The profile for Case 1 was chosen from an experimental study of LOX-GH2 high pressure combustion in a rocket motor. The wall temperature was quite low since external cooling was carried out. In Case 2, the wall temperature of Case 1 is doubled all along the wall. Future studies will simulate more realistic solid propellant combustion in the chamber with proper wall temperature profiles, and the MSD model will be coupled within the solver so that more realistic motors and their nozzle performance can be studied.

Some typical results are reported here. The temperature contours are shown in **Fig. 38 (b)** and **(c)** for the Case 1 and Case 2, respectively. As evident from the contour, the temperature is found to decrease in the axial direction due to the expansion of the gas downstream of the throat. The temperature magnitude in the core flow is higher for the Case 2, due to the higher wall temperature.

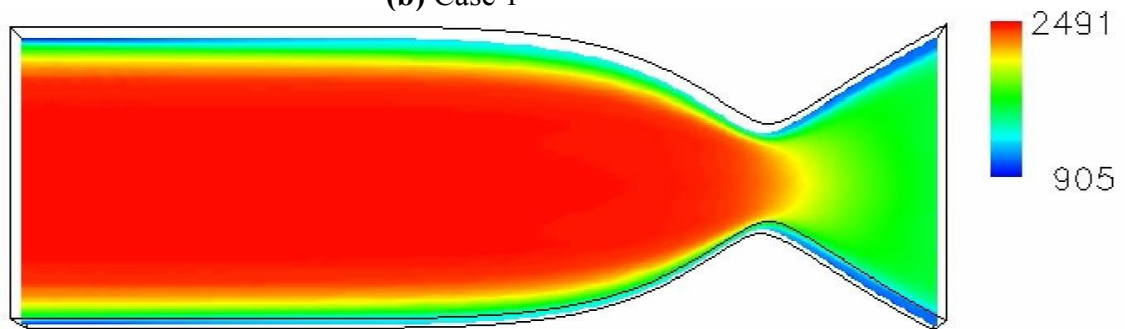
Some other representative results are shown as well. The pressure contours for Case 1 are shown in **Fig. 39**. It is clearly observable that the pressure is nearly constant in the normal directions far away from the throat, but changes significantly at the throat. The corresponding velocity contours are shown in **Fig. 40**. The U velocity is symmetric about the centerline and the V velocity profile is anti-symmetric, as expected.



(a) Wall temperature (K)



(b) Case 1



(c) Case 2

**Figure 38.** Calculated Temperature contours (K).

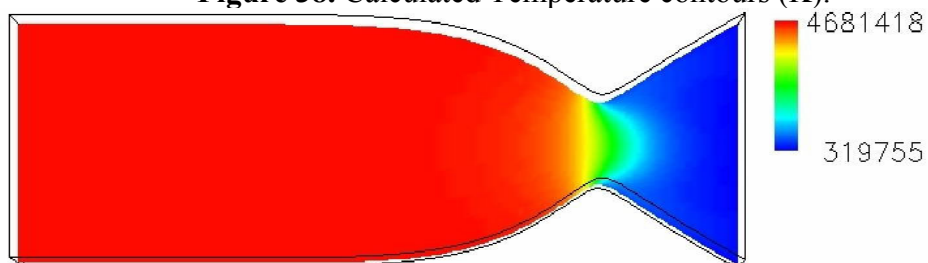


**Figure 39.** Calculated Pressure contours (Pa)

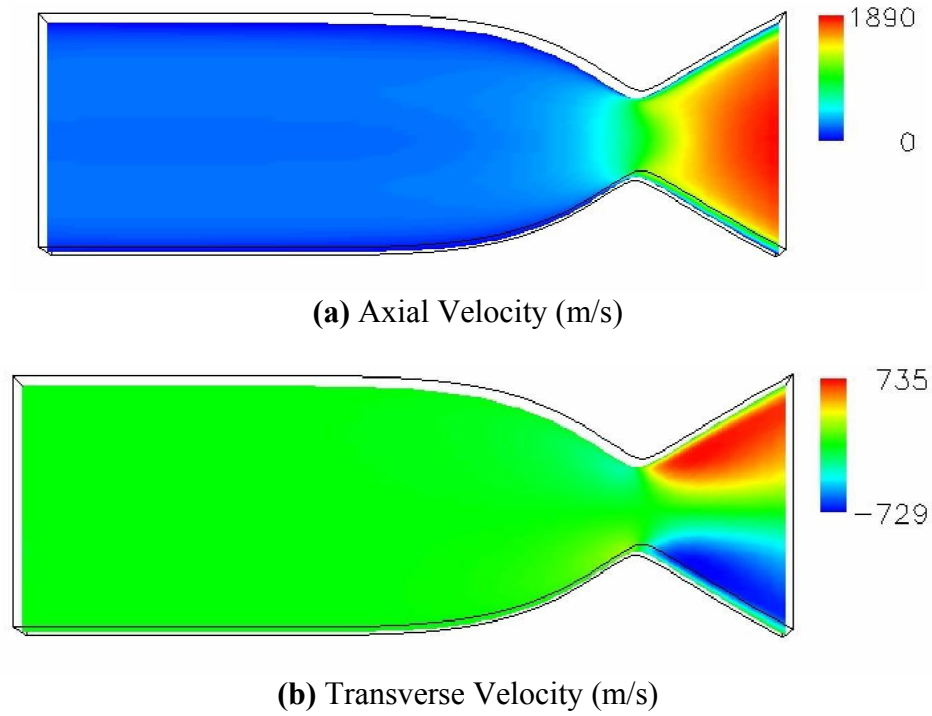


**Figure 40.** Calculated velocity contours in the nozzle

The wall shear stress profile is shown for the two cases 1 and 2 along the axial direction are shown in **Fig. 41**. As expected, the profile is found to peak at the throat. The Case 2 with the hotter wall shows a much larger shear stress.

In the next section, we use this shear stress information to simulate the surface erosion process by extending the MSD model to deal with surface force.

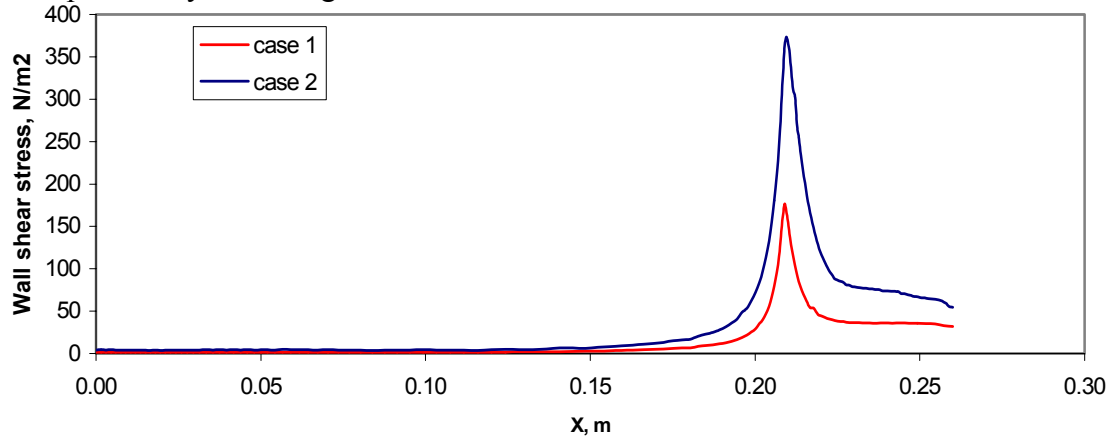


**Figure 41.** Calculated wall shear stress profile

#### 10.4.2 MSD Model Simulations

The MSD formulation was simulated to study the effect on erosion due to normal and shear forces. The normal and shear stresses were assumed to have the shear stress profile of the rocket nozzle simulated case, as shown in **Fig. 41**. For demonstration purpose, we use the Case 1 values. From these stresses, the normal and shear forces are computed and imposed on the MSD model. Tungsten and copper were considered for the material properties.

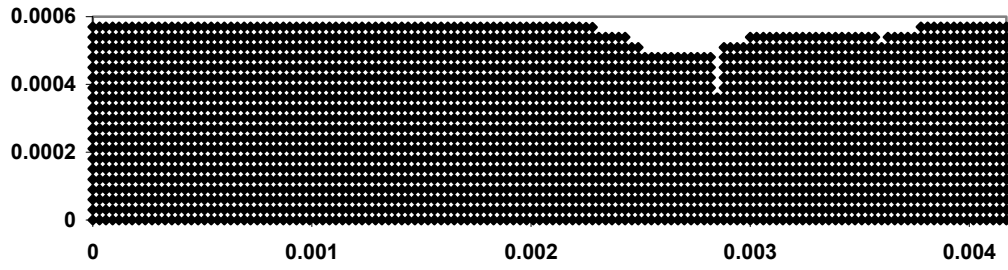
To demonstrate the effect of surface forces, we do some sample simulations that are not considered realistic for rocket cases since thermal boundary layer, surface kinetics and viscous boundary layer effects are not included. Furthermore, the MSD model is not fully coupled to the LES and therefore, the effect of erosion on the flow dynamics is currently ignored. However, the present study serves to demonstrate the MSD model and its potential for simulating surface erosion. Future studies will address the issue of full coupling between the MSD model and the flow physics.

The effect on erosion due to the chosen surface force profile is shown in **Fig. 42** for tungsten and **Fig. 43** for copper. A material block of 6mm x 0.4mm dimension is simulated with the above mentioned forces. An initial bond length ( $l_0$ ) of  $3e-5$  m and a time interval of  $2.5e-7$  sec were used for 100 time steps. The process of erosion as a function of time is shown in both these figures. Tungsten was observed to experience more erosion loss than copper for the same applied loading. From the figures it is evident that tungsten surface profile distortions are wider than copper, which has relatively more concentrated surface wear. These results are summarized in **Table 15**. Vertical erosion is computed from the depth of the eroded region as a fraction of the total depth. Horizontal erosion is computed from the horizontal width of the computed region as a fraction of the total width. Since many of the realistic physics have not yet been included these estimates are not considered accurate at present. Nevertheless, the current results show that the MSD model is capable of capturing some of key physics of erosion.

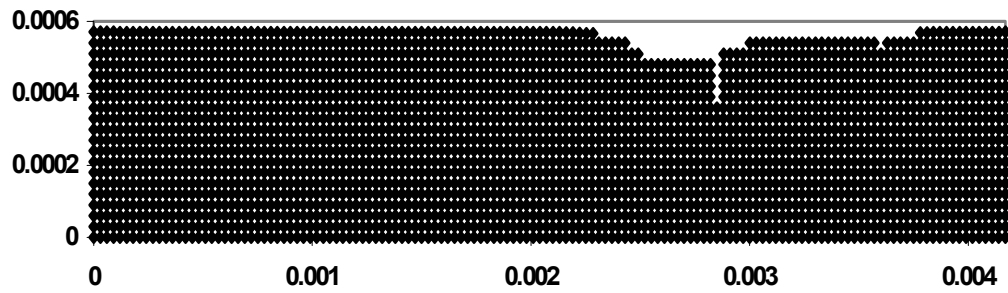
**Table 15.** Estimate of erosion from MSD simulations for effect of surface forces

Material	% of vertical erosion	% of horizontal erosion
Tungsten	15	35.7
Copper	20	14.3

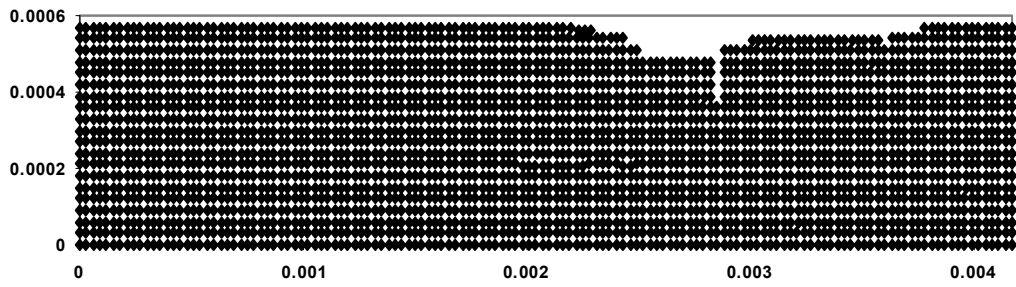
As observed in **Table 15**, tungsten encountered more lateral erosion, while copper encountered more vertical erosion in depth. This phenomenon is as expected. The relatively more ductile copper has a higher resistance to surface loads owing to its better capability to accommodate plastic deformation. On the other hand, the relatively more brittle tungsten makes it more vulnerable to deformation.



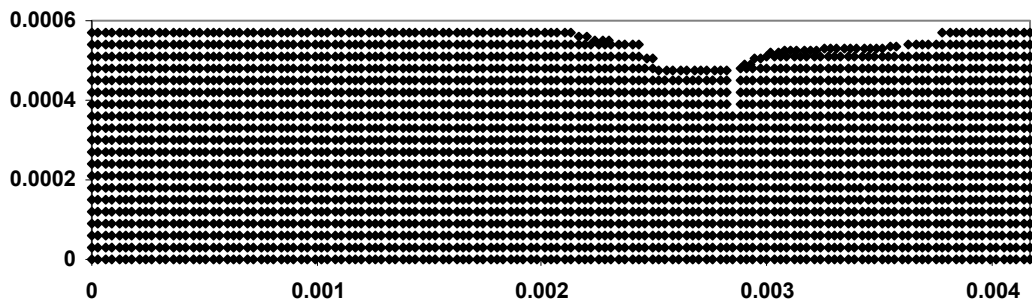
(a)



(b)

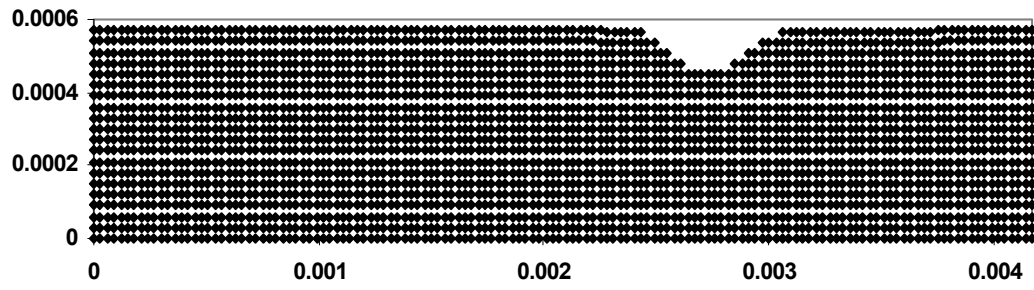


(c)

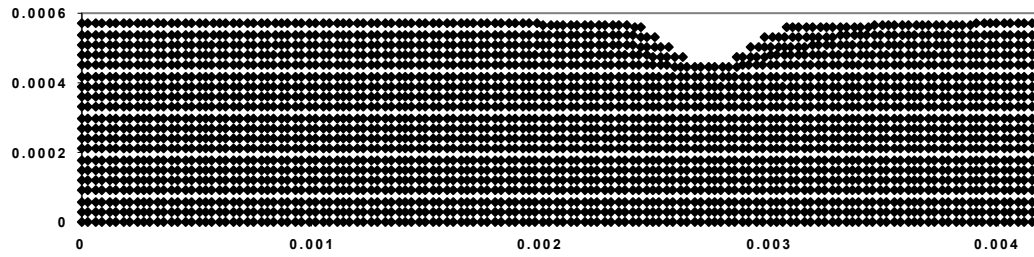


(d)

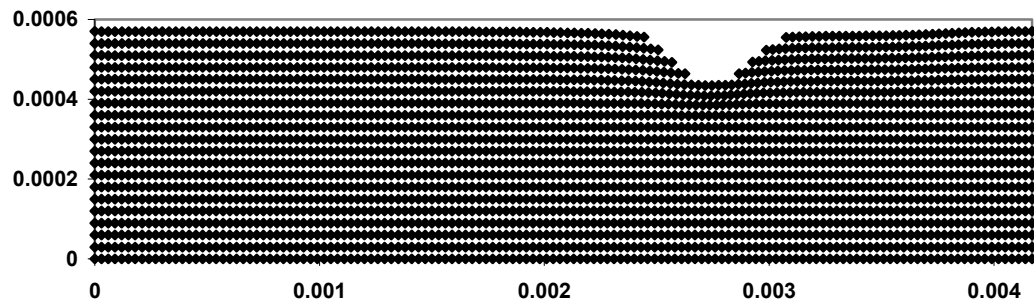
**Figure 42.** Erosion due to shear and normal forces for Tungsten; (a) 6.25  $\mu\text{sec}$ , (b) 12.5  $\mu\text{sec}$ , (c) 18.75  $\mu\text{sec}$ , (d) 25  $\mu\text{sec}$  (all axes in m)



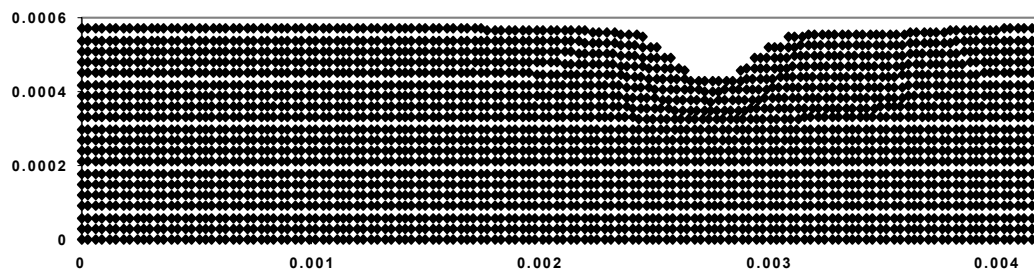
(a)



(b)



(c)



(d)

**Figure 43.** Erosion due to shear and normal forces for Copper; (a) 6.25  $\mu\text{sec}$ , (b) 12.5  $\mu\text{sec}$ , (c) 18.75  $\mu\text{sec}$ , (d) 25  $\mu\text{sec}$  (all axes in m).

It is also important to point out the erosion effect is directly related to the choice of  $\Delta t$ . If  $\Delta t$  is too large, the bond deformation could be large enough to easily cause excessive erosion, which is not correct. **Fig. 44** shows the erosion results of tungsten for (a)  $\Delta t = 0.1 \mu\text{sec}$  and (b)  $\Delta t = 0.05 \mu\text{sec}$ , with both cases run for a total time of  $100 \mu\text{sec}$ . The shear stress profile of case 2 was considered for these computations and a larger sample size was simulated. As evident from the figure, the choice of a smaller  $\Delta t$  results in more erosion. The correct choice of  $\Delta t$  is related to the value of the stress free bond length ( $l_0$ ) and their quantitative relationship needs to be further investigated. The time step will also be constrained by other surface effects, such as heat flux, boundary layer, and melt layer. This issue needs to be further investigated and will be addressed in the next quarter.

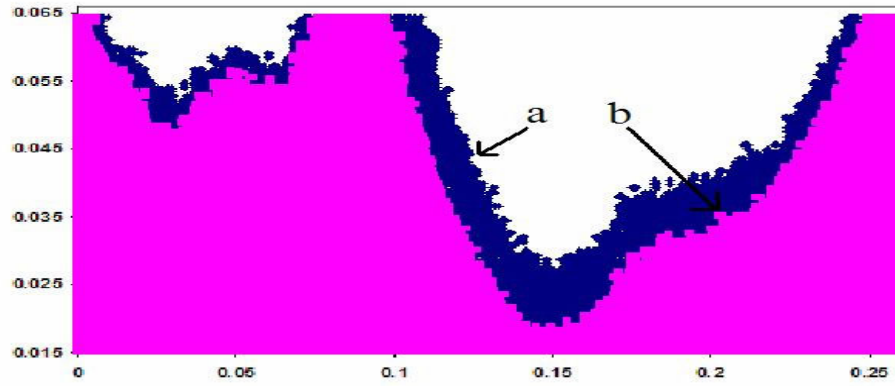
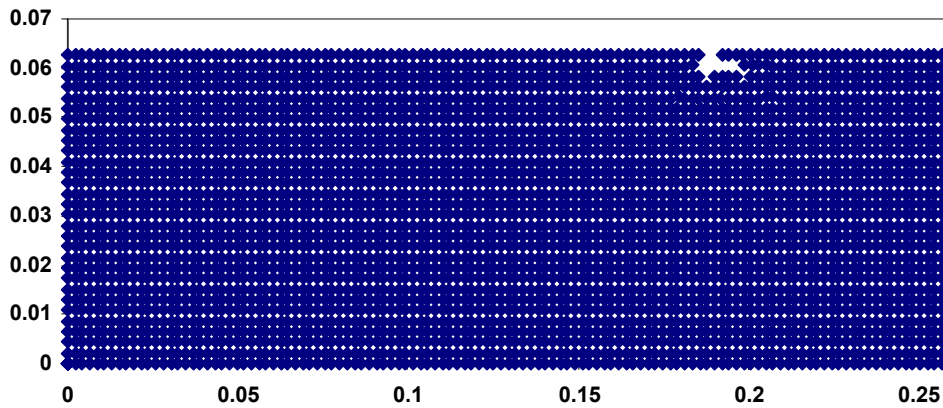
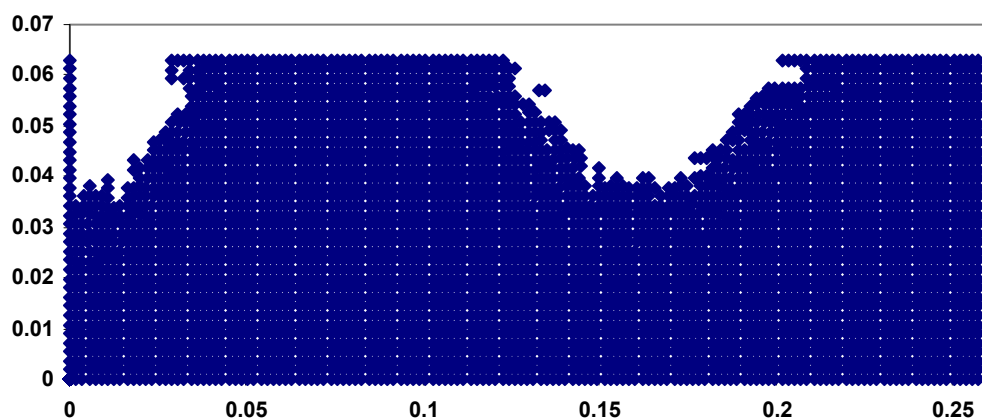


**Figure 44.** Effect of choice of  $\Delta t$  on erosion (total time =  $100 \mu\text{sec}$ );  
(a)  $\Delta t = 0.1 \mu\text{sec}$ , (b)  $\Delta t = 0.05 \mu\text{sec}$  (all axes in m)

The effect of the hotter isothermal wall on erosion was also studied. **Figure 45** shows the erosion caused on a block of tungsten for the two different wall temperatures (Case 1 and 2). For this study, computations were carried out for  $60 \mu\text{sec}$ , in time steps of  $0.04 \mu\text{sec}$ . The hotter wall had a higher shear stress and therefore higher erosion was observed.



(a)



(b)

**Figure 45.** Effect of wall temperature on erosion; (a) case 1, (b) case 2.

Future studies are planned to incorporate the MSD along with the actual nozzle flow simulation in order to simulate the real rocket erosion environment. Studies are planned to be extended to thermally perfect and real gas simulations. These studies are expected to develop a complete analysis of solid rocket nozzle erosion and ascertain the major factors that govern the process.

## **11. Phase diagrams and diffusion mechanisms in consideration of the oxidation, carburization and nitration of bulk metals (Morral Group at OSU)**

An extensive literature survey was performed. Information about the Rocket Nozzle Material selection and basic knowledge about their high temperature properties (including high temperature strength, high temperature oxidation-corrosion resistance and high temperature ablation resistance) were collected with the focus on metal based materials and various composite materials. Currently the focus of the literature survey is carbon/carbon composites and tungsten powder materials. In this regard we are preparing thermodynamic and kinetic databases for tungsten-rich W-Cu-C-Cl-H-N-O systems. In addition we are continuing our studies of oxidation and other damage mechanisms of carbon/carbon composites.

A thermodynamic database for the W-Cu-C-CL-H-N-O System was prepared from existing data<sup>129</sup>. From this database, a number of phase diagrams were constructed using Thermo-Calc software<sup>130</sup> for W under various gas atmospheres as shown below.

### 11.1 W-O-C-H Phase and Stability Diagrams

The W-O diagrams in **Fig. 46** map the equilibrium phases as a function of temperature and mole fraction of oxygen on the left and as a function of temperature and natural log of oxygen activity on the right. The two W-C-O diagrams in **Fig. 47** map the



equilibrium phases at 2,000 K as a function of the natural log of carbon monoxide activity and the natural log of diatomic oxygen activity on the left and as a function of the natural log of carbon monoxide activity and carbon dioxide activity on the right. **Fig. 48** is similar except it is for the W-H-O system.

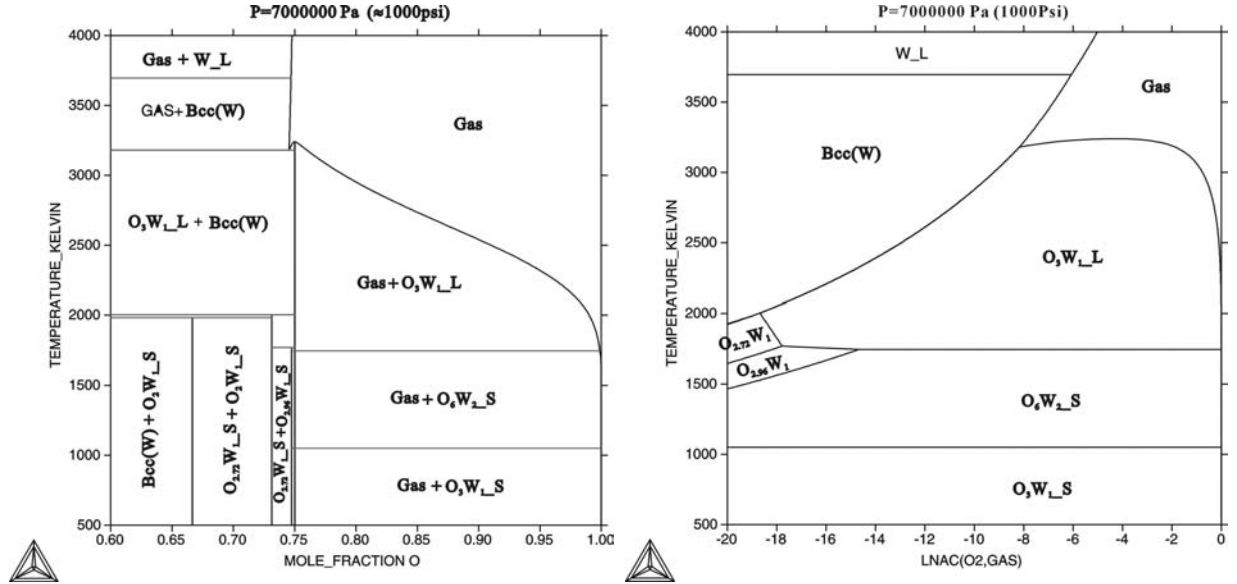


**Figure 46.** The W-O phase diagram at 1000 psi total gas pressure as a function of temperature and mole fraction of oxygen on the left and as a function of temperature and natural log of oxygen activity, LNAC(O<sub>2</sub>, GAS), on the right. The gas phase in the figures contains oxygen as well as various tungsten oxide molecules.

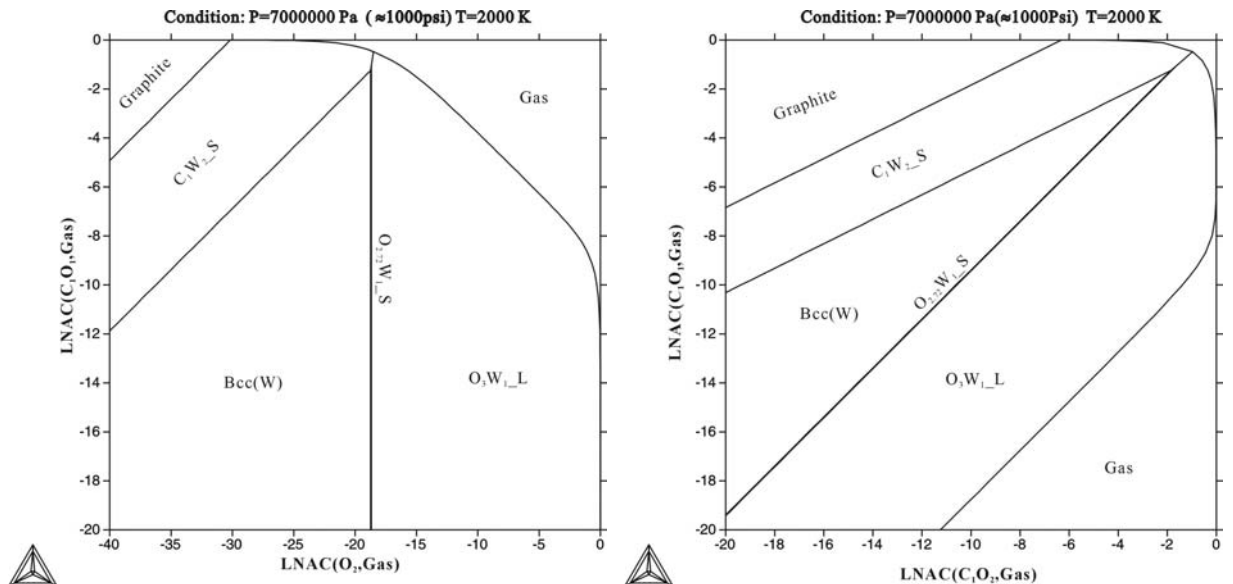


**Figure 47.** The W-C-O phase diagram at 1,000 psi total pressure and 2,000 K and as a function of the natural log of the carbon monoxide activity, LNAC(CO, Gas), and the natural log of diatomic oxygen activity, LNAC(O<sub>2</sub>, Gas), on the left and as a function of the natural log of carbon monoxide activity, LNAC(CO, Gas), and carbon dioxide

activity,  $\text{LNAC}(\text{CO}_2, \text{Gas})$ , on the right. The gas phase in the figures contains oxygen, as well as various carbon oxide and tungsten oxide molecules.

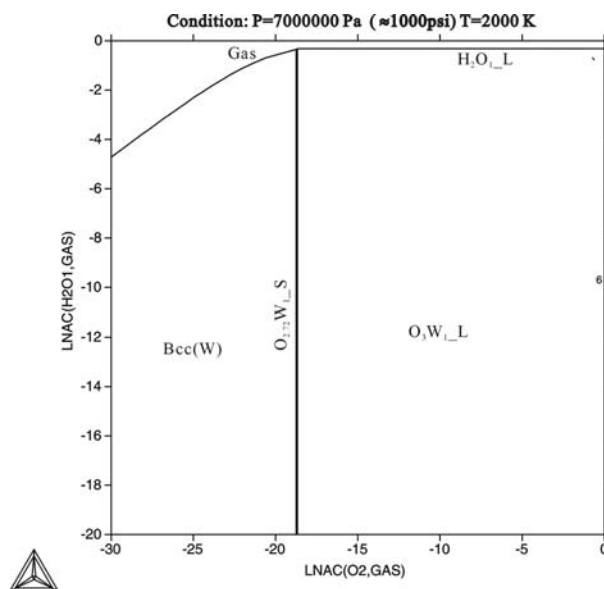


**Figure 48.** The W-H-O phase diagram at 1000 psi and 2000 K as a function the natural natural log of the water vapor activity,  $\text{LNAC}(\text{H}_2\text{O}, \text{Gas})$ , and the natural log of the oxygen gas activity,  $\text{LNAC}(\text{O}_2, \text{Gas})$ . The gas phase in the figures contains oxygen, hydrogen, water vapor as well as various tungsten oxide molecules.

## 11.2 W-CL-H-O stability diagrams

The reaction of pure tungsten (W) with gas containing chlorine (Cl) is illustrated below by a series of temperature versus natural log activity and natural log activity versus natural log activity diagrams. **Figure 49** shows W can be attacked by Cl, but that a greater activity of Cl is needed to cause a reaction as the temperature increases. This behavior is expected for exothermic reactions. The figures on the left and right show that increasing the pressure from 14.7 to 1,000 psi reduces the chlorine activity needed to cause a reaction by about a factor of seven. Therefore the stability of W to forming volatile chlorides is decreased by either decreasing the temperature or increasing the gas pressure.

Another way that W can be stabilized is by increasing the hydrogen activity as shown in **Fig. 50**, which is a stability diagram for the W-Cl-H system at a temperature of 2,000 K and 1,000 psi as a function of the chlorine and hydrogen activities. Stability diagrams for the W-Cl-O system are given in **Fig. 51** at both 2,000 K and 3,500 K. The diagrams show that at the higher temperature the tungsten oxides are volatile and that the stability of W has increased against reactions with both Cl and  $\text{O}_2$ . This increasing stability with temperature is the same effect illustrated in **Fig. 49**.

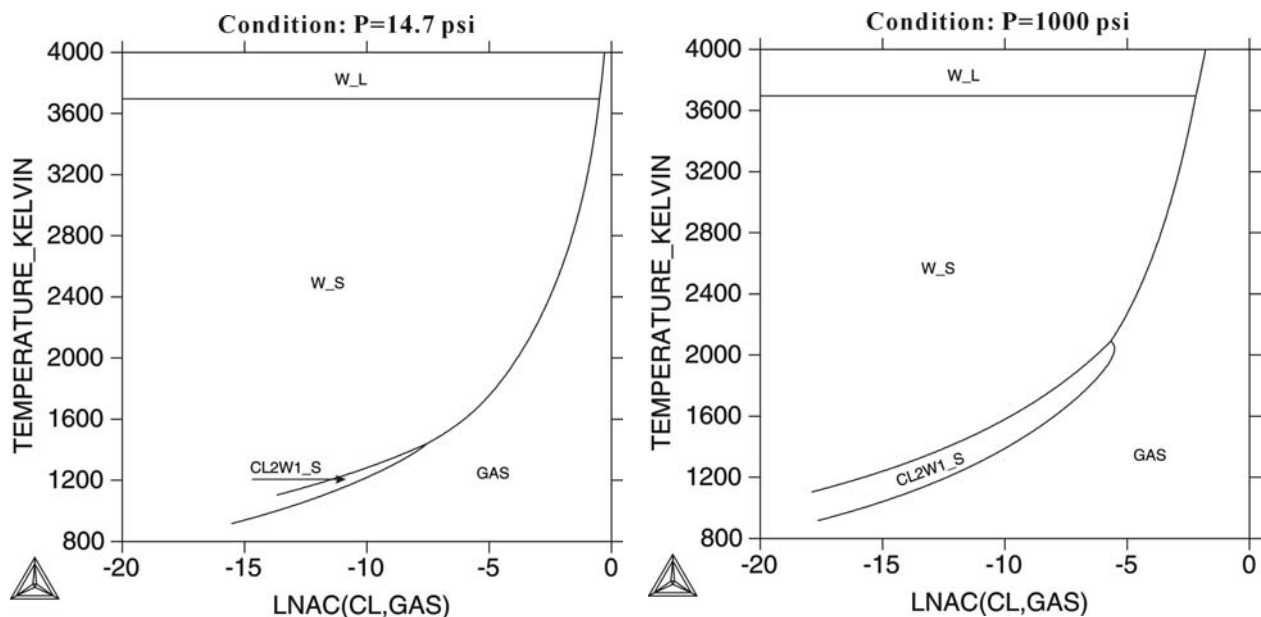


**Figure 49:** The W-Cl stability diagram as a function of temperature and CL activity at 14.7 psi on the left and 1,000 psi on the right. The gas phase contains chlorine and various tungsten chloride molecules.

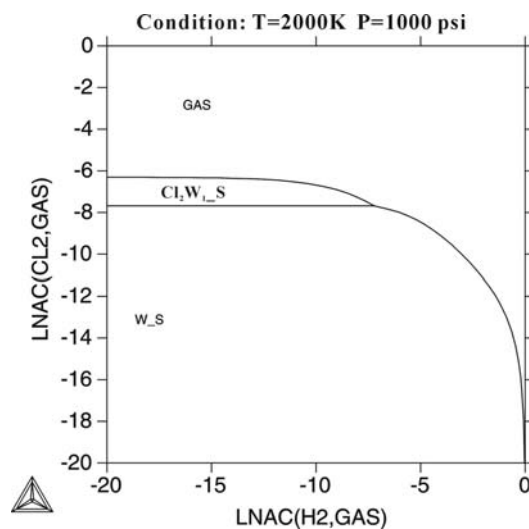


**Figure 50.** The W-Cl-H stability diagram at 2000 K and 1000 psi as a function of the natural log of the CL activity,  $\text{LNAC}(\text{CL}_2, \text{Gas})$  and the natural log of the hydrogen activity,  $\text{LNAC}(\text{H}_2, \text{Gas})$ . The gas phase contains hydrogen, chlorine, hydrochloric acid vapor and various tungsten chloride molecules.

In **Fig. 52** several sections of the W-Cl-C-H-O stability diagram at 2,000 K and 1,000 psi are given. They illustrate the ability of the software to make predictions even when dealing with complex gas mixtures. In the investigation of nozzle erosion it will be possible to input measured or predicted gas compositions and predict how the relative stability of W is affected. It is possible that the nozzle material will be tungsten powder

impregnated with Cu. Calculations were made of the Cu solubility in W as a function of both temperature and powder particle size. The W-Cu database was adapted from limited information available on the W-Cu phase diagram<sup>131</sup>.

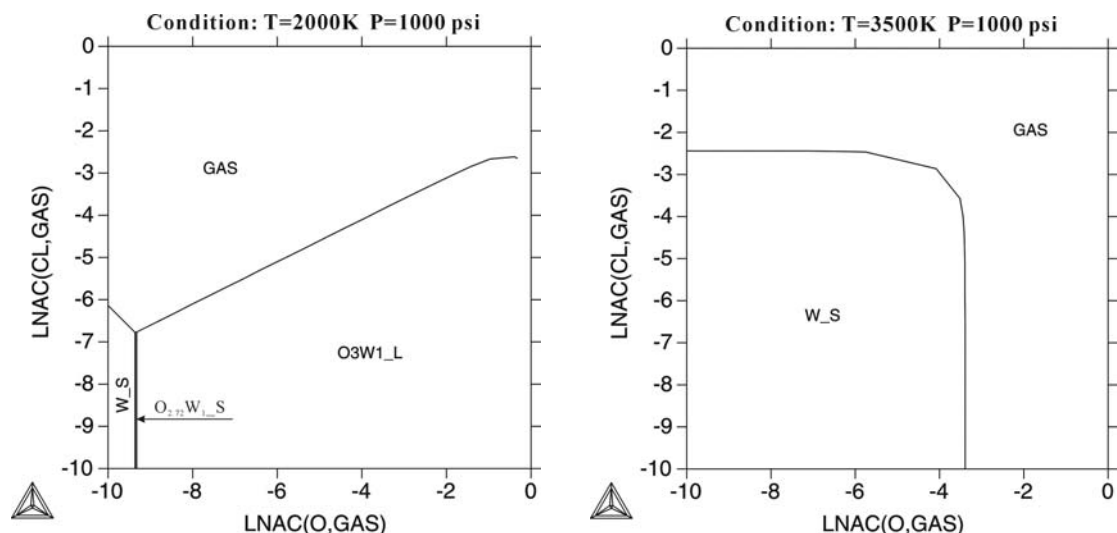


**Figure 51.** The W-Cl-O stability diagram at both 2,000 K and 3,500 K at 1000 psi as a function the natural log of Cl gas activity,  $\text{LNAC}(\text{Cl}, \text{Gas})$  and the natural log of the oxygen gas activity,  $\text{LNAC}(\text{O}_2, \text{Gas})$ . The gas phase contains oxygen and various oxychloride, tungsten oxide, and tungsten oxychloride molecules.

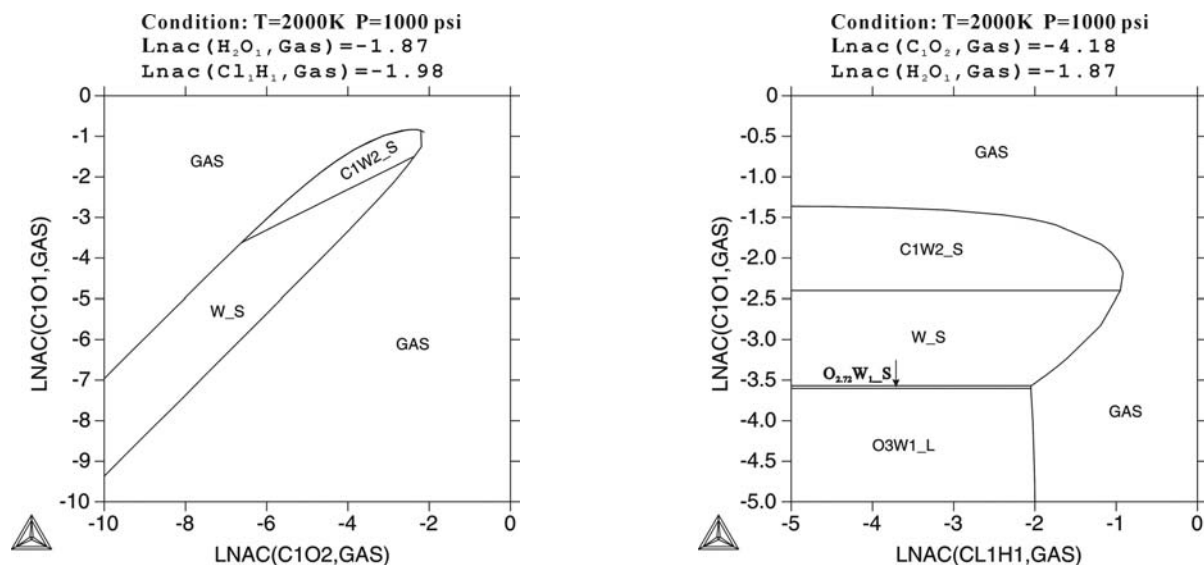


**Figure 52.** Several constant activity sections through the W-Cl-C-H-O stability diagram at 2,000 K and 1,000 psi. (The gas phase contains a wide variety of gas molecules.)

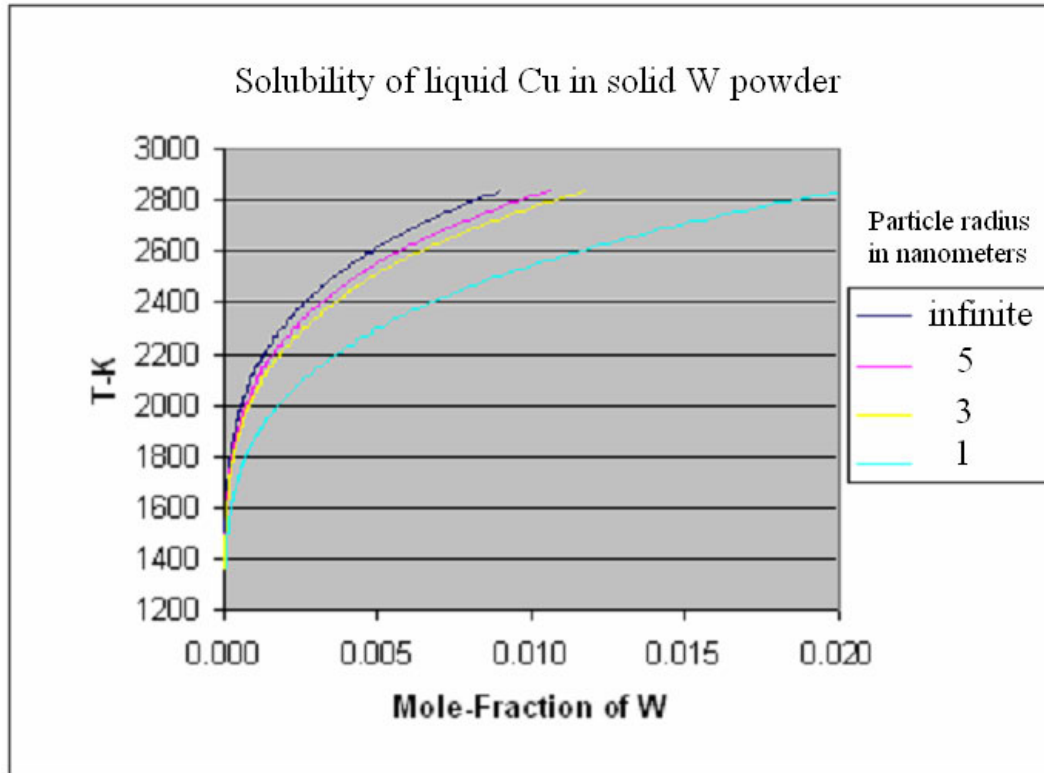
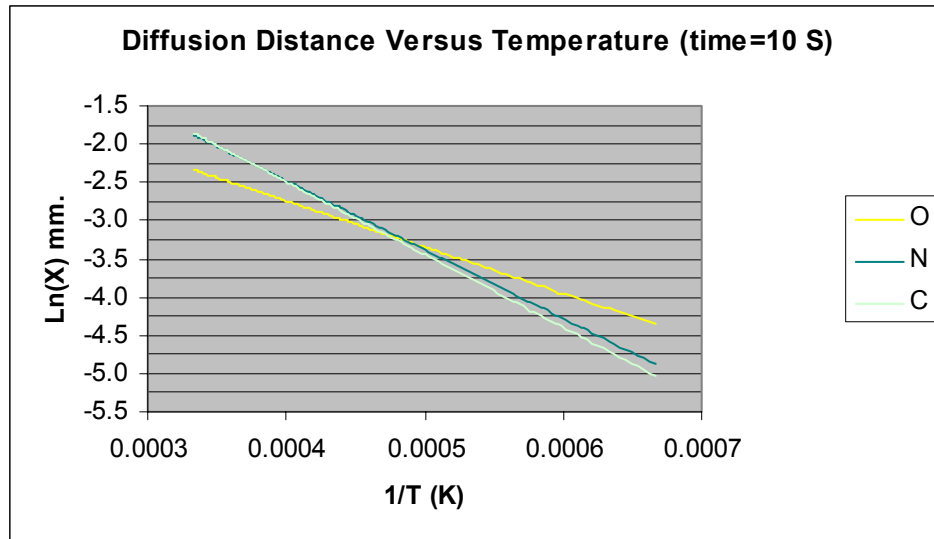


**Figure 53.** The solubility of Cu in solid W powder as a function of W particle size.

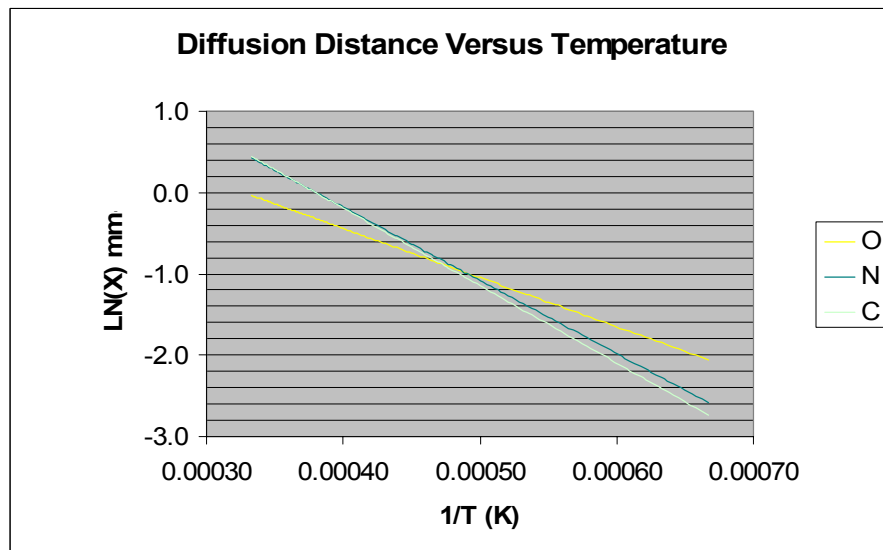
The results given in **Fig. 53** suggest that the solubility could approximately double if the powder particles were in the several nanometer size range.

### 11.3 Kinetic Database

A kinetic database for the W-Cu-C-N-O System was created from existing tracer diffusivity data<sup>132</sup>. The database assumes that the atoms move independently of interactions with other atoms when moving through the lattice (i.e. there are no cross coefficients in the diffusivity matrix). The diffusivities of the various interstitial elements coming from the gas phase; O, N and C, are compared in **Fig. 54** which gives the natural log of the diffusion distance after both 10 seconds and 1,000 seconds over a range of temperatures. The diagram shows that above 2,000 K that interstitial atoms can diffuse tens of microns in 10 seconds and nearly millimeters in 1,000 seconds. In **Fig. 55** there is a similar diagram for substitutional atoms. It predicts that after ten seconds that the penetration would be less than a micron and after 1,000 seconds it would be on the order of a few microns for most atom species.

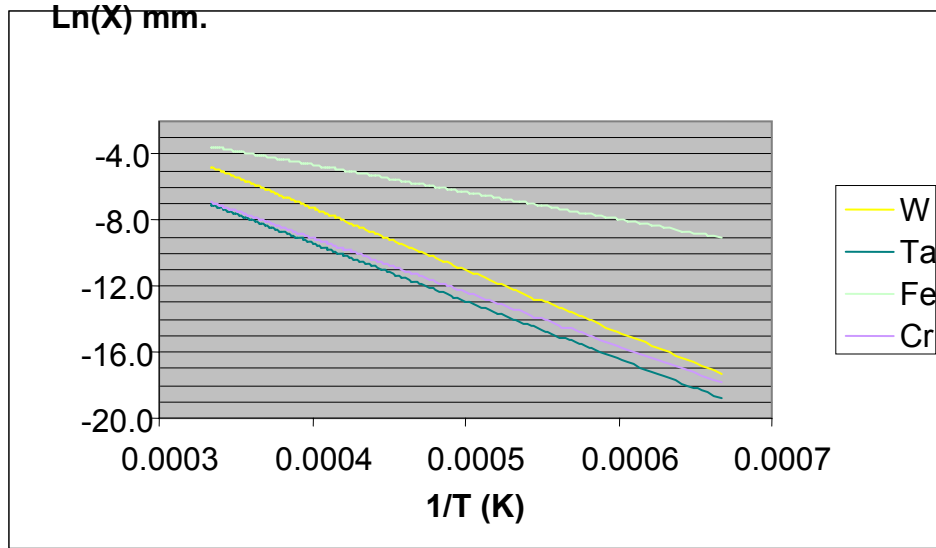


(a)

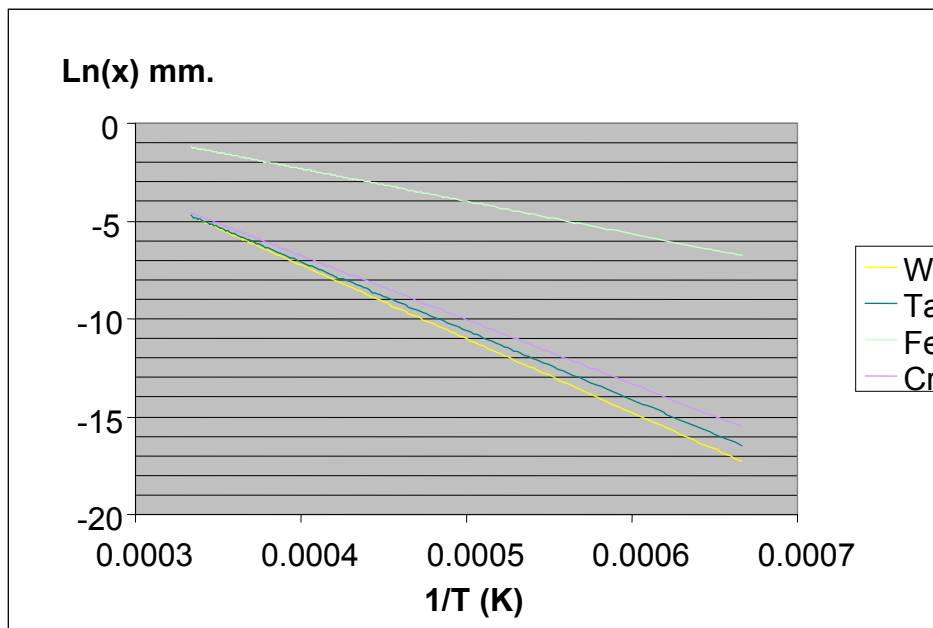


(b)

**Figure 54.** The diffusion distance of various interstitial atoms in W after (a) 10 seconds and (b) 1000 seconds



(a)



(b)

**Figure 55.** The diffusion distance in W of various substitutional atoms after (a) 10 seconds and (b) 1000 seconds as a function of temperature

## Major Accomplishments and Findings

- During the first year of the MURI-RNEM program, the **Kuo-group at PSU** has completed the design of two test rigs for evaluation of the instantaneous nozzle erosion process. The first test rig is called the rocket motor simulator (RMS), which can simulate the gaseous combustion product species of the non-metallized Propellant S as well as the product gas temperature. The RMS will utilize a vortex combustor design for injection of gaseous reactants. In the RMS, the concentrations of the product species can be varied systematically to study the effect of a given species concentration on erosion rate of nozzle throat. The second test rig designed is an instrumented ultra high-pressure solid-propellant rocket motor, which can be operated at nominal chamber pressures of up to 8,000 psia. Both the RMS and the ultra high-pressure solid-propellant rocket motor will have the capability of instantaneous nozzle erosion rate measurements by real-time X-ray radiography technique.
- Modifications to the graphite recession code (GRC) have been conducted by **Kuo-group at PSU** to incorporate the more comprehensive heterogeneous reaction kinetics proposed by Chelliah et al.<sup>10</sup> Predicted nozzle erosion results using three different sets of kinetic data of Chelliah et al.,<sup>10</sup> Libby-Blake,<sup>17</sup> and Golovina<sup>16, 36, 133</sup> were compared to show that even though the diffusion of oxidizing species to the nozzle throat surface is very important, the overall recession rate of nozzle surface also depends strongly on the heterogeneous reaction kinetics. The pressure dependency of the nozzle erosion rate was investigated and explained through the consideration of pressure effect on the local heat-transfer coefficient at the nozzle throat.
- The propellant requirement and test matrix was prepared by **Kuo and Yetter groups at PSU** with input from Dan Miller at NAWC-China Lake. The total requirement for solid propellant grains for nozzle throat erosion testing at **PSU** and **Hanagud, Seitzman, and Wilkinson group at GaTech** with the test matrix was submitted to ONR on May 11, 2005 for consideration and processing at China Lake. The test matrix of **PSU** is given in Appendices A-C. The test matrix of **GaTech** is given in Appendix D.
- The **Yetter Group at PSU** has obtained results that have important implications with regards to erosion of tungsten-based nozzles as well as to the design of fundamental kinetics experiments and oxidation mechanisms of tungsten. The results suggest that lower pressures should be able to yield the kinetics of interest to high-pressure nozzle erosion since the same speciation and relative amounts exist at lower pressures. The results also suggest which species will need to be considered in any elementary oxidation reaction mechanism to describe the chemical erosion process in environments with and without chlorine. These results show how the erosion mechanism could change from one involving purely chemical oxidation to one involving both physical and chemical mechanisms as a function of temperature, pressure, and propellant composition. *The results of the equilibrium calculations advocate for aluminized propellants in tungsten-based nozzles as tungsten oxide and tungsten oxychloride formation are significantly reduced due to the strong affinity of oxygen for aluminum.* The addition of aluminum also eliminates liquid WO<sub>3</sub> formation, which may reduce the



physical erosion mechanism. However, liquid and solid  $\text{Al}_2\text{O}_3$  are combustion products at high temperature and pressure, which may contribute to physical erosion through particle impact, and therefore, the physical erosion mechanism cannot totally be neglected.

- **Yang group at PSU** has been working on the numerical code for simulating the gas-phase flow field by extending an existing large-eddy-simulation (LES) code. This code utilizes a comprehensive numerical analysis for treating multi-component turbulent flows with gas-phase and surface reactions. Great progress in implementation and validation of this code on a parallel computing facility has been accomplished.
- **Lin, Musaev, and Irle Group at Emory** has successfully implemented and tested a three-stage strategy for the *a priori* prediction of reaction rate constants of large, complicated systems under high temperature/high pressure conditions. This strategy is novel in its combined use of a computationally cheap, yet qualitatively accurate approximate DFT method for the on-the-fly generation of energies and gradients (DFTB-D), and systematic identification of intermediate structures and reaction products at the more accurate ONIOM(DFT:DFTB-D) level of theory. Transition states between these structures will allow the calculation of overall rate constants for individual elementary nozzle erosion reaction processes of pristine and defective graphite surfaces.
- **Lin, Musaev, and Irle Group at Emory** has shown that pristine graphite surfaces are chemically inert toward normal-pressure attack of exhaust products  $\text{H}_2\text{O}$ ,  $\text{H}$ ,  $\text{CO}$ , and  $\text{CO}_2$ . This team expects that defects caused by high-temperature/high-pressure conditions will lead to more reactive surfaces sites, allowing gradual erosion to take place in a “zipper”-type mechanism. Preliminary investigations along these lines are pointing to this possibility, and the results of these simulations will greatly impact possible recommendations for the design and products of nozzle materials, which are less susceptible to erosion processes.
- According to **Lin, Musaev, and Irle Group at Emory**, water (as primary exhaust component) is easily capable of attacking and reacting with W atoms and cations through various spin-state crossings, and possibly tungsten surfaces, which are otherwise ideal candidates for nozzle material due to high melting temperature. Calculations with larger tungsten surface models are currently underway to clarify the role of the tungsten surface (bulk) environment. In addition, OH radicals were shown to readily attack even pristine graphite surfaces and form stable complexes, which can re-organize themselves and subsequently the graphite surface at energy levels feasible under the high-temperature conditions under which nozzle erosion occurs.
- **Brezinsky Group at UIC** has created a new test section of the shock tube, which has been bored, honed, electro-polished, and machined for attachment of the new particle injector. All parts of the particle injector are now complete. A replica of the test section with the particle injector has been constructed out of plexiglass. A high-speed camera has been used to film the particles injected into the plexiglass tube. With the information gathered from analyzing the resulting images, determination was made of the optimal air pressure to use when injecting particles into the shock tube.

- According to **Brezinsky Group at UIC** Carbon black powder from Cabot (Monarch® 800; density: 1.9 g/cm<sup>3</sup>, specific area: 210 m<sup>2</sup>/g, crystalline state: amorphous, C/H ratio: 99, diameter range: 20 to 100 nm) was selected instead of the baseline Metaullics G-90 graphite material for the MURI project, because it is not available in powder form. The selected powder has the same density as Metaullics G-90. An investigation of the expected reaction behavior of the selected powder revealed that at pressures above 1 bar (shock tube pressure: 550-700 bar), carbon particles with a diameter below 6 μm (with particle diameters <100 nm) undergo reaction-limited combustion as is desired. Therefore, the Cabot powder is a suitable solid source of carbon for these studies. The physical characteristics of these powders have been characterized by transmission electron microscopy.
- **Brezinsky Group at UIC** has also developed a strategy to confirm the two rate constants of interest in the Kuo and Keswani model<sup>30</sup> based on the gas phase composition in the shock tube before and after a shock wave is fired. These rate constants will be for the global reactions because it is not possible to measure the rates of adsorption and desorption reactions. Experiments have begun on the gas phase CO/CO<sub>2</sub>/H<sub>2</sub>O/H<sub>2</sub> chemistry in order to calibrate the ability of existing models to simulate the very high pressure chemistry of these species related to graphite nozzle erosion.
- With reference to the use of synchrotron X-ray technique, for the study of time dependant erosion techniques, **Hanagud, Seitzman and Wilkinson Group at GaTech** has accomplished the following items: 1) the propellant combustion chamber has been designed and is being fabricated; 2) the propellants have been selected and a test matrix has been formulated to meet the objectives; 3) the group has contacted Argonne National Laboratories for conducting tests during the second year. This team will send a formal proposal to Argonne National Laboratories during November 2005.
- Also, in preparation for the synchrotron X-ray tests and to assist the tests, **Hanagud, Wilkinson and Seitzman Group at GaTech** has initiated and completed a first phase of the study of interaction carbon monoxide with a tungsten nozzle at high pressures and high temperatures. The group has completed the first phase of *ab initio* chemisorption studies of carbon monoxide interaction with tungsten at high temperatures and high pressures. The *ab initio* results confirm the inferences and conclusions of experiments concerning the non-disassociation of carbon monoxide and bonding of carbon and oxygen atoms to the tungsten surfaces at high temperatures. Results have also been developed for high pressures and high temperatures that are not available in previous experimental work. Thus, the group has convincingly shown that the developments of *ab initio* chemical reaction studies are on solid foundation and the group can study the erosion due to other propellant decomposition products, by using *ab initio* techniques. This approach can be used to supplement the propellant combustion chamber tests, in designing the test matrix for synchrotron X-ray tests at Argonne National Laboratories. This team has also completed a manuscript on this work, for publication in a journal, and intends to submit an abstract to the JANNAF meeting in the future.
- **Hanagud, Wilkinson and Seitzman Group at GaTech** has also developed a procedure to fabricate nozzle (and evaluate in the propellant combustion chamber) that

will be made of a composite of zirconium carbide and tungsten. A motivation for this development is the higher melting temperature of zirconium carbide (3,540 °C) and thus a higher operating temperature of the nozzle, in comparison to the tungsten nozzles. The procedure was developed with the help of Dr. Ken Sandhage of the School of Materials Science and Engineering at Georgia Tech.

- Preliminary studies and computations have been carried out by **Menon Group at GaTech** to determine the various factors that govern the erosion process in a solid rocket nozzle. A new micro-scale dynamics (MSD) model has been adopted by this group to simulate the process of actual surface erosion due to surface forces and heat flux. Preliminary simulations for tungsten and copper nozzles were carried out using representative shear forces on a material sample. At this time, the sample size and surface forces employed were primarily chosen to demonstrate how the MSD model will be used. In the near future, this MSD model will be implemented within the LES code as a subgrid model to capture the fine-scale erosion process. Full two-way coupling and determination of the physical time step will be carried out. Finally, a surface CHEMKIN approach to account for surface kinetics within the LES code has been implemented but has not been coupled to the test case as yet. This coupling is expected to be completed in the next year. Future studies will also focus on investigating more realistic rocket nozzle physics than the demonstrations shown in the results obtained so far. The LES code will be used to simulate the nozzle configurations, such as the one currently being tested at **PSU** and the one being built at **GaTech** for surface erosion measurements.
- **Morral Group at OSU** has developed phase diagrams of the W-O-C-H-Cl systems to obtain insight into how tungsten reacts with high-pressure gases containing oxygen, carbon, hydrogen and chlorine. Also to demonstrate the ability of Thermo-Calc to predict the equilibrium phases under different conditions of high pressure, temperature and gas chemistry. The diagrams show, for example, the gas activity conditions when tungsten is stable to forming volatile molecules containing oxygen, chlorine, hydrogen and carbon. Also, they outline conditions when the oxides or chlorides will be solid, liquid, or vapor. These will be important considerations with regard to erosion mechanisms. However like all phase diagrams predicted from thermodynamic databases they needed to be validated with experimental data when extrapolations are made to conditions, which have not been previously investigated.
- According to **Morral Group at OSU**, it is instructive to note that when W powder is in the nanometer-size range that the solubility of Cu may be approximately double the value predicted by the equilibrium phase diagram. This could alter the high-temperature properties of W-Cu nozzles from what was found using nozzles made from conventional tungsten powder. In addition, tracer diffusivities in tungsten found in the literature predict that after 10 seconds at temperatures above 2000 K, the interstitial atoms will move tens of microns while substitutional atom movement is expected to be sub-micron. These numbers suggest depths at which compositional effects could occur during erosion.

**List of Papers Submitted or Published  
under ONR Sponsorship during this Reporting Period**

***Manuscript submitted, but not published***

1. K. K. Kuo and R. Acharya, "Effect of Chamber Pressure and Propellant Composition on Erosion Rate of Graphite Rocket Nozzle", accepted by the 24th JANNAF Rocket Nozzle Technology Subcommittee (RNTS) meeting to be held from October 31-November 4, 2005.
2. B. Evans, P. J. Ferrara, N. A. Favorito, J. D. Moore, E. Boyd, R. Acharya, and K. K. Kuo, "Design of a Solid-Propellant Rocket Motor Simulator for Nozzle Erosion Characterization Under High-Pressure Conditions", accepted by the accepted by the 24th JANNAF Rocket Nozzle Technology Subcommittee (RNTS) meeting to be held from October 31-November 4, 2005.
3. R. Acharya and K. K. Kuo, "Effect of Chamber Pressure and Propellant Composition on Erosion Rate of Graphite Rocket Nozzle", accepted for publication and presentation at 44th Aerospace Sciences Meeting of AIAA to be held in Reno, NV, January 9-12, 2006
4. M. C. Lin, S. Xu, D. G. Musaev, and S. Irle, "Rate Constants for the Dissociative Adsorption of CO<sub>2</sub> on Graphite", accepted by the 24th JANNAF Rocket Nozzle Technology Subcommittee (RNTS) meeting to be held from October 31-November 4, 2005.
5. D. G. Musaev, S. Xu, S. Irle, M. C. Lin, "The Reaction Mechanisms of W/W+ with H<sub>2</sub>O: Computational Studies", submitted to J. Phys. Chem. A.
6. S. Irle, S. C. Xu, D. G. Musaev, and M. C. Lin, "The Interactions and Reactions of CO<sub>2</sub> and CO on the Surface of Graphite", NIST meeting abstract, 2005.
7. J. Dunn, B. Culbertson, and K. Brezinsky, "Heterogeneous Combustion of Rocket Propulsion", accepted by the 24th JANNAF Rocket Nozzle Technology Subcommittee (RNTS) meeting to be held from October 31-November 4, 2005.

***Papers published in peer-reviewed journals***

1. S. C. Xu, S. Irle, D. G. Musaev, M. C. Lin, "Water Clusters on Graphite: Methodology for Quantum Chemical A priori Prediction of Reaction Rate Constants", accepted for publication in J. Phys. Chem. A.

**Demographic Data**

***Demographic Data for this Reporting Period:***

- Number of Manuscripts submitted during this reporting period: 7
- Number of Peer Reviewed Papers submitted during this reporting period: 2
- Number of Non-Peer Reviewed Papers submitted during this reporting period: 5
- Number of Presented but not Published Papers submitted during this reporting period: 0

***Demographic Data for the life of this agreement:***

- Number of Scientists Supported by this agreement (decimals are allowed): 18
- Number of Inventions resulting from this agreement: 0
- Number of PhD(s) awarded as a result of this agreement: 0
- Number of Bachelor Degrees awarded as a result of this agreement: 0
- Number of Patents Submitted as a result of this agreement: 0
- Number of Patents Awarded as a result of this agreement: 0
- Number of Grad Students supported by this agreement: 12.5
- Number of FTE Grad Students supported by this agreement: 7
- Number of Post Doctorates supported by this agreement: 3.5
- Number of FTE Post Doctorates supported by this agreement: 1
- Number of Faculty supported by this agreement: 14
- Number of Other Staff supported by this agreement: 5
- Number of Undergrads supported by this agreement: 3
- Number of Master Degrees awarded as a result of this agreement: 0

**Acknowledgments**

The authors would like to acknowledge the strong support and encouragement of Dr. Judah Goldwasser of ONR for this multi-university research initiative (MURI) project funded under the Contract N00014-04-1-0683. We would also like to acknowledge the invaluable suggestions made by Mr. Shea Parks and Mr. Daniel O. Miller of NAWC-China Lake for the selection of baseline propellants and nozzle materials for this research team. Mr. Miller's input on our rocket motor design for ultra high-pressure erosion characterization at the Pennsylvania State University is also greatly appreciated. Mr. Jerald A. Webber of NAWC-China Lake gave very useful input on the boundary-layer control of nozzle erosion that is also acknowledged.

**References**

1. M. M. Opeka, Nozzle Materials Directions Synopsis, MMO, 24 January. 2002.
2. M. M. Opeka, 49<sup>th</sup> JANNAF Propulsion Meeting, CPIA publication, 14-16 Dec 1999.
3. M. M. Opeka, et al., Conference on New Developments in High Temperature Materials, Istanbul, Turkey, 12-15 Aug 1998, published in *J. Eur. Cer. Soc.* (I 9) Nos 13-14, 1999, pp. 2405-2414.
4. M. M. Opeka, Nozzle Materials Selection 2, JANNAF RNTS, Propulsion Mtg, CPIA pub, 26, 2001.
5. P. J. Wolt, and J. A. Webber, "Demonstration of a Nozzle Boundary Layer Cooling System (NBLCS) as a Means to Mitigate Nozzle Erosion," presented at JANNAF 40th Combustion Subcommittee Meeting, Charleston, South Carolina, June 13-17, 2004.
6. A. Freedman, "Halogenation of Carbon Surfaces by Atomic Beams: HOPG Graphite", *Diamond and Related Materials*, 4:216-219, 1995.

7. J. Gonzalez, M. del C. Ruiz, A. Bohe, D. Pasquevich, "Oxidation of Carbons in the Presence of Chlorine", Carbon, 37:1979-1988, 1999.
8. G. Henning, "The properties of the interstitial compounds of graphite, III. The electrical properties of the halogen compounds of graphite", The J. of Chem. Phys., 20:No. 9, September 1952.
9. J. A. F MacDonald, M. J. B. Evans, S. Liang, S. E. Meech, P. R. Norman and L. Pears, "Chlorine and oxygen on the carbon surface", Carbon, Volume 38, Issue 13, 2000, Pages 1825-1830.
10. H. K. Chelliah, A. Makino, I. Kato, N. Araki, and C. K. Law, Combustion and Flame 104:469-480 (1996).
11. M. J. Chiaverini, J. A. Sauer, and S. M. Munson, "Laboratory Characterization of Vortex-Cooled Thrust Chambers for Methan/O<sub>2</sub> and H<sub>2</sub>/O<sub>2</sub>", AIAA Paper No. 2005-4131, July 10-13, 2005.
12. E. M. Abu-Irshaid, and J. Majdalani, "Hydrodynamic Instability of the Bidirectional Vortex", AIAA Paper No. 2005-4531, July 10-13, 2005.
13. D. Bradley, G. Dixon-Lewis, S. E. Habik, and E. M. J. Mushi, Twentieth Symposium (International) on Combustion, The Combustion Institute, Pittsburgh, 1984, pp. 931-940.
14. R. H. Hurt and B. S. Haynes, "On the origin of power-law kinetics in carbon oxidation", Thirtieth Symposium (International) on Combustion, The Combustion Institute, Pittsburgh, 2004, pp. 2161-2168.
15. K. Sendt and B. S. Haynes, "Density functional study of the chemisorption of O<sub>2</sub> on the armchair surface of graphite", Thirtieth Symposium (International) on Combustion, The Combustion Institute, Pittsburgh, 2004, pp. 2141-2149.
16. K. K. Kuo and S. T. Keswani, Combustion Science and Technology, 42:145-164 (1984).
17. P. A. Libby and T.R. Blake, Combustion and Flame 41:123-147(1981)
18. P. A. Libby, Combustion and Flame 38:285-300 (1980)
19. H. K. Chelliah, Combustion and Flame 104:81-94(1996)
20. A. Makino, Combustion and Flame 81:166-187 (1990)
21. A. Makino and C. K. Law, Combustion Sci. and Tech. 73: 589-614 (1990)
22. M. Matalon, Combustion Sci. and Tech. 24: 115 (1980)
23. D. Reinelt, A. Laurs, and G. Adomeit, Combustion and Flame 113:373-379 (1998)
24. R. A. Yetter, F. L. Dryer, and H. Rabitz, Combustion Sci. and Tech. 79: 97-128 (1991)
25. S. Apte and V. Yang, "Unsteady Flow Evolution and Combustion Dynamics of Homogeneous Solid Propellant in a Rocket Motor," Combustion and Flame, Vol. 131, 2002, pp. 110-131.
26. S. Apte and V. Yang, "An LES Study of Transition and Flow Instability in a Porous-Walled Chamber with Mass Injection," Journal of Fluid Mechanics, Vol. 477, 2003, pp. 215-225

27. V. E. Banin; C. M. Commissaris; J. H. J. Moors; A. Veefkind. Kinetic study of pulverized coal combustion at high pressure using a shock tube. *Combustion and Flame*. 1997, 108, 1-8.
28. T. Bazyn; H. Krier; N. Glumac. Oxidizer and Pressure Effects on the Combustion of 10-micron Aluminum Particles. *Journal of Propulsion and Power*. Submitted for publication
29. A. V. Fedorov. Mixing in Wave Processes Propagating in Gas Mixtures (Review). *Combustion, Explosion, and Shock Waves*. 2004, 40, 1, 17-31.
30. K. K. Kuo; S. T. Keswani. A Comprehensive Theoretical Model for Carbon-Carbon Composite Nozzle Recession. *Combustion Science and Technology*. 1985, 42, 145-164.
31. Z. H. Zhu; J. Finnerty; C. Q. Lu; M. A. Wilson; R. T. Yang. Molecular orbital theory calculations of the H<sub>2</sub>O-carbon reaction. *Energy and Fuels*. 2002, 16, 847-854.
32. N. Kayembe; A. H. Pulsifer. Kinetics and Catalysis of the Reaction of Coal Char and Steam. *Fuel*. 1976, 55, 211-216.
33. M. K. King. Kinetics of High-Temperature Reactions of Graphite with Carbon Dioxide and Water. *Journal of Spacecraft*. 1971, 8, 470-476.
34. G. Blyholder; H. Eyring. Kinetics of the Steam-Carbon Reaction. *Journal of Physical Chemistry*. 1959, 63, 693-696.
35. J. S. Binford; H. Eyring. Kinetics of the Steam-Carbon Reaction. *Journal of Physical Chemistry*. 1956, 60, 486-491.
36. E. S. Golovina; G. P. Khaustovich. The Interaction of Carbon with Carbon Dioxide and Oxygen at Temperatures up to 3000K. Eighth Symposium (BBInternational) on Combustion, Pittsburgh, Pennsylvania, 1962; p 784-792.
37. E. T. Turkdogan; V. Koump; J. V. Vinters; T. F. Perzak. Rate of oxidation of graphite in carbon dioxide. *Carbon*. 1968, 6, 467-484.
38. E. T. Turkdogan; J. V. Vinters. Kinetics of oxidation of graphite and charcoal in carbon dioxide. *Carbon*. 1969, 7, 101-117.
39. E. T. Turkdogan; J. V. Vinters. Effect of carbon monoxide on the rate of oxidation of charcoal, graphite, and coke in carbon dioxide. *Carbon*. 1970, 8, 39-53.
40. K. H. Van Heek; H. Juntgen; W. Peters. Fundamental studies on coal gasification in the utilization of thermal energy from nuclear high-temperature reactors. *Journal of the Institute of Fuel*. 1973, 46, 249-258.
41. L. G. Overholser; J. P. Blakely. Oxidation of Graphite by Low Concentrations of Water Vapor and Carbon Dioxide in Helium. *Carbon*. 1965, 2, 385-394.
42. S. R. Story; R. J. Fruehan. Kinetics of Oxidation of Carbonaceous Materials by CO<sub>2</sub> and H<sub>2</sub>O between 1300C and 1500C. *Metallurgical and Materials Transactions B*. 2000, 31B, 43-54.

43. K. J. Laidler *Chemical Kinetics*; 3 ed.; HarperCollinsPublishers: New York, 1987.
44. M. C. Lin, D. G. Musaev, and S. Irle, Milestones for the MURI RNEM Program of the Emory Team.
45. S. Xu, S. Irle, D. G. Musaev, M. C. Lin, "Water Clusters on Graphite: Methodology for Quantum Chemical A priori Prediction of Reaction Rate Constants", submitted to *J. Phys. Chem. A* (MS Number jp053234j).
46. D. G. Musaev, S. Xu, S. Irle, M. C. Lin, "The Reaction Mechanisms of W/W+ with H<sub>2</sub>O: Computational Studies", submitted to *J. Phys. Chem. A*.
47. A. Kumar, M. Elstner, S. Suhai, "DFTB-D study of intercalating carcinogens: Benzo(a)pyrene and its metabolites complexed with the G-C base pair", *Int. J. Quant. Chem.* 95(1), 44-59 (2003).
48. W. Mokrushin, V. Bedanov, W. Tsang, M. Zachariah, V. Knyazev, *ChemRate*, Version 1.20, National Institute of Standards and Technology Gaithersburg, MD 20899, U.S.A. (2003).
49. C. T. Rettner, M. N. R. Ashfold, "Dynamics of Gas-Surface Interactions" (Chapter 5, *Kinetics of Surface Reactions*), The Royal Society of Chemistry, 1991.
50. S. J. Klippenstein, A. F. Wagner, R. C. Dunbar, D. M. Wardlaw, S. H. Robertson, *Variflex*, 1999.
51. K. U. Albrechtsen, D. E. Bolton, T.E. Earnest, M. E. Ewing, M. Longaker, , B. B. McWhorter, and T. C. Noble, "Real-Time Inhibitor Recession Measurements in Two Space Shuttle Reusable Solid Rocket Motors," AIAA 2003-5107, 39th Joint Propulsion Conference and Exhibit, July 2003.
52. L. Anderson and D. Lewis, "Effects of Melt-Layer Formation on Ablative Materials Exposed to Highly Aluminized Rocket Motor Plumes," AIAA 98-0872, 36th Aerospace Sciences Meeting and Exhibit, Jan. 1998.
53. G. Beall, Z. Shirin, S. Harris, M. Wooten, C. Smith, and A. Bray, "Development of an Ablative Insulation Material for Ramjet Applications," *J. Spacecraft*, Vol. 41, No. 6, pp. 1068-1071.
54. S. S. Bhagawan, R. Sivaramakrishnan, S. G. Meera, Propellant Eng. Div., Vikram Sarabhai Space Cent., Thiruvananthapuram, India. Editor(s): Francis, D. Joseph; George, K. E. *Natl. Conf. Adv. Polym. Technol.* (1991), 114-21. Publisher: Cochin Univ. Sci. Technol., Kochi, India CODEN: 58FSAU Conference written in English. CAN 118:104529 AN 1993:104529 CAPLUS
55. A. Bizot, "Turbulent Boundary Layer with Mass Transfer and Pressure Gradient in Solid Propellant Rocket Motors," AIAA 95-2708, 31st Joint Propulsion Conference and Exhibit, July 1995.
56. D. Boury, J. Rey, A. Cronier, P. Greco, and G. Chounet, "Rubber Materials and Solid Propulsion General Overview and Technical Challenges," AIAA 2005-3609, 41st Joint Propulsion Conference and Exhibit, July 2005.



57. R. C. Bunker and A. Prince, "Hybrid Rocket Motor Nozzle Material Predictions and Results," AIAA 92-3591, 28th Joint Propulsion Conference and Exhibit, July 1992.
58. T. Cai and X. Hou, "Simple Method for Numerical Simulation of Temperature Response of the Solid Rocket Nozzle," J. Thermophysics, Vol. 4, pp. 42-46, Jan. 1990.
59. F. Cauty, "Ultrasound Method Applied to Full-Scale Solid Rocket Motor," Journal of Propulsion and Power, Vol. 16, No. 3, pp. 523-528, May-June 2000.
60. Y. K. Chen and F. S. Milos, "Two-Dimensional Implicit Thermal Response and Ablation Program for Charring Materials," Vol. 38, No. 4, July-Aug. 2001.
61. J. L. Clayton and J. McAnally, "Thermal Modeling of SRM Liner Materials Using 2-D Finite Element Adaptive Grid Techniques," JANNAF Rocket Nozzle Technology Subcommittee Meeting, pp. 35-43, Nov. 1994.
62. S. K. Das, Subrahmanya S. Katte, and S. P. Ventateshan, "Two-Dimensional Ablation in Cylindrical Geometry," Journal of Thermophysics and Heat Transfer, Vol. 14, No. 4, pp. 548-556, Oct.-Dec. 2000.
63. A. Davidy, A. M. Achlama, A. Ronen, H. Levy, and R. Grosfeld, "Determination of Kinetic Parameters of Ablating Polymers," AIAA 2005-4494, 41st Joint Propulsion Conference and Exhibit, July 2005.
64. W. A. Dick, M. T. Heath, R. A. Fiedler, and M. D. Brandyberry, "Advanced Simulation of Solid Propellant Rockets from First Principles," AIAA 2005-3990.
65. A. M. Eaton, M. E. Ewing, and K. M. Bailey, "Modeling the Gas Dynamics Environment in a Subscale Solid Rocket Test Motor," AIAA 2001-3584, 37th Joint Propulsion Conference and Exhibit, July 2001.
66. Y. Fabignon, "Ablation Rate Calculation of Thermal Insulations in Segmented Solid Propellant Rocket Motors," AIAA 93-1884, 29th Joint Propulsion Conference and Exhibit, June 1993.
67. Jun-Ling Fan, Insulating elastomer compositions for solid propellant rocket motors. U.S. Pat. Appl. Publ. (2004), 6 pp. CODEN: USXXCO US 2004229989 A1 20041118 CAN 141:412290 AN 2004:999697 CAPLUS.
68. Jun-Ling Fan, Syi-Pang Chang Chem. Systems Res. Div., Chung Shan Inst. Sci. Technology, Lung-Tan, Taoyuan, Taiwan. Huoyao Jishu (2001), 17(2), 59-68. CODEN: HJISE2 ISSN.
69. Jung-Ning Fan, (Chung Shan Institute of Science and Technology, Taiwan). Taiwan (2004), 2 pp. CODEN: TWXXA5 TW 574305 B 20040201 Patent written in Chinese. Application: TW 2002-91125343 20021025. CAN 142:263948 AN 2004:749653 CAPLUS.
70. Jung-Ning Fan, (Chung-Shan Institute of Science and Technology, Taiwan). Taiwan (2000), 24 pp. CODEN: TWXXA5 TW 411346 B 20001111 Patent written in Chinese. Application: TW 98-87111482 19980715. CAN 138:57328 AN 2003:32527 CAPLUS.

71. H. M. Gajiwala, Low-cost, low-density, ablative rubber insulation for rocket motors. U.S. Pat. Appl. Publ. (2004), 23 pp. CODEN: USXXCO US 2004209987 A1 20041021 CAN 141:351313 AN 2004:878183 CAPLUS.
72. B. Garrettson, Silicone-fiber-cork ablative insulation material. U.S. Pat. Appl. Publ. (2004), 3 pp. CODEN: USXXCO US 2004241408 A1 20041202 CAN 142:24316 AN 2004:1036476 CAPLUS.
73. D. G. Guillot, A. R. Harvey, EPDM rocket motor insulation. PCT Int. Appl. (2000), 61 pp. CODEN: PIXXD2 WO 2000043445 A2 20000727 CAN 133:121518 AN 2000:513744 CAPLUS.
74. D. G. Guillot, Low-density, thermoplastic elastomeric, ablative insulation for rocket motors. U.S. (1996), 6 pp. CODEN: USXXAM US 5498649 A 19960312 CAN 124:292034 AN 1996:229088 CAPLUS.
75. H. He and H. Yan, "Ablation Model of EPDM," Journal of Propulsion Technology (1001-4055), Vol. 20, No. 4, pp. 36-39, Aug. 1999.
76. T. N. Johnson, "High Temperature Material Performance Testing Using Continuous Wave Carbon Dioxide Lasers." Proceedings of The 4th Conference on Aerospace Materials, Processes, and Environmental Technology, 2001.
77. V. Jones and K.N. Shukla, "In-Depth Response of Charring Ablators to High Temperature Environment," AIAA 99-3462, 33rd Thermophysics Conference, June-July 1999.
78. N. Katsube and Y. Wu, "A Thermomechanical Model for Chemically Decomposing Composites – I. Theory," Int. J. Engng. Sci. Vol. 35, No. 2, pp. 113-128, 1997.
79. D. J. Kavanaugh and C. C. Nichols, "A Post Burn Outgassing and Thrust Prediction for the IUS Solid Rocket Motors," AIAA 80-1104, 16th Joint Propulsion Conference, June-July 1980.
80. J. H. Koo, L. A. Pilato, and G. E. Wissler, "Polymer Nanostructured Materials for Propulsion Systems," AIAA 2005-3606, 41st Joint Propulsion Conference and Exhibit, July 2005.
81. V. Krishnan and M. Keyhani, "A One-Dimensional Thermal Model with an Efficient Scheme for Surface Recession," JANNAF Rocket Nozzle Technology Subcommittee Meeting, pp. 1-15, Dec. 1992.
82. R. K. Madabhushi and J. S. Sabnis, "Simulation of Flow and Particle Impingement Patterns in Titan IV SRM AFT Closure," AIAA 95-2879, 31st Joint Propulsion Conference and Exhibit, July 1995.
83. D. L. Misterek and K. K. Pace, "Motor Internal Insulation Design Verification and Non-Conformance Analysis," AIAA 96-2637, 32nd Joint Propulsion Conference and Exhibit, July 1996.
84. F.M. Najjar, L. Massa, R. Fiedler, A. Haselbacher, B. Wasistho, S. Balachandar, and R. D. Moser, "Effects of Aluminum Propellant Loading and Size Distribution

- in BATES Motors: A Multiphysics Computational Analysis,” AIAA 2005-3997, 41st Joint Propulsion Conference and Exhibit, July 2005.
85. M. O’Malley, “A Model for Predicting RSRM Joint Volume Pressurization, Temperature Transients, and Ablation,” AIAA 88-3332, 24th Joint Propulsion Conference, June-July 1988.
  86. E. Robert, J. C. Traineau, and F. Vuillot, “The French Research and Technology Program on the Aerodynamics of Segmented Solid Motors: ASSM,” IAF-95-S.1.08, 46th International Astronautical Congress, Oct. 1995.
  87. P. S. Roganov and V. P. Zabolotskiy, “Mathematical Modeling of Heat and Mass Transfer on a Catalytic Wall in Flow of High-Enthalpy Gas,” Heat Transfer-Soviet Research, Vol. 17, No. 5, pp. 117-123, Sept.-Oct. 1985.
  88. P. Ruth, R. Blanski, and J. H. Koo, “Preparation of Polymer Nanocomposites for Solid Rocket Motor Insulation,” March 2004.
  89. M. Salita, “Closed-Form Analytical Solutions for Fluid Mechanical, Thermochemical, and Thermal Processes in Solid Rocket Motors,” AIAA 98-3965.
  90. S. Saterlie, E. Zabrensky, A. Kwas, K. Brunetto, R. Saterlie, W. Wong, S. Bhe, and M. Gallogly, Northrop Grumman, San Bernardino, USA. International SAMPE Symposium and Exhibition (2004), 49(SAMPE 2004), 659-666. CODEN: ISSEEG ISSN: 0891-0138. Journal; General Review; Computer Optical Disk written in English. AN 2004:815811 CAPLUS
  91. Y. C. Shih, F. B. Cheung, J. H. Koo, and B. C. Yang, “Numerical Study of Transient Thermal Ablation of High-Temperature Insulation Materials,” Journal of Thermophysics and Heat Transfer, Vol. 17, No. 1, pp. 53-61, Jan-March 2003.
  92. K. Skokova and B. Laub, “Experimental Evaluation of Thermal Protection Materials for Titan Aerocapture,” AIAA 2005-4108, 41st Joint Propulsion Conference and Exhibit, July 2005.
  93. R. B. Smalley, Jr. Passive, IR-reflective thermal insulator coatings for firearms cartridges, solid rocket motors, and caseless ammunition. U.S. (2004), 26 pp., Cont.-inpart of U.S. Ser. No. 946,127. CODEN: USXXAM US 6832556 B1 20041221 CAN 142:59315 AN 2004:1100326 CAPLUS.
  94. “Solid Rocket Motor Internal Insulation,” NASA Space Vehicle Design Criteria (Chemical Propulsion), NASA SP-8093, pp. 77-80, Dec. 1976.
  95. M. Storti, “Numerical Modeling of Ablation Phenomena as Two-Phase Stefan Problems,” Int. J. Heat Mass Transfer, Vol. 38, No. 15, pp. 2843-2854, 1995.
  96. E. J. Wernimont, “48-Inch Sub-Scale Motor Material Testing of Space Shuttle Advanced Solid Rocket Motor Carbon Cloth Phenolic Ablatives,” AIAA 93-2213, 29th Joint Propulsion Conference and Exhibit, June 1993.
  97. H. Wirzberger and S. Yaniv, “Prediction of Erosion in a Solid Rocket Motor by Alumina Particles,” AIAA 2005-4496, 41st Joint Propulsion Conference and Exhibit, July 2005.

98. E. Wienholts, "3D Flow Thermal Analysis of a Defect in the RSRM Field Joint," AIAA 89-2778, 25th Joint Propulsion Conference, July 1989.
99. T. F. Zien, "Application of Heat Balance Integral Method to Droplet Freezing in Melting Ablation," AIAA 2004-167, 42nd AIAA Aerospace Sciences Meeting and Exhibit, Jan. 2004.
100. E. M. Larson, P. A. Waide, J. Wong, *Rev. Sci. Instrum.*, 1990, 62, 53-57.
101. A. C. Jupe, X. Turrillas, P. Barnes, and S. L. Colston, *Phys. Rev. B*, 1996, 53, R14697-14700.
102. Private communication between GaTech group of the MURI Team and Dr. K. H. Sandhage of the School of Material Science and Engineering of Georgia Institute of Technology on nozzle fabrication.
103. M. B. Dickerson, P. J. Wurm, J. R. Schorr, W. A. Hoffman, P. G. Wapner, and K. H. Sandhage, *Journal Material Science* 39 (2004), 6005 – 6015.
104. A. B. Anderson and D. B. Kang, *Journal Physics and Chemistry B*, 1998, 102(29), 5993 – 5996.
105. P. Amara, A. Volbeda, J.C. Fontecilla-Camps, and M.J. Field, *Journal American Chemical Society*, 1999, 121, 4468 – 4477.
106. E. J. Bylaska, J. R. Rustad, and M. Dupuis, *Environmental Dynamics and Simulation*, 1999, Annual Report.
107. J. R. Rustad, E. J. Bylaska, D. A. Dixon, A. R. Felmy, and K. M. Rosso, *Environ. Dyn. Simulation*, 1999, Annual Report.
108. P. E. Blöchl, *Phys. Rev. B*, 1994, 50(24), 17953 – 17979.
109. A. Eichler, *Surface Sci.* 498, 2002, 314 – 320.
110. A. Gross, *Surface Sci.* 500, 2002, 347 – 363.
111. A. Eichler and J. Hafner, *Phys. Rev. Lett.* 79, 1997, 4481.
112. P.A. Redhead, *Trans. Faraday Soc.* 57, 641 (1961).
113. L.J. Rigby, *Can. J. Phys.* 42, 1256 (1964).
114. T.W. Hickmott and G. J. Ehrlich, *Chem. Phys.* 24, 1263 (1956).
115. J. Eisnger, *J. Chem. Phys.* 27, 1206 (1957).
116. R.E. Schlier, *J. Appl. Phys.* 29, 1162 (1958).
117. J.A. Becker, *Solid State Phys.* 7, 379 (1958).
118. R. Gomer, *J. Chem. Phys.* 28, 168 (1958).
119. R. Klein, *J. Chem. Phys.* 31, 1306 (1959).
120. T.E. Madey, J.T. Yates Jr., and R.C. Stern, *J. Chem. Phys.* 42, 4 (1965).
121. M. E. Coltrin, R. J. Kee, and F. M. Rupley, "Surface Chemkin: A general formalism and software for analyzing heterogeneous chemical kinetics at a gas-

- surface interface," International Journal of Chemical Kinetics, Vol. 23, p 1111-1128, 1991.
122. M. E. Coltrin, R. J. Kee, and F. M. Rupley, "Surface Chemkin: A fortran package for analyzing heterogeneous chemical kinetics at a solid surface - gas phase interface," Sandia Report SAND90-8003B, July 1991.
  123. M. E. Coltrin, R. J. Kee, and F. M. Rupley, "Surface Chemkin III: User manual," Reaction Design, 1996.
  124. D. Y. Li, K. Elalem, M. J. Anderson, and S. Chiovelli, "A microscale dynamical model for wear simulation," WEAR, Vol. 225-229, p 380-386, 1999.
  125. Q. Chen, and D. Y. Li, "Computer simulation of solid particle erosion," WEAR, Vol. 254, p 203-210, 2003.
  126. K. Elalem and D. Y. Li, "Dynamical simulation of an abrasive wear process," Journal of Computer-Aided Materials Design, Vol. 6, p 185-193, 1999.
  127. Q. Chen and D. Y. Li, "Computer simulation of solid-particle erosion of composite materials," WEAR, Vol. 255, p 78-84, 2003.
  128. Y. Niu and C. Tsai, "Simulation of erosion by the dilute particle flow impact," Numerical Heat Transfer, Part A, Vol. 37, p 167-187, 2000.
  129. SGTE substance database (SSUB3) available from ([www.sgte.org](http://www.sgte.org)).
  130. ThermoCalc software available from ([www.thermocalc.com](http://www.thermocalc.com)).
  131. Phase Diagrams of Binary Copper Alloys, Ed. P. R. Subramanian, D. J. Chakrabarti, and D. E. Laughlin (ASM International, 1994, Materials Park, OH) 475-477.
  132. Diffusion in Solid Metals and Alloys, Landolt-Bornstein, New Series, Group III, Volume 26, ed. H. Mehrer (Springer-Verlag, NY, 1990).
  133. E. C. Golovina, "The gasification of carbon by carbon dioxide at high temperature and pressures", Carbon, Vol. 18, pp. 197-201, 1980.

# Appendix A: Solid Propellant Rocket Motor Test Matrix at PSU (Kuo Group)

<b>TOTALS</b>					
Propellant Type	Grain Lengths [in]	Volume [in <sup>3</sup> ]	Volume [gal]	Weight [lb]	Number of Tests
"S"	5, 8, 10, 13, 19	2730	12	173	16
"M"	5, 8, 13	1975	9	128	16
Total		4705	21	302	32

## Propellant "S" with Graphite Nozzle

Pressure [psi]	1000	3000	5000	7000
Propellant "S" Burn Rate [in/s]	1.422	2.458	2.988	3.398
Density [lb/in <sup>3</sup> ]	0.06327	0.06327	0.06327	0.06327

Grain Diameter [in]	4.30	4.30	4.30	4.30	<b>TOTALS</b>
Number of Tests	2	2	2	2	8
Duration [s]	3.52	3.25	3.35	2.94	
Length [in]	5.00	8.00	10.00	10.00	66.00
Volume [in <sup>3</sup> ]	72.61	116.18	145.22	145.22	958.45
Volume [gal]	0.31	0.50	0.63	0.63	4.15
Mass [lb]	4.59	7.35	9.19	9.19	60.64
Number of Tests	2	2	2	2	8
Duration [s]	7.03	5.29	6.36	5.59	
Length [in]	10.00	13.00	19.00	19.00	122.00
Volume [in <sup>3</sup> ]	145.22	188.79	275.92	275.92	1771.69
Volume [gal]	0.63	0.82	1.19	1.19	7.67
Mass [lb]	9.19	11.94	17.46	17.46	112.09
Nozzle Height [in]	0.23	0.17	0.145	0.13	
Nozzle Width [in]	0.69	0.51	0.435	0.39	
Predicted Pressure [psia]*	954	3064	5020	7003	

Number of Tests	16
Length [in]	188
Volume [in <sup>3</sup> ]	2730
Volume [gal]	12
Mass [lb]	173

\* Predicted chamber pressures do not account for nozzle erosion

### Propellant “M” with Graphite Nozzle

Pressure [psi]	1000	3000
Propellant "M" Burn Rate [in/s]	1.2272	2.2579
Density [lb/in <sup>3</sup> ]	0.065	0.065

Grain Diameter [in]	4.30	4.30	<b>TOTALS</b>
---------------------	------	------	---------------

Number of Tests	2	2	4
Duration [s]	4.07	3.54	
Length [in]	5.00	8.00	26.00
Volume [in <sup>3</sup> ]	72.61	116.18	377.57
Volume [gal]	0.31	0.50	1.63
Mass [lb]	4.72	7.55	24.54

Number of Tests	2	2	4
Duration [s]	6.52	5.76	
Length [in]	8.00	13.00	42.00
Volume [in <sup>3</sup> ]	116.18	188.79	609.92
Volume [gal]	0.50	0.82	2.64
Mass [lb]	7.55	12.27	39.65

Nozzle Height [in]	0.225	0.175
Nozzle Width [in]	0.675	0.525
Predicted Pressure [psia]*	980	2934

Number of Tests	8
Length [in]	68
Volume [in <sup>3</sup> ]	987
Volume [gal]	5
Mass [lb]	65

\* Predicted chamber pressures do not account for nozzle erosion

Propellant “M” with Cu-W Nozzle

Pressure [psi]	1000	3000
Propellant "M" Burn Rate [in/s]	1.2272	2.2579
Density [lb/in <sup>3</sup> ]	0.065	0.065

Grain Diameter [in]	4.30	4.30	<b>TOTALS</b>
---------------------	------	------	---------------

Number of Tests	2	2	4
Duration [s]	4.07	3.54	
Length [in]	5.00	8.00	26.00
Volume [in <sup>3</sup> ]	72.61	116.18	377.57
Volume [gal]	0.31	0.50	1.63
Mass [lb]	4.72	7.55	24.54

Number of Tests	2	2	4
Duration [s]	6.52	5.76	
Length [in]	8.00	13.00	42.00
Volume [in <sup>3</sup> ]	116.18	188.79	609.92
Volume [gal]	0.50	0.82	2.64
Mass [lb]	7.55	12.27	39.65

Nozzle Height [in]	0.225	0.175
Nozzle Width [in]	0.675	0.525
Predicted Pressure [psia]*	980	2934

Number of Tests	8
Length [in]	68
Volume [in <sup>3</sup> ]	987
Volume [gal]	5
Mass [lb]	65

\* Predicted chamber pressures do not account for nozzle erosion



Appendix B: Solid Propellant Rocket Motor Test Matrix at PSU for Option Program  
(Kuo Group)

**TOTALS FOR OPTION PROGRAM**

Propellant Type	Grain Lengths [in]	Volume [in <sup>3</sup> ]	Volume [gal]	Weight [lb]	Number of Tests
"M"	10, 19	3369	15	219	16

Propellant "M" with Graphite Nozzle  
(Option Program)

Pressure [psi]	5000	7000
Propellant "M" Burn Rate [in/s]	2.9980	3.6135
Density [lb/in <sup>3</sup> ]	0.065	0.065

Grain Diameter [in]	4.30	4.30	<b>TOTALS</b>
---------------------	------	------	---------------

Number of Tests	2	2	4
Duration [s]	3.34	2.77	
Length [in]	10.00	10.00	40.00
Volume [in <sup>3</sup> ]	145.22	145.22	580.88
Volume [gal]	0.63	0.63	2.51
Mass [lb]	9.44	9.44	37.76

Number of Tests	2	2	4
Duration [s]	6.34	5.26	
Length [in]	19.00	19.00	76.00
Volume [in <sup>3</sup> ]	275.92	275.92	1103.67
Volume [gal]	1.19	1.19	4.78
Mass [lb]	17.93	17.93	71.74

Nozzle Height [in]	0.155	0.143
Nozzle Width [in]	0.465	0.429
Predicted Pressure [psia]*	4929	6905

Number of Tests	8
Length [in]	116
Volume [in <sup>3</sup> ]	1685
Volume [gal]	8
Mass [lb]	110

\* Predicted chamber pressures do not account for nozzle erosion

Propellant "M" with Cu-W Nozzle  
(Option Program)

Pressure [psi]	5000	7000
Propellant "M" Burn Rate [in/s]	2.9980	3.6135
Density [lb/in <sup>3</sup> ]	0.065	0.065

Grain Diameter [in]	4.30	4.30	<b>TOTALS</b>
---------------------	------	------	---------------

Number of Tests	2	2	4
Duration [s]	3.34	2.77	
Length [in]	10.00	10.00	40.00
Volume [in <sup>3</sup> ]	145.22	145.22	580.88
Volume [gal]	0.63	0.63	2.51
Mass [lb]	9.44	9.44	37.76

Number of Tests	2	2	4
Duration [s]	6.34	5.26	
Length [in]	19.00	19.00	76.00
Volume [in <sup>3</sup> ]	275.92	275.92	1103.67
Volume [gal]	1.19	1.19	4.78
Mass [lb]	17.93	17.93	71.74

Nozzle Height [in]	0.155	0.143
Nozzle Width [in]	0.465	0.429
Predicted Pressure [psia]*	4929	6905

Number of Tests	8
Length [in]	116
Volume [in <sup>3</sup> ]	1685
Volume [gal]	8
Mass [lb]	110

\* Predicted chamber pressures do not account for nozzle erosion

Appendix C: Solid Propellant Rocket Motor Test Matrix at PSU for Base and Option Program (Yetter Group)

Propellant Type	Sample Geometries	Volume [gal]	Weight [lb]	Purpose
"M"	10 cm x 10 cm x 25 cm	0.5	10	For 30 Tests
"S"	10 cm x 10 cm x 25 cm	0.5	10	For 30 Tests

Appendix D: Solid Propellant Rocket Motor Test Matrix at GaTech for Base and Option Program (GaTech Group)

Stead-state chamber pressure (psi)	Propellant	Throat Diameter (mm)	# Starter sticks	Stick length burned in transient (in)	Chamber diameter (in)	Chamber length (sized for a 3s steady state burn, in)	Time to pressures (s)	Main L for 3s burn (in)	Starter length (in)	Shakedown	Throat compare	Duration	xray	SUM	Mass
1000	S	2	1	0.227193267	4	6	0.199	4.4944298	0.2271933	2				2	0.101659
2000	S	2	2	0.396054434	4	8	0.251	6.6335941	0.7921089	2	3			5	0.550026
3000	S	2	2	0.785026717	4	10	0.455	8.1590798	1.5700534	1			6	7	1.253304
4000	S	2	2	1.083688832	4	10	0.563	11.482261							
5000	S	2	2	1.43795463	4	12	0.688	13.277944							
1000	S	3	1	0.207140392	4	6	0.18	4.4743769	0.2071404	2		4		6	0.64317
2000	S	3	2	0.359867368	4	8	0.242	6.597407	0.7197347	2	3			5	1.114617
3000	S	3	2	0.67132707	4	10	0.383	8.0453802	1.3426541	1		5		6	2.099893
4000	S	3	1	0.808466021	4	10	0.412	9.8481261							5.762669
5000	S	3	1	1.064276721	4	12	0.499	11.092633							
1000	M	2	1	0.217445752	4	6	0.221	3.8889234	0.2174458	2		4		2	0.100771
2000	M	2	2	0.383616942	4	8	0.302	5.7923285	0.7672309	2	3			5	0.547411
3000	M	2	2	0.600043336	4	8	0.4	7.3737201	1.2000867	1		5	6	7	1.173424
4000	M	2	2	1.089152896	4	10	0.639	11.213768							
5000	M	2	2	1.506124332	4	12	0.8	13.512324							
1000	M	3	1	0.196161335	4	6	0.198	3.877639	0.1961613	2				6	0.636138
2000	M	3	2	0.34175378	4	8	0.266	5.7504653	0.6835076	2	3			5	1.103485
3000	M	3	2	0.515168022	4	8	0.337	7.2888448	1.0303360	1				6	2.009295
															5.570523

**Test Matrix at GaTech**

The test matrix has been designed to provide an optimum test plan for synchrotron X-ray that will be conducted at the Argon National Laboratories. The synchrotron X-ray tests are planned to observe the time-dependent erosion process in a modified strand burner system. First stage of the strand burn test will be conducted in a pressure range that will vary from 1000 to 3000 psi. We are initially considering two throat diameters and three different nozzle materials. The maximum test duration will be 3 seconds. However, to study the time-dependent erosion process, tests will be of a duration that will be less than the full duration of 3 seconds. The next item of interest in the test matrix is the metallized and non-metallized propellants. First series of tests will be with non-metallized propellants. Following these tests, metallized propellants will be considered, including any needed redesign of the burn strand.

The test matrix is designed such that we do not have to conduct tests all tests to cover the complete range of parameters.. As the tests are conducted and we learn from the analysis of tests, many tests can be eliminated. First series of tests consists of shake down tests to understand the performance of the burner system. Next series of tests will be to compare the throat diameters. Following the tests, we will explore the needed duration and the pressure realized as a function of the nozzle erosion. This will be followed by tests to understand the time-dependent process of erosion. This will be accomplished by analyzing the recovered nozzles at varying duration of times. Tests will also be conducted to validate and provide input to ab initio studies.

Because the needed number of tests will be large and all tests cannot be included in the test matrix, we are studying the reaction and erosion process by the use of ab initio techniques. In particular we have very encouraging results in our current studies with ab initio/MD techniques. We expect to supplement the test matrix with results from validated ab initio studies that can provide results of tests that can not be included in the test matrix.

Amount of Propellants: As communicated by **Dr. Seitzman**, the amount of propellant needed is 11 to 13 kg. Half of the amount is metallized and the other half is non-metallized propellant.